# Three Dimensional Microstructures for Cell Culture with Engineered Stiffness and Geometry

PAR

Mattia MARELLI

acceptée sur proposition du jury:

Prof. H. Shea, président du jury
Prof. J. Brugger, directeur de thèse
Prof. M. Chiquet, rapporteur
Prof. G. Dietler, rapporteur
Prof. R. Truckenmüller, rapporteur

**EPFL**

ÉCOLE POLYTECHNIQUE
FÉDÉRALE DE LAUSANNE

Suisse
2014

To Gabriele

for being an example of grit and dedication
in going after what one believes in and in making it happen.


*A Gabriele*

*per essere un esempio di grinta e dedizione*
*nell'inseguire ciò in cui si crede e nel realizzarlo.*

# Abstract

In this dissertation, three dimensional (3D) microenvionments for on-chip cell culture, with engineered geometrical and mechanical properties, are presented. Geometrical and mechanical features of the cell milieu at the microscale are crucial regulators of various cell functions [1,2]. Micro-engineered cell-culture substrates are thus becoming key tools in domains such as tissue engineering or pharmacological tests, where they can simulate physiological conditions more realistically than 2D Petri dishes.

Two families of microdevices, with distinct mechanical properties, have been developed in the present work, both with a 3D shape: (i) hard microwells, made out of Si, and (ii) flexible cell-cages made out of curved cantilevers.

The microwells are fabricated using a two steps etching technique. During the first step, an hemispherical cavity is formed. The second etching step allows the shape of microwells to be further modified and made different from an hemisphere, in order to improve the deposition of Au patterns on the internal curved surface of the microwells . Stencil lithography is used for this purpose, thanks to its ability to create micrometric patterns even on non-flat substrates presenting a high surface topography, as it is the case for the wells (depth of few tens of micrometers).

The flexible cell cages, which we named μ-flowers due to their shape, are based on micro-fabricated cantilever beams, bent out of plane by the intrinsic stresses of a bilayer structure. μ-flowers are cell culture substrates designed to mimic essential physical properties of the *in vivo* environment (dimensionality, shape and also rigidity) (i) in a precisely controlled way, (ii) at single-cell scale, and (iii) with a high degree of parallelization. The use of bilayer films (Ti-SiO$_2$) with various thicknesses, made it possible to realize a palette of cantilevers with an almost constant bending radius ($R = 31 \pm 2\,\mu$m, suitable for the fabrication of single-cell devices), but with a stiffness spanning almost two orders of magnitude (spring constant

$k \approx 1 - -80 \times 10^{-3}\,\mathrm{N\,m^{-1}}$). Furthermore, this stiffness range matches the rigidity of various physiological tissues, such as brain, muscle, skin and bone [3], opening the applicability of μ-flowers to the on-chip culture of many cell types.

As it is the case for microwells, μ-flowers are also decorated with Au patterns at the subcellular scale. The chemical contrast of the surfaces (Au vs. oxides) of both the devices, allows for a functionalization/passivation protocol to be applied, which makes the Au patterns cell-adhesive, while the reminder of the device is passivated against adhesion. These patterns are a way to further engineer the geometry of the 3D microenvironment. One possible application is demonstrated by making adhesive Au spots at the end of cantilevers, localizing there the focal adhesions of fibroblasts. This localization is crucial in order to know the point where cell traction forces are applied, allowing the cantilevers to be used as a force gauge.

μ-flowers have been tested by culturing mouse fibroblasts inside them. Microchips $1\,\mathrm{cm} \times 1.2\,\mathrm{cm}$ in size are prepared, containing about $10\,000$ μ-flowers structures. Typically, about 5000 (50%) of them contain cells, showing the suitability of the device for highly parallelized cell culture tests within 3D microenvironments with precisely engineered geometrical and mechanical properties. Finally, a live experiment with fibroblasts showed how bent cantilevers can be deflected by cell contraction, proving the potential of the device also as a tool to measure cell traction forces.

**References**

[1] M. Nikkhah et al., *Biomaterials*, 33 (2012), pp. 5230-46.

[2] J. Fu et al., *Nature Methods*, 9 (2010), pp. 733-6.

[3] D. E. Discher, D. J. Mooney and P. W. Zandstra, *Science*, 324 (2009), pp. 1673-7.

**Keywords list**

| | | |
|---|---|---|
| Microfabrication | Cantilevers | Bilayer |
| Microtechnology | Stiffness | Microwells |
| Bio-MEMS | Spring constant | Silicon etching |
| Cell microenvironment | Bending | Stencil lithography |
| Cell cages | Thin film | Cell traction force |
| Three dimensional (3D) | Stress | Cell traction force microscopy |
| Micro patterning | Silicon oxide (SiO$_2$) | On chip cell culture |
| Surface functionalization | | |

# Résumé

Cette thèse présente des microenvironnements tridimensionnels à des fins de culture cellulaire sur substrats, ayants des propriétés géométriques et mécaniques spécifiques. A l'échelle micrométrique, les propriétés géométriques et mécaniques de l'environnement cellulaire sont des régulateurs cruciaux de diverses fonctions cellulaires [1,2]. C'est pourquoi les substrats pour cultures cellulaires micro-structurés deviennent un outil clé pour les domaines tels que l'ingénierie tissulaire ou les tests pharmacologiques, car ils peuvent simuler des conditions physiologiques de manière plus réaliste que des boites de Pétri bidimensionnelles.

Deux familles de micro-dispositifs 3D avec des propriétés mécaniques différentes ont été développées lors de ce travail : (i) des micro-puits rigides en silicium, et (ii) des cages cellulaires flexibles composées de poutres courbées.

Les micro-puits sont fabriqués en deux étapes de gravure. Durant la première étape, la gravure crée une cavité hémisphérique. La seconde étape de gravure permet de modifier le puits en une forme non hémisphérique, afin d'améliorer la qualité du dépôt d'or sur les faces inclinées. La déposition se fait par lithographie au pochoir, grâce à sa capacité à créer des motifs micrométriques même sur des substrats à forte topographie, comme c'est le cas pour les puits (profondeur de quelques dizaines de micromètres).

Les cages cellulaires flexibles, que nous appellerons µ-fleurs à cause de leur forme, sont basées sur des poutres flexibles micro-fabriquée, type MEMS, courbées par le stress interne dû à une structure double couche. Les µ-fleurs sont donc des substrats de culture cellulaire conçues pour imiter des propriétés essentielles de l'environnement in-vivo (dimension, forme et rigidité) (i) de manière contrôlée, (ii) à l'échelle unicellulaire, et (iii) de manière dense sur de grandes surfaces. L'utilisation de doubles couches (Ti-$SiO_2$) d'épaisseurs variées a permis la réalisation d'une palette de poutres flexibles ayant un rayon de courbure quasi constant ($R = 31 \pm 2\,\mu$m, approprié pour la fabrication de dispositifs pour cellules unitaires),

avec une rigidité variable s'étendant sur près de deux ordre de magnitude (constante de ressort $k \approx 1 - 80 \times 10^{-3}\,\mathrm{N\,m^{-1}}$). De plus, la gamme de rigidité correspond à celle de divers tissus physiologiques, tels que le cerveau, les muscles, la peau et les os [3], ce qui permet l'application des μ-fleurs pour la culture sur substrat de multiples types de cellules.

Tout comme pour les micro-puits, les μ-fleurs sont ornées d'un motif d'or à l'échelle subcellulaire. Le contraste chimique de surface (Or vs oxydes) des deux dispositifs permet d'appliquer des protocoles de fonctionnalisation/passivation, rendant les motifs d'or adhérents pour les cellules, alors que les autres surfaces sont passivées et donc non adhérentes. Ces motifs sont une étape supplémentaire dans l'ingénierie géométrique de l'environnement 3D. Une application possible est démontrée en rendant adhésifs les spots d'or uniquement au bout des poutres, ce qui localise ainsi les points d'adhésion des fibroblastes. Cette localisation est cruciale pour connaitre l'endroit où les forces de traction cellulaire seront appliquées, permettant ainsi d'utiliser les poutres flexibles en tant que dynamomètres.

Les μ-fleurs ont été testées en y cultivant des fibroblastes de souris. Des puces de 1 cm × 1.2 cm contenant environs 10 000 μ-fleurs ont été préparées. De manière générale, environ 5000 (50%) contenaient des cellules, démontrant la capacité du dispositif pour des tests de culture cellulaire hautement parallélisée dans un microenvironnement 3D aux propriétés géométriques et mécaniques spécifiques. Finalement, une expérience en temps réel avec des fibroblastes a montré comment les poutres fléchies peuvent être pliées par contraction cellulaire, prouvant le potentiel de ce dispositif également pour mesurer des forces de traction cellulaire.

**References**

[1] M. Nikkhah et al., *Biomaterials*, 33 (2012), pp. 5230-46.

[2] J. Fu et al., *Nature Methods*, 9 (2010), pp. 733-6.

[3] D. E. Discher, D. J. Mooney and P. W. Zandstra, *Science*, 324 (2009), pp. 1673-7.

**Mots clés**

Microfabrication

Micro-technologie

Bio-MEMS

Microenvironnement cellulaire

Cages cellulaires

Tridimensionnel (3D)

Microstructuration

Fonctionnalisation de surface

Cantilever, poutre

Rigidité

Constante de ressort

Flexion

Couches minces

Stress

Oxyde de silicium ($SiO_2$)

Double couche

Micro-puits

Gravure de silicium

Lithographie au pochoir

Force de traction cellulaire

Microscopie de force
de traction cellulaire

Culture cellulaire sur substrat

# Contents

# Contents

# List of Figures

# List of Tables

# Glossary

**µCP**  microcontact printing. 5, 11

**2D**  two dimensional. 5, 6, 11, 13, 22, 23, 25, 26, 37–39, 85, 94, 96, 98, 99

**3D**  three dimensional. 2, 3, 5, 6, 11, 13, 14, 19, 21, 23, 25, 26, 65, 82, 84, 88, 92–96, 98

**BHF**  buffered hydrofluoric acid. 57, 71, 76

**bio-MEMS**  biological microelectromechanical system. 7, 8

**biocompatibility**  ability to be in contact with a living system without producing an adverse effect (IUPAC definition). 42, 69

**biocompatible**  see biocompatibility. 42

**CTF**  cell traction force. xvii, 3, 6–8, 10, 11, 25, 26, 33, 36, 37, 46, 47, 65, 83, 89–93, 95, 98

**CTFM**  cell traction force microscopy. 3, 11, 26, 37

**DI water**  deionized water. 20, 22, 48, 71, 72, 74

**DMEM**  Dulbecco's Modified Eagle's Medium. 85, 86, 88

**DRIE**  deep reactive-ion etching. 21

**ECM**  extracellular matrix. 2, 5, 6, 93

**FA**  focal adhesion. 5, 6, 33, 39, 40, 83, 88, 97, 98

**FCS**  fetal calf serum. 86–88, 92, 93

**Glossary**

**ICP** inductively coupled plasma. 20, 22, 50, 74

**LPA** lysophosphatidic acid. 88–93

**mechanosensation** the ability of a cell to sense and respond to the mechanical properties of its environment, e.g. changes in matrix compliance [1]. 6, 7

**MEF** mouse embryonic kidney fibroblast. 86, 87, 89, 92, 95

**MEMS** microelectromechanical system. 42

**microenvironment** local surroundings with which cells interact by processing various chemical and physical signals, and by contributing their own effects to this environment. 1–3

**MOS** metal-oxide-semiconductor. 43

**PBS** phosphate buffered saline. 84, 85, 88

**PDMS** poly(dimethylsiloxane). 4, 11, 13, 38, 84, 87, 99

**PEG** polyethylene glycol. 11

**PLL-*g*-PEG** poly(L-lysine)-*grafted*-poly(ethylene glycol). 69, 84–87, 97

**PVD** physical vapor deposition. 14, 22, 41, 69, 71, 76

**RCA cleaning** a standard cleaning procedure performed before high-temperature processing (e.g. oxidation and diffusion) of silicon wafers in semiconductor manufacturing. The procedure was developed by Werner Kern in 1965, while working for the Radio Corporation of America (RCA).. 48

**RIE** reactive ion etching. 22, 50

**SEM** scanning electron microscope. 17, 18, 51, 54, 55, 76

**UV** ultra violet. 50, 72, 73, 84

# 1 Introduction

## 1.1 Background and Motivation

When looking at the astonishing complexity of a developed biological organism, some fundamental questions rise spontaneously: how have such different tissues and organs been generated from the same zygote? How can it be possible that the same DNA-encoded information gives birth to such specific and diverse cell types, such as neurons and muscle fibers, osteoblasts and erythrocytes? The answers lay in the interaction between cells and their surrounding environment. This interaction – as well as the story of all past interactions with the environment – determines the phenotype of the organism (or of the single cell), driving fundamental cell processes such as proliferation, differentiation, migration, gene expression and programmed cell death. The ability to sense and respond to the environment is widespread in almost every cell type [1], and concerns many properties of the external surroundings. Just to name few of them:

- Chemical/biochemical properties:

    soluble molecules (e.g. growth factors and nutrients)

    non-soluble molecules (protein embedded in the extra cellular matrix)

- Physical properties:

    mechanical (e.g. forces from the microenvironment and stiffness [2])

    thermodynamical (e.g. temperature [3])

electromagnetic (e.g. electric fields [4] and currents)

- Geometrical properties:

surface topography (e.g. roughness)

chemical/bio-chemical patterning (biomolecule patterns, gradients etc.)

shape and volume available for the cell

dimensionality (two dimensional or three dimensional substrate)

The knowledge of cell-environment interaction mechanisms is the first step to improve biomedical applications in fields as tissue repairing or tissue engineering, regenerative medicine, cancer therapies and implant surgery. However there is still a long route to go to understand the mechanisms of these interactions, due to the high complexity of the systems involved: cells and surrounding environment. On one hand the biomolecular mechanisms governing cell sensing and response are far from being straightforward, since they involve a large number of signaling pathways, often interacting with each other. On the other hand the external microenvironment itself holds a lot of cues, all acting on the cell at the same time, increasing the degree of convolution and crosstalk of different signals.

It is thus clear that the availability of well-characterized **artificial microenvironments** is fundamental both for basic research and for applications in life science and medicine, since they **allow to precisely know and tune the chemical and physical signals experienced by the cells**. In basic research, a simplified and finely tuned microenvironment allows assessing how cells respond to one or few external stimuli at a time, in a controlled way. Cell culture substrates with engineered properties are also useful in pharmacology and medicine, where they are used to study the reaction of cells to drugs or to grow tissues *in vitro* [5, 6, 7]. Indeed, advanced cell culture substrates have the advantage to mimic some of the features experienced by cells *in vivo*, in a better way with respect to what glass slides or Petri dishes can do. E.g., the stiffness of a substrate could be tuned to approximate the physiological values of a specific tissue; the surface could be functionalized with biomolecules found in the extracellular matrix (ECM), possibly organized in patterns that resemble the spatial organization found *in vivo*; cells could be embedded in a three dimensional (3D) matrix or, again, subjected to time variations of biomolecular signals, thanks to microfluidics.

In the last two decades, many efforts have been made to develop new cell culture substrates that integrate unconventional properties, especially those that concern mechanical and geometrical features (see section 1.3). A fertile interdisciplinary approach – at the crossroad between biology, microtechnology and material science – gave birth to the research field of cellular microenvironment engineering [8]. Indeed, the use of new materials and microfabrication technologies are continuously increasing the ability to realize advanced cell culture substrates, and have already demonstrated how non-chemical stimuli can strongly affect cell behavior (some examples are given in the following state of the art).

## 1.2 Objectives

This project is located inside this arena, and aimed to design, develop and fabricate artificial microenvironments with tailored geometrical and mechanical properties – as well as to test their suitability for cell culture. The main objectives which steered the implementation of such microdevices are:

- realize 3D systems, that could be used to assess the effects of dimensionality

- engineer the mechanical properties (stiffness) of the artificial microenvironment, as done in two dimensions [2, 9, 10]

- use the devices for CTF measurements

## 1.3 State of the Art

The present section starts by covering the advances done in engineering two key aspects of artificial cellular microenvironments, which are at the center of this work: mechanical properties and geometrical properties. A second section is finally dedicated to a survey of cell traction force microscopy (CTFM) techniques.

### 1.3.1 Engineering Mechanical Properties

The mechanical properties of cell culture substrates are known to strongly affect cell behavior, e.g. adhesion, migration, gene regulation and differentiation. The most commonly studied and more easily controllable mechanical feature of artificial substrates is rigidity, quantified by the Young's modulus of a substrate. A systematic investigation of Pelham *et al.* assessed cell locomotion and FA formation on soft polyacrylamide gels, whose Young's modulus was tuned between 10 to 80 Pa by modifying the concentration of the bisacrylamide cross linker, while keeping a constant chemical environment by coating the gels with collagen [2]. The authors observed a loss of regularity of FA shape and size on the softer gels compared to the stiffer ones, where the typical elongated shape of FA is found. FA and cell lamellipodia were also less stable over time on the softer substrates, where higher speed of migrations were observed as well. The same technique (polyacrylamide gels laminated with collagen or fibronectin) has been used by Yeung and coworkers to study the effects of rigidity on the morphology and cytoskeletal organization of various cell kinds [9]. A much wider stiffness range was spanned, with elastic moduli spanning the range from 2 to 55 000 Pa. Two kind of cells (fibroblasts and endothelial) increase their spread area abruptly when the elastic modulus become bigger than 3000 Pa. This transition is accompanied by the appearance of stress fibers. Interestingly, the stiffness dependence of shape and fiber formation is lost when cells are confluent, an effect that has to be taken into account when studying the influence exerted by the microenvironment on cells.

Another technique to tune the rigidity of cell culture substrates makes use of microfabricated vertical posts. In this case, the geometry of the pillars is modified [11], in lieu of the material properties of a continuous substrate, as it is the case for gels or elastomers like poly(dimethylsiloxane) (PDMS). Fu *et al.* have used this method to fabricate a set of substrates with various stiffnesses, but identical topology and surface chemistry, and studied the influence of the mechanical properties of the substrate on the differentiation of human mesenchymal stem cells (hMSCs). They found a correlation among rigidity, magnitude of forces exerted by cells and osteogenic vs. adipogenic differentiation (the stiffer the substrate, the higher the forces and the osteogenic differentiation). Microtechnologies have been used also on a bigger scale (few hundreds of micrometers), in order to fabricate microtissue scaf-

folds constituted by vertical flexible structures with different stiffnesses [12]. NIH 3T3 cells dispersed in collagen gel gathered spontaneously and bridged adjacent pillars. These multi-cellular agglomerates generated a tension proportional to the stiffness of the scaffolds they where anchored on. Moreover, proteins involved in the mechanical structure of cells and in intercellular linking showed a stiffness-modulated expression. A last example of mechanically engineered substrate has been given by Grosberg *et al.*[7], who fabricated flexible cantilevers to be used in the growth of "heart on a chip". The compliance of elastomeric micro-beams allowed to measure the contractility of microtissue strips of laminar cardiac muscle, combined with a quantification of action potential propagation.

### 1.3.2 Engineering Geometry: Patterns and Dimensionality

Two geometrical properties of the microenvironment are pivotal in this dissertation: dimensionality – two dimensional (2D) vs. 3D – and the creation of patterns to confine cells or cell parts, e.g. focal adhesions (FAs).

**Adhesive patterns** made by microcontact printing (μCP) have been used by Chen *et al.* to show the correlation between cell spreading area and apoptosis [13]. They produced adhesive islands coated with a variety of cell-adhesive molecules (fibronectin, antibodies specific for integrin and ECM), observing that the driving parameter that controls cell survival and apoptosis is the area available for the cell to spread. This trend was further confirmed by the authors using discontinuous dotted patterns with constant size and number of dots, but different spacing. In this way, the total area of contact between the cell and the adhesive molecules was maintained constant, while varying the spreading area only. A similar approach was used by Lutz *et al.* [14] to investigate the link between the size of adhesion spots and cell adhesion itself. Nanotechnolgies have been used in order to overcome the limitations of μCP and prepare adhesion spots even below the micrometer scale. The ability of cells to create stable FA was proved to be dependent on the size of the adhesive spots, with FA maturation being inhibited for spots smaller than 1 μm, and cells migrating at lower speed on the smaller spots (< 1 μm). Micropatterns were also used by Théry *et al.* to investigate and control cell organization and division: adhesive figures with various symmetry, on which cells can attach and exert forces, guided mitotic spindle orientation during cell division [15], and

similar patterns have been shown to influence the spatial organization of cell organelles [16].

**3D microstructures** for cell culture are the other field of research concerning geometry that has been considered in the present work. Giselbrecht *et al.* produced 3D microwells via thermoforming of plastic films at the microscale [17], that can be used for 3D cultivation of tissues. Hepatocellular carcinoma cells were affected by the 3D arrangement, displaying an upregulation of genes which support organotypic functions [18]. Stiff microwells made out of Si have been proposed by Nikkhah *et al.* as a tool to study the cytoskeletal organization of normal fibroblasts and breast cancer cells in 3D [19, 20]. The ability to be suspended in a 3D environment has been shown to depend on the cell kind, and based on the correct cytoskeletal functioning. Ochsner *et al.* studied how the dimensionality controls the metabolism and the cytoskeleton assembly of fibroblasts, using 2D and 3D substrates of various shapes and rigidity [21]. The authors used microwells made out of PDMS, whose size is at the single cell scale, and whose shape and rigidity can be easily engineered (Young's modulus between 20 kPa and 1 MPa).

### 1.3.3   Cell Traction Force Microscopy

As seen in the previous section 1.3.1, cells are able to sense and respond to the mechanical properties of their environment – a capability named mechanosensation. A particular mechanosensitive reaction – and a pivotal mechanism in the process of mechanosensation itself – is the ability of cells to internally generate CTFs. These forces are generated via the acto-myosin contraction of the cytoskeleton and are transmitted along actin fibers to FAs, large macromolecular assemblies which link actin fibers to the ECM. FAs do not act solely as an anchorage between the cell and the ECM, but are also responsible for the generation of regulatory biochemical signals in response to the compliance of the ECM. Even if a complete model of all the sensing machinery implemented by FAs is not yet available, there is growing evidence that mechanical tension can activate various modifications of protein conformation, e.g. the opening of $Ca^{2+}$ channels [22] or the exposure of protein active sites upon unfolding [23, 24], which in turn trigger a cascade of biomolecular reactions. It is thus clear how cells use CTFs to probe the stiffness of their environs through FAs, which act as bio-mechanical sensors producing signals to drive cell behavior [25, 26, 27]. For these reasons CTFs are an intersting

observable to understand how mechanosensation works, and the biological microelectrome-chanical systems (bio-MEMS) developed in the context of this work have been designed with the capability of measuring CTFs (see sec. 6.1), proving their potential to combine in a single device the possibility to engineer the mechanical and geometrical features of the substrate together with the possibility to quantify a fundamental physical mechanotransductive cell response such as the generation of CTFs.

The use of cell culture substrates sensitive to CTFs generated by single cells dates back to 1980, with the pioneering work of Harris *et al.* [28, 29] which used elastomeric silicone rubber to highlight the forces generated during cell locomotion, observing the wrinkles produced in the silicone membrane. The novelty of this approach consisted in introducing an inert material like silicone, which is not affected by biochemical changes induced by cells. In this way the only possible contraction of the substrate can be ascribed to CTFs, excluding other causes of shrinkage in the substrate itself (e.g. protein network dehydration in proteic gels) [28]. The membranes produced by Harris *et al.* allowed the observation of wrinkles produced even by single cells. This sensitivity was achieved thanks to the technical ability to prepare membranes with a thickness of about $1\,\mu$m, via a quick and high-temperature cross-link process, done by exposure of the silicone fluid to a flame.

During the mid 90's, Ken Jacobson's group paved the way for the quantification of CTFs [30, 31, 32]. They used the same silicone membranes introduced by Harris, and improved them by embedding latex beads ($1\,\mu$m in diameter) dispersed on the surface. These beads worked as markers to detect and measure the elastic deformations produced by locomoting fish keratocytes. The silicone membrane was fixed to a Pyrex cylinder, preventing wrinkles formation and allowing only in-plane strains to take place under cell forces. This – together with a direct mechanical calibration of the stiffness $k$ of the membranes – made possible for the authors to asses CTFs quantitatively. In the first instance, forces were roughly estimated from the displacement $\delta$ of single beads, as $F = k\delta$ [30]. A little later the method was perfected computationally, in order to retrieve the continuum field of tensions exerted by cells (defined as force per unit area) from the recorded displacements of micro-beads[1] [32]. The technique

---

[1]The stiffness $k$ was calibrated as the ratio $F/\delta$ between a force $F$ parallel to the plane of the membrane and applied in a small area, and the displacement $\delta$ of the point where $F$ was applied. In the case of a cell, things are a bit more complicated. First, a point-like force is not only displacing the point where it is applied, but it produces a deformation in each point of the membrane. Considering a planar force $\mathbf{F}(\mathbf{x})$ applied at $\mathbf{x}$, it will produce in any other point $\mathbf{x}_0$ a displacement vector $\boldsymbol{\delta}(\mathbf{x}_0) = \mathbf{s}(\mathbf{x}_0 - \mathbf{x})\mathbf{F}(\mathbf{x})$, where the tensor $\mathbf{s}$ of rank two is called compliance

of the elastic substrate was brought to maturity in 1999 by Dembo and Wang [33]. They based their work on polyacrylamide hydrogels developed by Pelham and Wang [2, 34]. By changing the concentration of bis-acrylamide over acrylamide, the elasticity of the gel can be tuned. Thus, the stiffness of the substrate can be adapted to various cell kinds, allowing them to generate measurable displacements without exceeding at the same time the linear elastic regime of the substratum. The beads as well were improved, staining them with fluorophores and using smaller bead diameters. Another major advancement of the technique was the functionalization of the hydrogel surface with the protein type I collagen. In this way the mechanical properties of the substratum are tunable while maintaining a constant chemical interface interacting with cells.

Almost at the same time Galbraith *et al.* [35] developed a different method for the measurement of CTFs, based on a micro-machined substrate. They built a bio-MEMS characterized by movable platforms ($2\,\mu m \times 2\,\mu m$ up to $5\,\mu m \times 5\,\mu m$) coplanar with the top surface of a chip. Each one of these platforms is anchored via a pedestal to the free-end of a cantilever that is buried under the surface of the chip. In this way an array of force sensors is fabricated: when a locomoting cell crawls over and pulls a platform, it moves the platform itself by bending the underlying cantilever. A measurement of cantilever deflection provides a quantification of the pulling force, since the spring constant of cantilever was previously calibrated. The major improvements of this approach are the capability to measure CTFs with subcellular resolution, and the use of mechanically isolated force sensors. Indeed the displacement of a given platform depends only on the forces pulling directly on its surface, and not on forces exerted by the cells on adjacent parts of the chip, as it is the case for continuous elastic membranes[1]. This simplifies to a great extent the calculation of forces, which are given by the simple equation $F = k\delta$ ($k$ being the spring constant of the cantilever and $\delta$ being its deflection). The two main drawbacks of this device are the low surface density of sensors (due to the need of building very long and soft cantilevers) and the possibility to measure only the force component perpendicular to cantilevers, losing the information on forces parallel to the

---

tensor. Second, in the case of a cell forces are applied in many points, ideally under the whole area $A_{cell}$ occupied by the cell. It is thus better to talk about a vectorial field of shear force density $\boldsymbol{f}(\mathbf{x})$ exerted by a cell. The resultant displacement in a certain point $\mathbf{x}_0$ is the superposition of all the displacements caused by cell tractions acting under the cell area, and is given by $\boldsymbol{\delta}(\mathbf{x}_0) = \int_{A_{cell}} \mathbf{s}(\mathbf{x}_0 - \mathbf{x})\mathbf{f}(\mathbf{x})\,d\mathbf{x}$. This means that in the case of a continuous field of forces, such as the one exerted by a cell, these forces can not be directly calculated as $F = k\delta$, as done for a single point-like force. Instead, forces and displacement are linked by a convolution, requiring the use of more involved calculation methods in order to retrieve the tension field $\boldsymbol{f}(\mathbf{x})$ from a measurement of the displacement field $\boldsymbol{\delta}(\mathbf{x})$.

| Year | Force Range [nN] | Sensor Density [$\mu m^{-2}$] | Sensor Area [$\mu m^2$] | Sensor kind | Novelty | Cell | Ref. |
|---|---|---|---|---|---|---|---|
| 1980 | — | — | — | Freestanding silicone membrane | Single cell forces detected | chick heart fibroblasts | [28] |
| 1994 | — | — | — | Drumhead silicone membrane with beads | Total forces of single cells quantified[a] | fish keratocytes | [30] |
| 1996 | $\gtrsim 7$ | $\sim 0.04^b$ | $\sim 25^b$ | Drumhead silicone membrane with beads | Sub-cellular forces quantified | fish keratocytes | [31] [32] |
| 1997 | 1.5–150 | $10^{-6}$ | 4–25 | In-plane cantilevers | Discrete measurement of isolated forces (only the component of planar forces which is $\perp$ to cantilever axis is detected) | chicken embryo fibroblasts | [35] |
| 1999 | $\gtrsim 1.3$ | $\sim 0.04^b$ | $\sim 25^b$ | Polyacrylamide hydrogels with beads | Tunable stiffness, functionalization independent from stiffness | 3T3 fibroblasts | [2] [34] [33] |
| 2003 | 12–190 | 0.012 | 7 | PDMS posts | Tunable sensor density and stiffness, measure forces in both planar directions | bovine smooth muscle | [10] |

| Year | Force Range [nN] | Sensor Density [μm$^{-2}$] | Sensor Area [μm$^2$] | Sensor kind | Novelty | Cell | Ref. |
|---|---|---|---|---|---|---|---|
| 2007 | 0.6–190 | 0.012 | 7 | magnetic PDMS posts | Magnetic Co nanowire embedded in PDMS post for magnetic actuation. | 3T3 fibroblasts | [36] |
| 2009 | — | — | — | Polyacrylamide gel with beads (0.8–9 kPa) | 3D force vector (retrieval of the vertical component of forces) | 3T3 fibroblasts | [37] |
| 2010 | — | — | — | Polyacrylamide hydrogel with beads | 4D mapping (3D force vector and fast time leap, i.e. 8.5 s) | Dictyostelium discoideum | [38] |
| 2010 | — | ~ 0.1–0.5[b] | ~ 2–10[b] | PEG hydrogel with beads (0.6–1 kPa) | Cell embedded in 3D, retrieval of 3 components of forces | 3T3 fibroblasts | [39] |

Table 1.1: Evolution of the main tools used for the measurements of CTFs.

[a]No precise measurement of forces, but a rought evaluation of the order of magnitude of the total force exerted by an entire cell.

[b]There is no discrete sensor. The device is made up by a continuum elastic medium, and the spatial resolution is due to the calculation mesh used to compute te forces.

cantilever axis.

Few years later the group of Christopher Chen [10] reported another method to isolate mechanical forces on an elastic substrate. Using the technique of replica-molding, they fabricated arrays of flexible and vertical micro-posts made out of PDMS. Since the posts are vertical (i.e. normal to the substrate surface on which cells are cultured), cell forces can bend them in any direction within the plane of the surface, allowing for the measurement of both tangential components of forces. The authors used μCP in order to functionalize with fibronectin or collagen IV only the top surface of the posts, while the sides were passivated against cell adhesions using Pluronic®. The same group, collaborating with the physics lab of Daniel Reich, improved the tool of microposts by embedding magnetic Co nanowires inside PDMS posts [36]. In this way the sensing capability of their substrate was combined with the possibility to actuate the posts with an external magnetic field, applying external forces to cells.

In 2009 the measurements of CTFs began to quantify the vertical component of forces as well, beside the tangential components parallel to the substrate surface. Using the same established technique based on fluorescent microbeads embedded in a soft polyacrylamide hydrogel, and improving image acquisition[2] and data analysis, Maskarinec and coworkers [37] were able to map the 3D vector of forces exerted by fibroblasts. They found that the vertical component is similar to the tangential ones, an observation confirmed even for other kind of highly motile organisms without focal adhesions [38].

All the forementioned methods made use of 2D substrates, with cells cultured on top of them, on a flat surface. A major change in CTFM was introduced in 2010 again by the group of Chen. They cultured fibroblasts inside a polyethylene glycol (PEG) hydrogel, allowing for the cells to pull and move in a 3D environment. The technique for the calculation of forces relied again on the measurement of the displacements of microbeads, but a finite element method was extended in 3D in order to retrieve the tensions exerted by fibroblasts at the cell/hydrogel interface.

---

[2]Using a laser scanning confocal microscope

# 2 3D Stiff Micro-Wells with Localized Adhesion Sites

## 2.1 Introduction

The use of micro-wells as culture substrates is a common technique in cell biology, for a number of reasons. Firstly, among all cell-retaining techniques, the micro-well structure is the simplest and most straightforward approach that keeps cells physically separate and constrained within their location, allowing them to be analyzed separately. Secondly, they constitute a straightforward way to include the third dimension into otherwise flat substrates, adding geometrical complexity and mimicking the three dimensional (3D) cell arrangement found *in vivo* (e.g. in glands, intestinal villi, hair follicles, etc.). Micro-wells are fabricated in a number of sizes and with a variety of materials. E.g., they have been fabricated in poly(dimethylsiloxane) (PDMS) with tunable stiffness, at the scale of a single cell, to investigate how the dimensionality affects the metabolism and the organization of the cytoskeleton [21]; in Si, with the size of few cells ($\sim 200\,\mu$m), again for the study of the cytoskeleton in 3D microenvironments [20]; with polymer thin films (diameter $\sim 300\,\mu$m), for the study of gene regulation in 3D-chip culture [18]. At the same time, adhesive patterns and surface topography have shown their potential to investigate the influence of two dimensional (2D) controlled geometry onto fundamental cell processes, such as mitotic division [15], internal organelle organization and cell polarization [16], or again to control the arrangement of cells along engineered microstructures, e.g. for the guidance of neural axons along microfabricated grooves [40]. The combination of the two features — topography and 3D shape — in a single device is a challenging task, because of the

small size of the patterns/topography, and the non planar geometry of the micro-wells (indeed, most of surface microtechnologies are developed for flat substrates). A technique based on thermoforming of polymer films has been proposed to fabricate patterned micro-wells. The topographical structures are prepared prior micro-well formation, and the high material coherence maintains them intact during the shaping of the micro-wells *via* thermoforming [41].

**The objective** of the research presented in this chapter **is to fabricate 3D Si micro-wells featuring adhesive patterns on their internal surface, merging** in one single device the possibility to have **3D structures together with patterned adhesive surfaces** at the sub-cellular scale. The following sections illustrate how the Si micro-wells are made, by means of wet etching, and how their shape can be controlled by using a two step etching process. Then, the technique of stencil lithography is briefly introduced and used as a deposition tool to create Au patterns inside the preformed wells, as schematized in Fig. 2.1. Later, these Au patterns
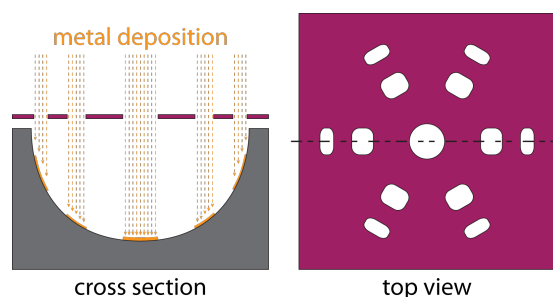


Figure 2.1: Microwell patterning with stencil lithography. The scheme shows the concept of micro-patterns deposition within a Si hemispherical well. **Left**: cross sectional view showing the PVD of a metal, through a stencil mask. Only the metal passing through the apertures is deposited on the substrate. The technique is particularly suitable for topographically complex substrates, on which standard photolithography cannot be applied. **Right**: schematic top view of a typical aperture pattern used in this work. The stencil masks used here are made with low stress silicon nitride (LS SiN) membranes.

can be selectively functionalized with a cell-adhesive peptide, while the rest of the microwell is passivated to prevent cell adhesion. More details about the functionalization strategy of Au patterns will be given later in this dissertation (6.2).

14

## 2.2 Shape Control by Two Steps of Etching

A well characterized effect of stencil lithography is the so called geometrical blurring [42], due to the geometrical set up of the deposition apparatus as schematized in Fig. 2.2a. Briefly, a
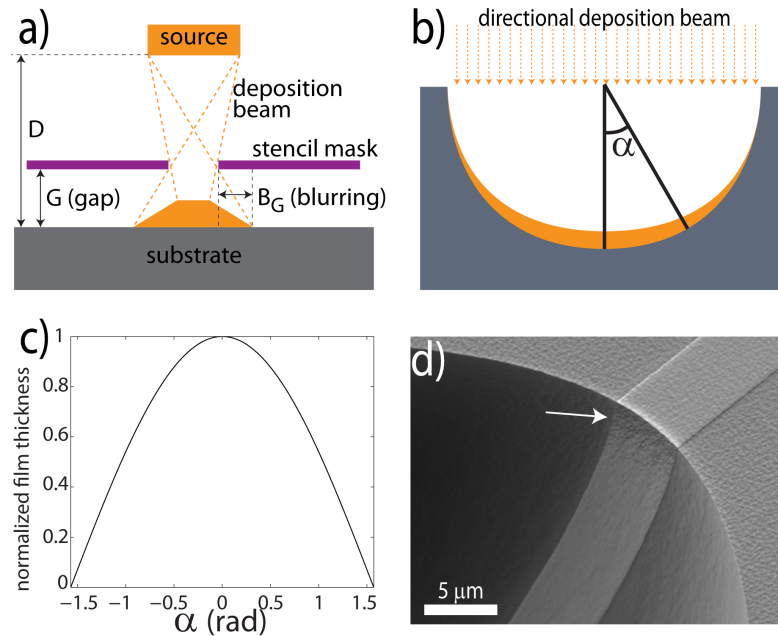


Figure 2.2: **a)**: schematics of the geometrical blurring ($B_G$) encountered in stencil lithography. This effect is due to the geometry of the deposition setup, and depends on the substrate-source distance (D), on the stencil mask-substrate gap (G), and on the divergence of the depostion beam. **b)**: highly directional deposition beams are routinely used in stencil lithography to reduce the blurring, but cause the deposited film to have a non homogeneous thickness over the angle $\alpha$. **c)**: normalized thickness as a function of the angle $\alpha$ (thickness $\propto \cos(\alpha)$). **d)**: SEM micrograph showing an Au stripe deposited inside a microwell, getting thinner and discontinuous close to the edge of the well, where the steepness of the surface is too high.

loss of resolution stems from and is proportional to the stencil-to-substrate gap $G$ and to the inverse of the substrate-to-source distance $D$. This is the reason why a long distance $D$ (i.e. a highly directional evaporation beam) is required when depositing through a stencil mask. However, the use of a collimated beam makes it impossible to deposit on vertical walls. In our specific case of an hemispherical well, one can expect to observe a vanishing film thickness when approaching the vertical edge of the well, as depicted in Fig. 2.2b.

In order to face this problem, it would be necessary to have non-hemispherical micro-wells, ending at an angle $\alpha < \pi/2$. The strategy adopted to fabricate this kind of micro-wells is sketched in Fig. 2.3, and consists in having two separate etching steps, named etch 1 and

etch 2. Si (100) wafers with a 200 nmSiN film are used. Circular apertures $a$ with $\varnothing = 10\,\mu m$
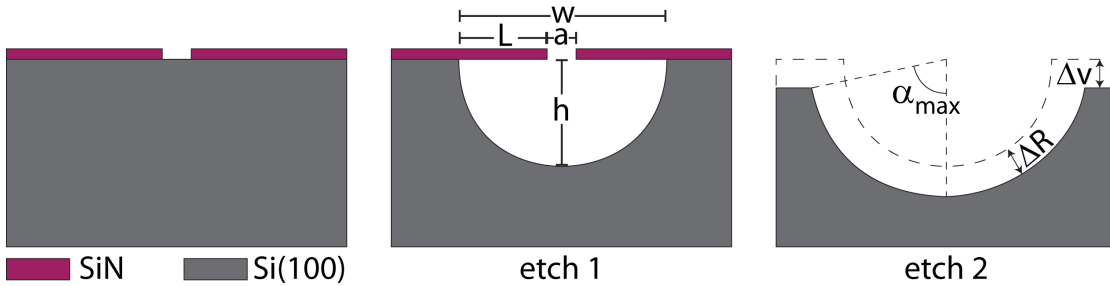


Figure 2.3: Two etching steps technique. **Left**: Si substrate with a SiN mask, in which an aperture is done with photolithography and dry etching (not shown). **Center**: isotropic etching through the aperture produces an almost hemispherical micro-well. **Right**: the second etching step, after removing the SiN mask, transforms the well shape from hemispherical to a more open cup, in which thin film deposition is possible up to the edges.

are made in the nitride layer, by means of photolithography and dry etching. SiN is then used as a mask during wet isotropic[1] etching of Si, done with HF/Nitric Acid (HNA [2]), with the following composition: HF(49%):HNO$_3$(70%):H$_2$O 3:50:20. Etching through a pinhole produces approximately an hemispherical micro-well. Even if we assume a perfectly isotropic Si etching (i.e. identical lateral etched length and vertical etched height, $L = h$) the finite size of the pinhole $a$ gives the micro-wells a shape which deviates from an hemisphere, since the width $w = 2L + a$ is more than twice the depth $h$, as shown in Fig. 2.3. This effect, however, can be neglected for the sizes used in practice, i.e. $w \approx 60\,\mu m \gg 10\,\mu m = a$. After having removed entirely the SiN mask (with dry etching), a second wet isotropic etching in NHA is performed. The radius of the well is increased by an amount $\Delta R$, but this time also the top surface is eroded, and moves down by an amount $\Delta h$.[3] In the end, the combination of the two etching steps (with and without SiN mask) produces wells that are no longer hemispheres, but spherical caps. The angle $\alpha_{max}$ at the edge with the flat surface of the wafer is decreased and is less then $\pi/2$, improving the deposition of metallic films close to the well border (Fig. 2.3). In

---

[1]The etching of Si with HF/Nitric Acid (HNA) is normally said to be isotropic at low HF concentration, when the reaction is diffusion limited. Despite this, a certain degree of anisotropy was observed during the experiment (even if we used a low HF concentration: HF(49%):HNO$_3$(70%):H$_2$O 3:50:20) and has been reported in literature few years ago [43].

[2]The acronym HNA stands both for HF/Nitric/Acetic acid, and for HF/Nitric acid/water, which are qualitatively equivalent etcher for Si, differing only in rate and tolerance for diluent variation[44, 45].

[3]Ideally $\Delta R = \Delta h$, but two phenomena make them different, reason why I used two different names for them. The two phenomena giving different etch rates at the top surface and within the well are: anisotropy of HNA etching and diffusion-limited etching [46] (due to the relatively low concentration of fluoride reactants with respect to the oxidizing nitric acid).

the following sections we characterized the evolution of the size and shape of the micro-well by varying the duration of etch 1 and etch 2. Our goals were:

1. proving the principle of shape control *via* two-steps etching;

2. find the appropriate etching times $t_1$ and $t_2$ to fabricate micro-wells with the desired shape and size, namely the ones necessary to fit the size of a single cell ($\varnothing \approx 50 - 60\,\mu m$) and to perform stencil deposition close to the steepest edge of the well ($\alpha_{max} < \pi/2$).

### 2.2.1 First Etching Step

A solution of HNA (HF(49%):HNO$_3$(70%):H$_2$O 3:50:20) at 20 °C was used in all the experiments of this chapter, which were performed in the clean room of the Center of MicroNanoTechnology of the EPFL (CMi). After having determined the approximate etching rate[4] with preliminary tests, three samples were etched with three different times, expected to give micro-wells with suitable dimensions. The dimensions we took into account for our analysis were the height (or depth) of the micro-well ($h$), the width ($w$), and the aspect ratio $h/w$. While the width can be easily measured from top using an optical microscope (Fig. 2.5), the quantification of the depth is more demanding. Standard mechanical profilometers cannot access the bottom of the wells, and optical profilometers fail when the steepness of the surface becomes too high, which is the case for the micro-wells fabricated in this work. Thus, we measure $h$ by taking cross section views of the micro-wells using a scanning electron microscope (SEM). Microwells cross sections were prepared by cleaving the wafers, and the first difficulty encountered with this technique is having the cross-secting plane passing in the middle of micro-wells. This problem is faced by cleaving a relatively long array of micro-wells. Since it is quite hard to have the cleaving plane perfectly aligned with the array, it happens that some of the micro-wells are crossed close to their mid-plane, as shown in Fig. 2.4a. Selecting the right cross sections is fundamental in order to have a reliable measurement of the depth. The wells that are cleaved close to their mid-plane can be selected since they are the ones with the deepest cross section $h_{max}$ of the array, as schematized in Fig. 2.4b.

---

[4]Remark about the reproducibility of the experiments: we observed a variation of the etch rate over time, on the scale of several days, probably due to the variation of reactants concentrations (evaporation and or consumption during etching). The reader willing to use the data on the etch rate, should make a test to determine it precisely before running any fabrication, and possibly check it even during fabrication.
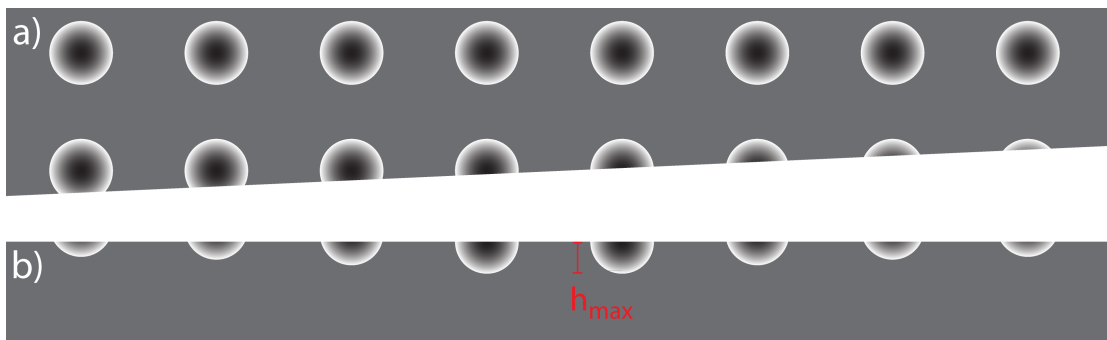
Figure 2.4: Microwells cleaving. **a)**: having the cleaving plane at an angle with respect to the array orientation, allows for some of the micro-wells to be cross-sectioned close to their mid plane. **b)**: the cross sections passing close to the mid plane can be chosen as the ones having the maximum depth $h_{max}$. .

The first observation done is that the so called isotropic HNA etching is not isotropic (Fig. 2.5). Quite surprisingly this phenomenon has been reported by Svetovoy *et al.* only in 2007
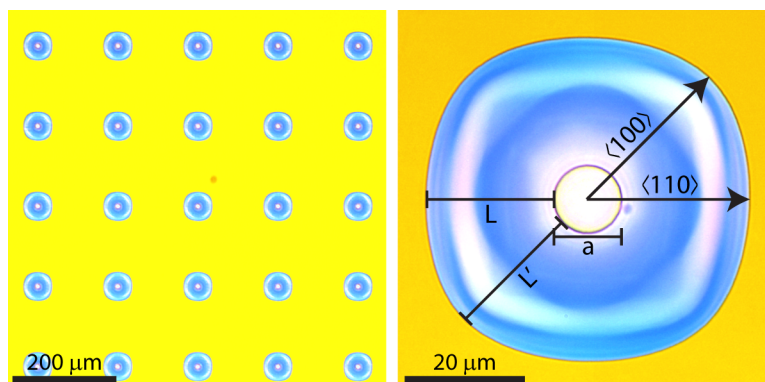


Figure 2.5: Etching anisotropy. **Left**: an array of Si micro-wells etched through the pinhole in SiN membrane. **Right**: close up of a single well, with the pinole aperture a clearly visible. The well etched below the SiN film appears to be light blue. Due to a higher etching rate along the $\langle 100 \rangle$ direction, the wells are not perfectly circular.

[43], while the technique was characterized in details already since the 60's [44, 45] and it is well established in the semiconductor industry. The anisotropy is mostly evident when comparing the etch rates along the $\langle 100 \rangle$ and the $\langle 110 \rangle$ directions, with the rate along $\langle 100 \rangle$ being about 7-8% faster than along $\langle 110 \rangle$. A similar 9% anisotropy is reported also by Svetovoy [43]. This has to be taken into account for the design of the shape of micro-wells. Indeed, the normal to the wafer surface is one of the $\langle 100 \rangle$ crystalline directions. This means that not only the contour of the well in the wafer plane is affected by the anisotropy (Fig. 2.5), but also their vertical cross section. Having a look at the SEM micrographs of Fig. 2.6, and at the related
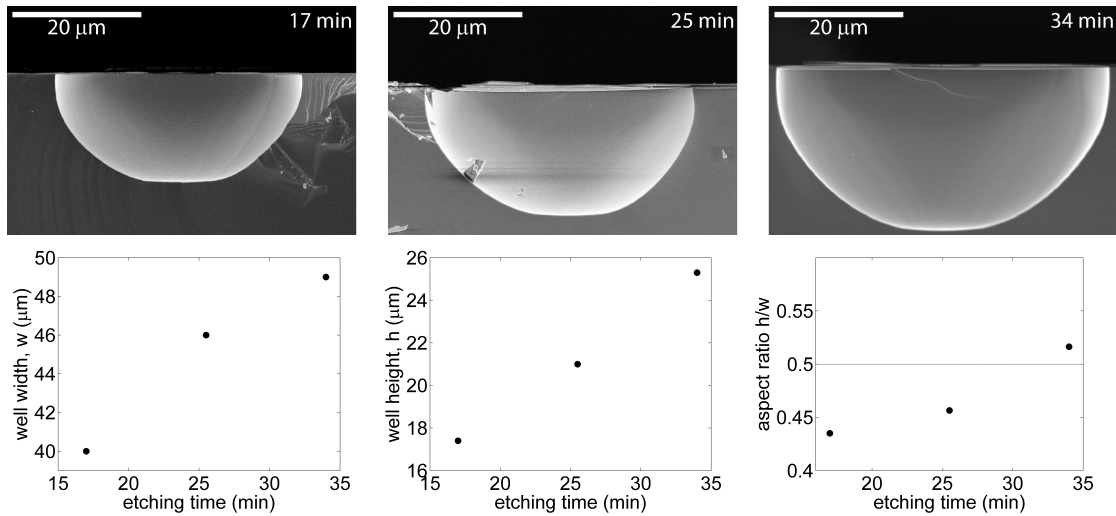
Figure 2.6: Characterization of the fist etching step. **Top**: left to right: SEM cross sections of micro-wells obtained by increasing etch 1 time. The effect of anisotropy is visible also in the cross sections. **Bottom**: left to right: graphs showing the evolution over time of the width ($w$), height ($h$) and aspect ratio ($h/w$), respectively. The height $h$, (which is along the $\langle 100 \rangle$ direction), grows faster than the width (which is along the $\langle 110 \rangle$ direction) due to the slight anisotropy of the HNA etch. This result in a shape evolution over time, instead of a simple scaling of the size, visible as an increase of the aspect ratio over time (last graph on the right).

graphs can better clarify this point. We can see that by increasing the etch 1 time from 17 to 34 min augments both the width and the height of the well by about $8\,\mu$m each, which is somehow unexpected for an isotropic etching. Indeed, one would expect the width to increase twice as fast as the depth, since it is etched both at its left and at its right sides at the same time. This leads to an increase of the aspect ratio $h/w$ for longer etching time, and not simply to a scaling of the micro-well shape. The third graph on the left (Fig. 2.6) shows this even better: for shorter etch 1 times (17 min) the aspect ratio is less then 0.5, i.e. the value expected for an hemisphere, due to the fact that the aperture $a$ contributes to the width by making it more than twice the depth ($w = 2L + a > 2h$ for shorter etching time, i.e. for relatively small $L$ and $h$). As the etching advances, though, the depth $h$ grows faster than $L$, overcompensating the contribution of $a$ and leading to an aspect ratio greater than 0.5 ($w = 2L + a < 2h$ for longer etching time, i.e. for relatively small $a$). This effect on the aspect ratio has to be taken into account more for the implications related to stencil deposition than for the shape of the well itself. Indeed, in the investigated range of sizes, interesting for single-cell studies, the shape is still quite close to an hemisphere and, most importantly, is 3D, which is the main goal.

19

The major problem could instead come from the deposition on the steepest portion of the micro-well sides: the part of well close to the edge is even steeper than it would be for a perfect hemisphere, as a consequence of the slower etching speed in the lateral direction $\langle 100 \rangle$. It turns out that the second etching step, already envisioned at the beginning of this chapter, is even more necessary due to anisotropy.

### 2.2.2 Second Etching Step

Before performing etch 2, the samples are rinsed in deionized water (DI water), dried with a nitrogen gun, and liberated from the SiN mask, by stripping it with an inductively coupled plasma (ICP) of $SF_6$. Then the etching in the same HNA solution is resumed. Three etch 2 times were tested: 5, 17 and 25 min. The effects of the second etching step over micro-well size and shape are presented here similarly to what was done for etch 1. As expected, the width keeps on increasing, even though at a pace which gets slower and slower. This is due to the reduction of the angle $\alpha_{max}$. At the beginning, for $\alpha_{max} = \pi/2$, the etching direction at the edge of the well is horizontal, meaning that the advancement of the etching front is horizontal as well, and it contributes entirely to an increase of the horizontal width $w$. Later, when the angle $\alpha_{max} < \pi/2$, the etching front at the edge of the well does not advance horizontally any more. Instead, it advances also downwards, perpendicularly to the edge surface (red arrow in Fig. 2.7D). This implies that the horizontal component of the etching advancement is reduced, and so does the growth rate of the width (Fig. 2.7, first graph on the left). The second graph shows the evolution of the depth $h$, which decreases over the etch 2 time. This effect can be attributed to the reaction being diffusion limited [46]. Indeed, the diffusion of reagents and reacted species to and from the bottom of the well is slower with respect to what happens for the open, flat surface of the wafer topside. This was anticipated in the schematics drawn in Fig. 2.3, where the etch rates of the flat surface and within the well were distinguished by using the two symbols $\Delta h$ and $\Delta R$, respectively. The fact that the etch rate of the flat, open surface of the wafer, $\Delta h$, is faster than the one inside the micro-wells, $\Delta R$, reduces the depth $h$ over time.

Figure 2.7: Characterization of the second etching step. **Top**: shape evolution for increasing etch 2 time $t_2$. **A)**: $t_2 = 0\,\text{min}$. **B)**: $t_2 = 5\,\text{min}$. **C)**: $t_2 = 17\,\text{min}$. **D)**: $t_2 = 25\,\text{min}$. The angle $\alpha$ at the edge of the wells is reduced, as envisioned for a better metal deposition on steep sidewalls. The magnifications of the SEM cross-sections are not constant, in order to display the micro-wells with the same width on the page and compare their shape disregarding the scale. During etch 2 the width w increases, as visible in the graph at the **bottom left** corner. **Bottom center**: the depth of the micro-well decreases (see text for more details), resulting in a significant variation of the aspect ratio, as desired (**bottom right**)

## 2.3 Stencil Fabrication and Stencil Deposition

As already mentioned, we used stencil lithography for the deposition of Au patterns inside the 3D micro-wells. The stencil mask used for this purpose was made out of a double side polished Si wafer with a 500 nm film of LS SiN grown on both of its faces. The fabrication process of such masks is illustrated in Fig. 2.8. Briefly, a photoresist mask is applied on top of



Figure 2.8: Stencil mask fabrication. **A)**: a photoresist mask is first made, with the designed apertures. **B)**: these apertures are transferred into a SiN film, *via* dry etching. **C)**: photolithography is preformed on the bottom of the wafer as well, and the SiN film is also etched as before **D)**. **E)**: DRIE is used in order to create an opening below the SiN front membrane, which is finally suspended using KOH etching **F)**.

the SiN film by means of spin coating and photolithography (Fig. 2.8A). Then, the photoresist sidewalls are transferred into the SiN layer *via* dry etching, using an ICP of $SF_6$ (Fig. 2.8B). After removing the photoresist, the same process is done on the backside of the wafer Fig. 2.8C-D), this time producing bigger apertures which work as frame for the membrane that will soon be freestanding. Silicon is then etched from the apertures fabricated on the backside, first with a reactive ion etching (RIE) process, which transfers the apertures vertically into the wafer (Bosch process, alternating plasma pulses of $SF_6$ and $C_4F_8$, Fig. 2.8E), and finally with a more gentle KOH wet etch, used to etch the last 30-50 μmof Si that hold the SiN film. Once the Si has been completely removed, a suspended membrane of SiN with microfabricated holes remains (Fig. 2.8F). On the sides of the wafers, a few dedicated membranes featuring alignment marks are prepared and used to align the stencil wafer onto the substrate containing micro-wells. Thin SiN films are transparent, so the alignment can be done with optical microscopes as usually done with Cr-masks, but using a dedicated chuck that clamps together the two wafers at the end of the alignment. This holder is then transferred into a PVD system, and a film of Ti-Au (thicknesses 8-80 nm) is deposited, with Ti acting as an adhesion layer. The same stencil mask can be cleaned from the deposited material (when necessary) and re-used more than once. Cleaning of the mask is performed first in a solution containing KI (25 g/l) and $I_2$
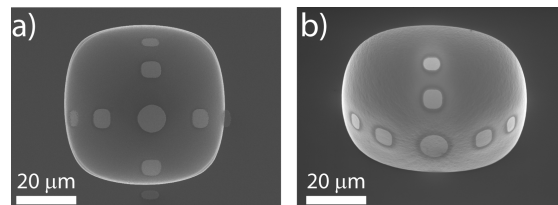


Figure 2.9: Alignment error in stencil lithography. An alignment error of ~ 1 μm have to taken into account even in the best case. **a)**: having micro-wells tightly fitted onto the pattern size, could cause a deposition exceeding the micro-well area. **b)**: slightly larger micro-wells should be preferred during design, in order for all of the patterns to be inside them.

(12 g/l) to etch Au, and later, after having rinsed the wafer in DI water, in a diluted solution of hydrofluoric acid (HF 1% vol. in water) which etches the Ti. Finally the mask is rinsed, again with DI water, and ready to be re-used. A second deposition has been made using the same stencil mask, but this time having a flat, unprocessed Si wafer as substrate. The same patterns as deposited in the micro-wells are thus readily reproduced on a 2D surface, simply by cleaning the stencil mask and reusing it. Figure 2.10 shows micrographs of the stencil mask

and of the deposited patterns in 2D and in 3D (inside the micro-wells).

Much care has to be taken during the alignment process, in order to center the patterns inside the well. Even the most careful operator, though, should consider an alignment error of at least 1 µm as normal. It is thus better to fabricate micro-wells that are slightly bigger than the patterns drawn on the stencil mask, allowing for this error (see Fig. 2.9). In this way, the deposited patterns will be all inside the micro-well, and not too close to the edges, where a discontinuous film could be deposited due to the steepness of the well (as shown in Fig. 2.2d).
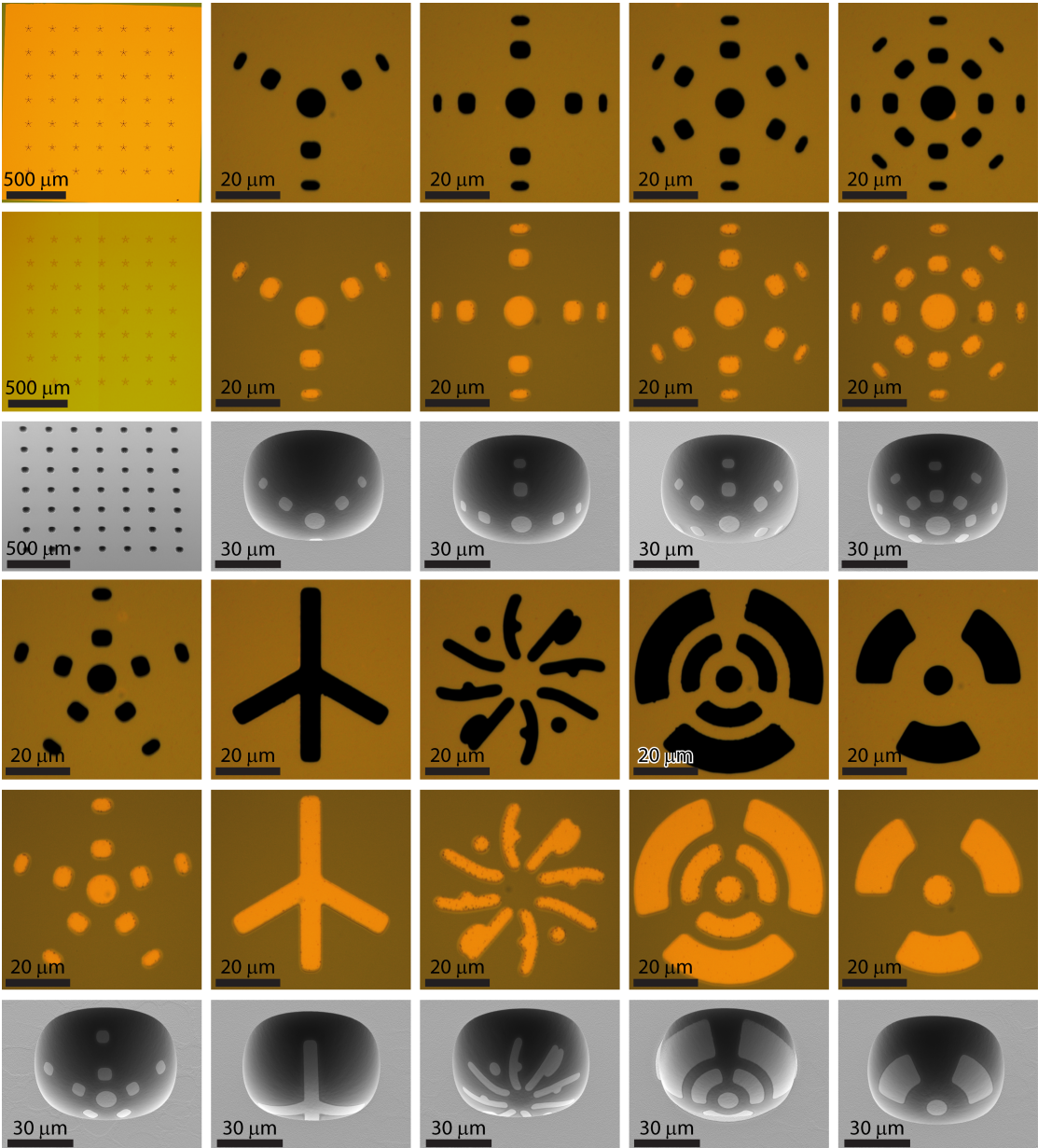
Figure 2.10: Optical micrographs of the SiN stencil mask with various apertures (lines 1 and 4). Optical micrographs of Au patterns deposited on a flat Si substrate through the stencil apertures (lines 2 and 5). SEM micrographs showing the same patterns deposited inside 3D Si micro-wells made by two-steps etching (lines 3 and 6).

# 3 3D Compliant Microstructures Based on Bent Cantilevers

## 3.1 Introduction

The behavior of cells is determined by the interplay between intracellular processes and extracellular environment. Besides biochemical factors, cells are also able to sense the mechanical and geometrical features of their surroundings via the activation of signal transduction pathways that in turn regulate DNA expression and cell responses to these external stimuli [47]. One of the reactions modulated by the mechanical properties of the cell culture substrate is the intensity of cell traction forces (CTFs) [48]. A common technique currently exploited to study CTFs makes use of soft gels with embedded fluorescent beads [33]. The strain field produced in the gel by CTFs is measured by imaging the displacement of the beads, and it allows for the retrieval of CTFs by means of various computational approaches [49]. In order to measure CTFs directly from displacements, Tan et al.[10] introduced another method based on elastomeric pillars, which bend under cell forces. Both techniques have been extensively used to measure CTFs of cells cultured on two dimensional (2D) substrates. However, it has been reported that cells are strongly affected by the dimensionality of their environment, in terms of their morphology, adhesions, migration, cytoskeleton organization, and response to mechanical properties [50, 21]. Moreover, all of the cells found in tissues *in vivo* are located in a three dimensional (3D) environment, and there exert contractile forces in order to fulfill basic biological functions such as adhesion, migration and tissue organization [51]. For this reason, methods based on fluorescent beads have been adapted for the use with cells cultured
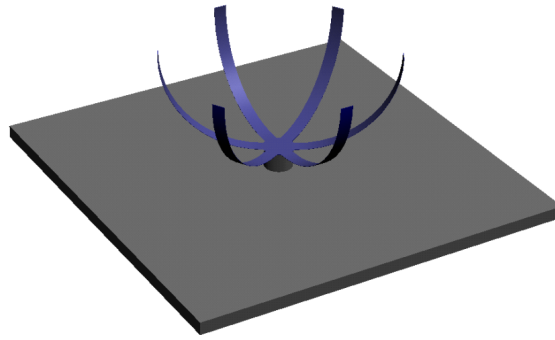
Figure 3.1: Schematic model of a μ-flower, a 3D device for cell culture, based on flexible bent cantilevers. Ideally, such a device should be designed and fabricated (i) to fit the size of single cells and (ii) to be pliable under CTFs, in order to mimic the rigidity of soft tissues and to allow for CTFs to be detected.

inside a 3D gel matrix, either to measure the strain energy of the gel [52], or CTFs [39]. The measurement of a full map of CTFs in 3D is however demanding in terms of imaging and computation [39]. Another approach for the study of cell mechanics in 3D has been proposed, which makes use of 3D-micropatterned environments [53]. As previously suggested [53], the use of micropatterned substrates for cell culture has the key advantage of simplifying the complexity encountered *in vivo* or in 3D reconstituted matrices, while retaining and mimicking some pivotal physical features, like the compliance and the 3D dimensionality. Indeed, in complex 3D environments many factors influence cell shape, cytoskeleton organization and CTFs generation, and the picture is further complicated by the fact that physical and biochemical properties are often correlated and can vary during remodeling of the extracellular matrix (ECM) [53]. In this framework, we developed a new 3D microdevice which allows for the direct measurement of CTFs. This device – named μ-flower after its shape (Fig. 3.1) – is composed of compliant cantilevers, which provide adhesion sites to hold the cell suspended in 3D, and allow cellular forces to be quantified. Analogous to microposts in 2D, bent cantilevers are the discrete and mechanically decoupled units of a 3D elastic microenvironment. This mechanical decoupling, together with the ability to localize cell adhesions on a defined pattern, allows forces to be measured directly from displacements, instead of being calculated from the interdependent strains of a continuous medium.

In the following sections the mechanics of bent cantilevers is introduced, covering the basics of stress-bent cantilevers, the calculation of the spring constants and the comparison between 2D elastic substrates and 3D discrete elements commonly used in cell traction force

microscopy (CTFM).

## 3.2 Mechanical Model of Stress-Bent Cantilevers

The pivotal point for the fabrication of µ-flowers is the exploitation of the built-in[1] stress of thin films.
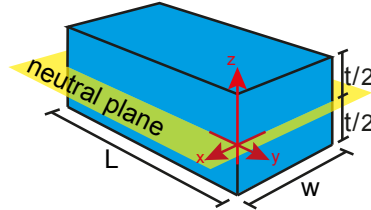


Figure 3.2: Frame of reference for a cantilever used in the calculations of this chapter. The z axis is taken to be normal to the width $w$ and to the length $L$ (i.e. normal to the film- substrate interface in the context of this work). The origin of the z axis is placed at the intersection with the neutral plane, i.e. in the middle of the film thickness $t$.

Indeed the cantilevers are shaped by means of surface microtechnology starting from stressed films (see section 4.2 and 5.2 for more details on the fabrication). Later, when the cantilevers are released from the substrate, the built-in stress makes them bending upward. To see why and how this bending takes place, let's consider a cantilever adhering on a thick substrate and holding a biaxial built-in stress $\sigma_{bi}(z)$ in the plane of the film ($xy$ plane) which is a function of the vertical position $z$ measured with respect to the neutral plane (see Fig. 3.2). The forces and bending moments generated by $\sigma_{bi}(z)$ are balanced by the substrate, which prevents the film from curling. After releasing the cantilever from the substrate (Fig. 3.3a), the built-in stress deforms the cantilever, until a new mechanical equilibrium position is reached with all the forces and moments cancelling out each other. Let's assume in our model, as done in the Euler-Bernoulli beam theory, that the deformations occur in the linear elastic regime (validity of Hooke's law, with stress and strain linearly bound to each other) and that plane sections of the beam remain plane upon deformation (Navier's hypothesis).

---

[1]In this work we refer to the stress present in a film deposited or grown on a substrate as the *built-in stress*. We avoid to use the term *intrinsic stress* as synonym, since it has often a more strict meaning in the literature, signifying only that particular component of the built-in stress stemming from the internal nano- and micro-structure of the film. The built-in stress could have other components beside the intrinsic one. It could e.g. include the thermal stress coming from the mismatch between the thermal expansion coefficients of the substrate and the film: $\sigma_{built-in} = \sigma_{intrinsic} + \sigma_{thermal} + \dots$.
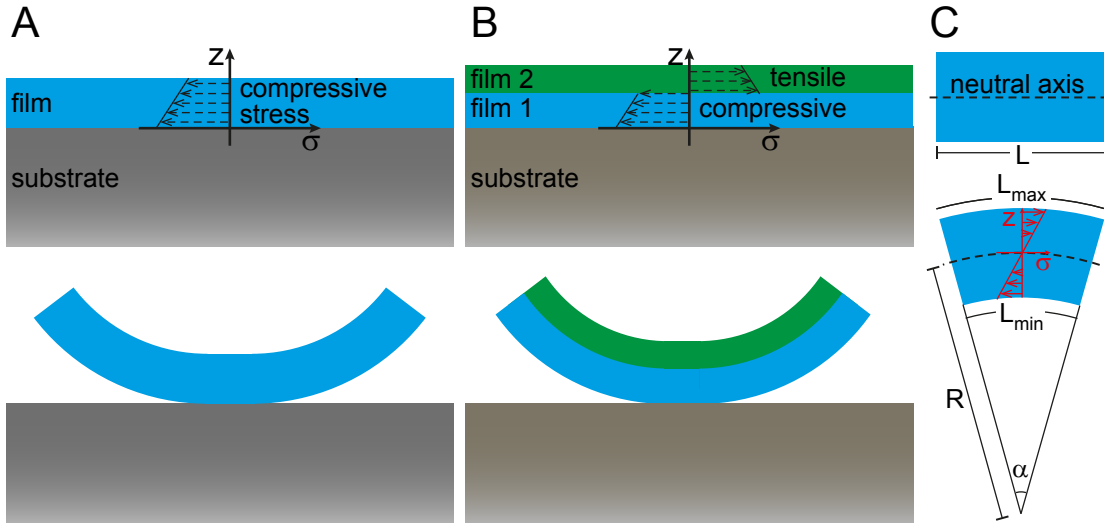
Figure 3.3: Stress and bending of thin films. (A) Top: Schematic of compressive stress with a linear gradient in a film deposited on a substrate; bottom: when the film is liberated from the substrate, the stress gradient provokes an upward bending. (B) bilayer deposited on a substrate and composed of a first film with compressive stress and of a second film with negative stress; bottom: after release the opposed stresses both contribute to an out-of-plane bending. (C) Top: schematic of a beam at rest. Bottom: when the beam is subject to bending, the strain generate a stress $\sigma_{bend}(z)$ which is tensile toward the convex surface of the beam, and compressive toward the concave surface (red graph).

As shown in figure 3.3c, the fact that plane sections remain plane means that rectangular beams bend and become circular under the force and moment given by the built-in stress. This deformation induces a strain $\varepsilon_{def}(z)$ and a stress $\sigma_{def}(z) = E\varepsilon_{def}(z)$ in the beam, which counteract the built-in stress $\sigma_{bi}(z)$ until equilibrium is reached (being $E$ the Young's modulus of the material). As it will become clear in few lines, the deformation strain is composed of a constant strain and a bending strain, the latter being a linear function[2] of $z$:

$$\varepsilon_{def}(z) = \varepsilon_c + \varepsilon_{bend}(z). \tag{3.1}$$

Considering that the length $L$ of the cantilever at the neutral axis is unchanged after the bending occurs — by definition of neutral axis — and that the angle $\alpha = L/R$, it follows from figure 3.3c that the stress $\sigma_{bend}(z)$ induced by the bending strain is expressed by the equation:

---

[2]The fact that the strain has a linear dependence on $z$ is a logical consequence of Navier's assumption that plane sections remain plane, as can be seen in Fig. 3.3c.

$$\sigma_{bend}(z) = E\varepsilon_{bend}(z) = E\frac{\Delta L(z)}{L} = E\frac{L(z) - L}{L} = E\frac{\alpha(R+z) - L}{L} = E\frac{R+z}{R} - 1 = \frac{E}{R}z, \quad (3.2)$$

where $\Delta L(z)$ is the elongation of the beam along a plane at a distance $z$ from the neutral axis, and $L(z)$ is the length of the beam after deformation, along the same plane. Let's consider now the situation in which static equilibrium is reached after releasing the pre-stressed cantilever from the substrate. The total force and moment have to be null:

$$\begin{cases} 0 = F = \int_{-t/2}^{t/2} w(\sigma_{bi}(z) + \sigma_{def}(z)) \, \mathrm{d}z \\ 0 = M = \int_{-t/2}^{t/2} wz(\sigma_{bi}(z) + \sigma_{def}(z)) \, \mathrm{d}z \, , \end{cases} \quad (3.3)$$

where $w$ is the width of the beam and $t$ its thickness. By substituting $\sigma_{def}(z)$ with $E\varepsilon_{def}(z)$, and using equations 3.1 and 3.3 for further substitutions, we can write the following:

$$\begin{cases} \int_{-t/2}^{t/2} \sigma_{bi}(z) \, \mathrm{d}z = -\int_{-t/2}^{t/2} \sigma_{def}(z) \, \mathrm{d}z = -\int_{-t/2}^{t/2} E\varepsilon_c \, \mathrm{d}z - \cancel{\int_{-t/2}^{t/2} \frac{E}{R}z \, \mathrm{d}z} = -E\varepsilon_c t \\ \int_{-t/2}^{t/2} z\sigma_{bi}(z) \, \mathrm{d}z = -\int_{-t/2}^{t/2} z\sigma_{def}(z) \, \mathrm{d}z = -\cancel{\int_{-t/2}^{t/2} zE\varepsilon_c \, \mathrm{d}z} - \int_{-t/2}^{t/2} z^2 \frac{E}{R} \, \mathrm{d}z = -\frac{Et^3}{12R} \, , \end{cases}$$

where we have separated the built-in stress contribution and the deformation contribution. The two struck through integrals are equal to zero due to the symmetry of the integrand function with respect to $z$. It follows directly from the static equilibrium conditions that the deformation strain $\varepsilon_{def}(z) = (\varepsilon_c + \varepsilon_{bend}(z)) = (\varepsilon_c + z/R)$ of a released cantilever is characterized by the following parameters:

$$\begin{cases} \varepsilon_c = -\frac{\int_{-t/2}^{t/2} \sigma_{bi}(z) \, \mathrm{d}z}{Et} = -\frac{<\sigma_{bi}>}{E} \\ R = -\frac{Et^3}{12\int_{-t/2}^{t/2} z\sigma_{bi}(z) \, \mathrm{d}z} \end{cases} \quad (3.4)$$

It is now clear, after having solved the equilibrium conditions, that the total strain has two components, as hypothesized in equation 3.2:

- $\varepsilon_c$ which is constant through all the thickness of the cantilever. This strain corresponds to an elongation (or shortening) of the entire cantilever, which counterbalances the average compressive (or tensile) built-in stress $<\sigma_{bi}>$. Considering that typical values

of the built-in stress are in the order of few hundreds of MPa, and that values of $E$ are in the order of few hundreds of GPa, $\varepsilon_c$ is in the order of 0.1%, provoking a negligible variation of the length of the beam.

- $\varepsilon_{bend}(z) = z/R$ with $R$ given in equation 3.4. This strain comes from the bending of the cantilever under the moment generated by the built-in stress $M_{bi} = \int_{-t/2}^{t/2} z\sigma_{bi}(z)\,\mathrm{d}z$. It is evident that a built-in stress which is constant throughout the thickness $z$ ($\sigma_{bi}(z) = \sigma_{bi}, \forall z$) would give a null bending moment $M_{bi} = 0$ and hence a flat cantilever ($R = \infty$). In order **to have a small bending radius, it is** thus **important for the built-in stress to have a significant gradient with respect to** $z$, while the absolute value of the stress doesn't affect the bending at all (it only changes $\varepsilon_c$).
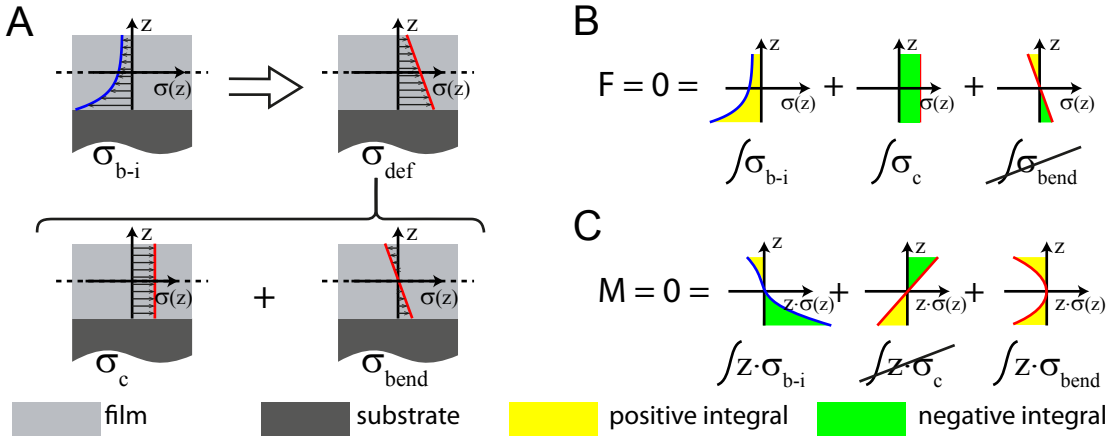


Figure 3.4: The built in stress $\sigma_{bi}$ deforms the cantilever, until equilibrium is reached (see equation 3.3). A) shows a schematics of the equilibrium between the built-in stress $\sigma_{bi}$ of a cantilever (blue line) and the stress due to its deformation $\sigma_{def}$ (red lines). The deformation stress can be decomposed (i) in a constant component $\sigma_c$, due to an elongation (or shortening) $\varepsilon_c$ of the entire cantilever, counterbalancing the average built-in stress $<\sigma_{bi}(z)>$, and (ii) in another component $\sigma_{bend}(z)$ linear with respect to $z$ and due to cantilever bending. B) and C) show the equilibrium conditions for the total force $F$ and bending moment $M$ respectively, which link the built-in stress with the bending radius of the cantilever (see equations 3.3, 3.4 and text for more details).

A gradient of the built-in stress is practically observed in all thin films, and we exploited it to engineer the bending of cantilevers. This stress inhomogeneity is a reasonable phenomenon when thinking that a thin film has one face bound to the substrate and the other face free of constraints. Beside this, also the growth (or deposition) of thin films takes place along the vertical $z$ axis (normal to the substrate surface), affecting in this way the microstructure of the

film, its strain and stress along $z$.

## 3.3  Validity of Beam Model

The model used in section 3.2 to describe the relation between built-in stress and curvature might differ significantly from reality, in case our assumptions and approximations were not valid. They are checked in this sections, by criticizing analytically our model. For this purpose, we need to know the material elastic properties (namely the Young's moduli $E$) and the geometrical parameters (radius $R$ and thickness $t$).       While using Euler-Bernoulli beam theory, we assumed the validity of Hooke's law for stress and strain ($\varepsilon = E\sigma$). This means that the strains generated during bending lay within the elastic regime of materials, without reaching the yield strength or the fracture strength, in case of ductile or brittle materials respectively.[3] One of the materials used for the fabrication of bent cantilevers is thermally grown $SiO_2$ (section 4). The yield strength of thin silica films has been measured with tensile tests on micro-structures, resulting in a value of $\sigma_{yield} = 364 \pm 57\,\text{MPa}$ [54]. The maximum tensile stress caused by bending is experienced by fibers on the convex surface of a cantilever, (equation 3.2, and Fig. 3.5). The highest tensile stress experienced by the bilayer cantilevers made in the framework of this thesis can be estimated by taking the thicker $SiO_2$ layer (180 nm), and assuming that the neutral plane $z = 0$ lays at the interface between Ti and $SiO_2$. In this case we have a value of $z = z_{max} = 180\,\text{nm}$ at the external surface of bent cantilevers, where the maximum tensile stress due to bending is reached. Moreover, we anticipate here that the smaller bending radius achieved is $R \approx 30\,\mu\text{m}$ (see section 5.3.1) and that $E_{SiO_2} = 60\,\text{GPa}$ is a reasonable value for thermally grown wet-$SiO_2$ thin films [55, 56]. These values, together with equation 3.2, lead to an upper estimation of $\sigma_{bend,max}(z) = \sigma_{bend}(z_{max}) = 360\,\text{MPa}$ for the tensile stress, very close to the measured fracture strength $\sigma_{yield}$. However, this is not the maximum total stress experienced by the external fibers of the $SiO_2$ layer. Indeed, these same fibers are the ones retaining the highest intrinsic compressive stress before releasing the cantilever from the substrate ($\sigma_{intrinsic} \approx 200$ to $300\,\text{MPa}$), being the ones at the Si-$SiO_2$

---

[3]Ductile materials under load, e.g. Ti, are characterized by a linear elastic regime, until a certain load, named yield strength, is reached. For loads higher than this yield, the material undergoes a plastic deformation before breaking. On the other hand, brittle materials, e.g. $SiO_2$, do not show the ability to absorb strain energy in a plastic regime. They are characterized as well by a linear elastic regime, but they break all of a sudden when the fracture strength is reached, without experiencing a plastic regime before fracture.
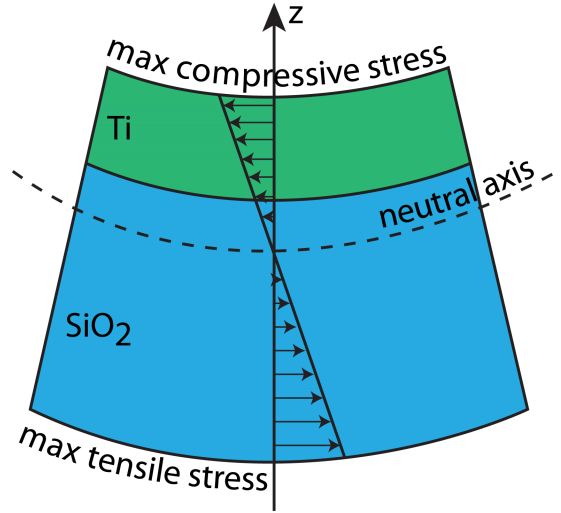
Figure 3.5: Schematics of a Ti-SiO$_2$ bilayer cantilever as the ones fabricated in the context of this work. Due to bending, tensile and compressive stresses are generated in planes laying below and above the neutral plane, respectively. Since the bending stress depends linearly on the distance $z$ from the neutral axis, the maximum stresses are generated at the concave and convex surfaces of the beam. The bending stress, due to cantilever deformation, should not be confused with the intrinsic stress present in the films, and causing bending.

interface (see section 4.1). The resulting total stress $\sigma_{tot} = \sigma_{bend} - \sigma_{intrinsic}$ is thus safely lower than the fracture strength, thanks to the fact that, during bending, the compressive intrinsic stress of SiO$_2$ is released while the bending tensile stress builds up. Let us now have a look to the Ti thin film present in the bilayer cantilevers. As shown in Fig. 3.5, the bending stress of Ti $\sigma_{bend}(z)$ is compressive. For thin films, the measurement of the compressive strength[4] is technically more complicated than the measurement of tensile stress. This is the reason why in the literature it is not easy to find measures of the compressive strength for Ti thin films. Conversely, direct measurements of the tensile yield have been performed on Ti films, giving values from 700 to 800 MPa [57, 58]. Let us assume, as it is the case for bulk metals, that the compressive strength has the same magnitude as the tensile yield, which can be used as a benchmark to check the validity of the beam model previously used. The maximum stress of Ti can be calculated similarly to what was done for SiO$_2$. Assuming a value $z_{max} = 150$ nm (distance between Ti surface and neutral axis), a bending radius $R = 30$ nm, and a Young's modulus $E_{Ti} = 128$ GPa [58], we get from equation 3.2 that $\sigma_{bend,max}(z) = \sigma_{bend}(z_{max}) = $

---

[4]The compressive strength is the stress at which a material under compressive load fails (e.g. experiencing a plastic deformation). For ductile materials, like metals, the compressive strength is usually similar to the tensile yield.

600 MPa. Since the film already has a tensile intrinsic stress $\sigma_{intrinsic}$ before bending, and since $\sigma_{bend}$ is opposed to it, the total tensile stress left is well within the yield strength of Ti thin films. These worst-case estimations corroborate the hypothesis of elastic deformations (Hooke's law) for both $SiO_2$ and Ti.

The other assumption holding Euler-Bernoulli theory is Navier's hypothesis (plane sections of the beam remain plane and normal to the beam axis upon deformation). It is valid for beams that have a span and a bending radius at least 10 times bigger than the thickness [59], which is the case for the cantilevers used in this work ($t \approx 100$ to $200\,nm$, $R > 20\,\mu m$, and $L > 30\,\mu m$).

## 3.4 Computation of the Spring Constant and Considerations on Cell Force Measurements

We introduce here, in the context of bent beam mechanics, the calculation of the spring constant, which will be used later to characterize mechanically the fabricated devices. Of particular interest is the application of bent cantilevers to CTF measurements, presented in chapter 6. The technique is based on the localization of cellular focal adhesions (FAs) in pre-defined areas along the cantilever, namely at the end and in the middle. This localization is achieved by using Au spots deposited on the cantilevers and functionalized to enhance cell adhesion. These Au spots are called distal Au spot and proximal Au spot, respectively, as shown in Fig. 3.6a. The cantilever parameters used in this chapter to carry out the calculations (i.e. radius, materials and thicknesses) are the same of the cantilevers used in chapter 6 for CTF measurements, due to their relevance within this dissertation.

Considering the bent cantilever shown in Fig. 3.6a and making use of Castigliano's second theorem, it is possible to calculate the deflection $\delta x$ produced by a horizontal force $F$ applied either at the proximal Au spot or at the distal one. The following calculations are derived from the analysis of the deflection of curved beams carried out in *Roark's Formulas for Stress and Strain* [59] (section 9.2, p. 275 of the $7^{th}$ edition). The theorem states that $\delta x = \partial U(F)/\partial F$, being $U(F)$ the strain energy of the cantilever expressed as a function of the applied load $F$. Since the angular span of the cantilever is much bigger than its thickness, the strain energy

can be approximated with the energy of flexure $U_f$ of a straight beam:

$$U \approx U_f = \int_0^{l_i} \frac{M^2(l)}{2EI}\, \mathrm{d}l \tag{3.5}$$

with $l_i = l_P$ or $l_D$ respectively, $E$ expressing the Young's modulus of the cantilever, $I$ the second moment of area and $M^2(l)$ being the bending moment generated by the load $F$ at any point $l$ along the cantilever length.
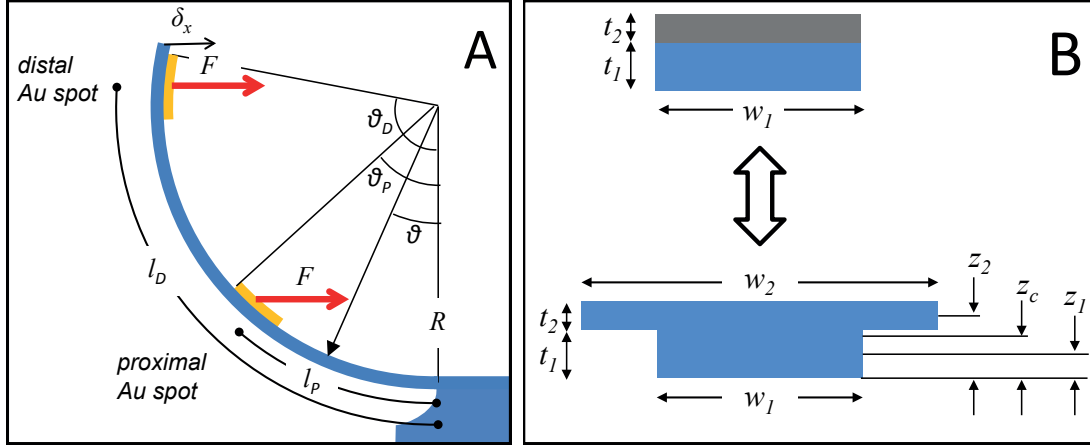


Figure 3.6: **A**: Schematic of a bent cantilever used for the calculation of the spring constants experienced by horizontal forces applied at the distal Au spot and at the proximal Au spot. **B** Scheme showing the mechanical equivalence between a bilayered cantilever with rectangular section and a T-shaped cantilever made out of one single material.

Denoting the angular position of any section of the cantilever by $\vartheta = l/R$, it is evident that the moment is $M = FR(\cos\vartheta - \cos\vartheta_i)$, with $\vartheta_i = l_i/R = \vartheta_P$ or $\vartheta_D$ respectively. Substituting $dl$ with $Rd$ we have:

$$U \approx U_f = \int_0^{l_i} \frac{[FR(\cos\vartheta - \cos\vartheta_i)]^2}{2EI} R\, \mathrm{d}\vartheta \tag{3.6}$$

Instead of solving the integral and then doing the partial derivation $\delta x = \partial U/\partial F$, it is convenient to differentiate first and then integrate:

$$\delta x = \frac{1}{EI} \int_0^{\vartheta_i} FR^3 (\cos \vartheta - \cos \vartheta_i)^2 \, \mathrm{d}\vartheta$$

$$= \frac{FR^3}{EI} \int_0^{\vartheta_i} \cos^2 \vartheta - 2 \cos \vartheta_i \cos \vartheta + \cos^2 \vartheta_i \, \mathrm{d}\vartheta$$

$$= \frac{FR^3}{EI} \left[ \left( \frac{\vartheta}{2} + \frac{\sin \vartheta \cos \vartheta}{2} \right) - 2 \cos \vartheta_i \sin \vartheta + \vartheta \cos^2 \vartheta_i \right]_0^{\vartheta_i}$$

$$= \frac{FR^3}{EI} \left[ \frac{\vartheta_i}{2} - \frac{3 \cos \vartheta_i \sin \vartheta_i}{2} + \vartheta_i \cos^2 \vartheta_i \right] \tag{3.7}$$

Once the displacement $\delta x$ is known, the spring constant for an applied horizontal force $F$ can be calculated as

$$k = \frac{F}{\delta x} = \frac{EI}{R^3 \left( \frac{\vartheta_i}{2} - \frac{3 \cos \vartheta_i \sin \vartheta_i}{2} + \vartheta_i \cos^2 \vartheta_i \right)} \tag{3.8}$$

To compute $k$ we need to calculate the second moment of area $I$ for the bilayer cantilever. For this purpose an equivalent T-shaped cross section is developed (see Fig. 3.6b), made out of a single material ($SiO_2$), with thicknesses $t_1$ and $t_2$ equal to the original bilayer thicknesses, and with the width of the second layer increased by the ratio between the Young's moduli: $w_2/w_1 = E_{Ti}/E_{SiO_2}$ [59] (section 8.2, p. 137 of the $7^{th}$ edition). Being $z_1$ and $z_2$ the positions of the neutral axis of the two elements and $t_1$ and $t_2$ the thicknesses of these same elements, we can calculate the neutral axis $z_c$ of the equivalent T-shaped beam:

$$z_c = \frac{z_1 w_1 t_1 + z_2 w_2 t_2}{w_1 t_1 + w_2 t_2} \tag{3.9}$$

Having $z_c$ and knowing that $I_i = w_i t_i^3 / 12$ we can calculate the second moment of area of

the equivalent T-shaped beam:

$$I = I_1 + w_1 t_1 (z_1 - z_c)^2 + I_2 + w_2 t_2 (z_2 - z_c)^2 \tag{3.10}$$

For the fabricated cantilevers used in the CTF experiment (section 6.1) we have a radius $R = 28\,\mu m$, an arc $l_P = 20\,\mu m$ and $l_D = 50\,\mu m$, a width $w_1 = 5\,\mu m$, and thicknesses $t_1 = 104\,nm$ and $t_2 = 59\,nm$. Taking $E_{SiO_2} = 66\,GPa$ [60] and $E_{Ti} = 116\,GPa$ (value for bulk Ti) and carrying out the computation for $k$ we obtain:

$$k_P = 313\,nN/\mu m$$
$$k_D = 5.5\,nN/\mu m \tag{3.11}$$

Hence if a force is applied to the proximal Au plate, the displacement would be about 2% of the displacement generated by the same force when applied to the distal Au plate. For this reason we divide the cantilevers in two sets during data analysis: one set with cells adhering to the proximal Au spot – for which we don't expect significant displacements – and another one with cells adhering to the distal Au spot – for which we expect measurable displacements. When computing the spring constant, the main sources of uncertainty are the values of the Young's moduli and the thickness of the cantilever. Young's moduli of very thin metal films, as the one fabricated in the context of this work, are known to be dependent on the particular process used during the fabrication, on the substrate on which the films are deposited, as well as on the thickness of the films themselves, with variations of $E_{Ti}$ that can be in the order of 30% [58, 57]. For these reasons a lot of care has to be taken when using data from the literature or from tabulated values for bulk materials. The other most significant source of uncertainty is the thickness of the $SiO_2$ film composing the cantilevers. It has been precisely measured with a spectroscopic reflectometer (see section 5.2, but the subsequent etching process, performed to release the cantilevers, could have modified its initial thickness. In order to quantify the uncertainty on $k$, two extreme cases have been compared:

(i) a maximum value of 128 GPa for $E_{Ti}$ [58] and a completely unaffected SiO$_2$ layer;

(ii) a minimum value of 90 GPa for $E_{Ti}$ [57] associated with a 20% reduction of the SiO$_2$ layer.

We obtain for $k$ the following asymmetric uncertainties:

$$k_P = 313^{+13}_{-127} \text{ nN/}\mu\text{m}$$

$$k_D = 5.5^{+0.2}_{-2.2} \text{ nN/}\mu\text{m} \tag{3.12}$$

To quantify forces more precisely it would be required to overcome this uncertainty, by a direct calibration of the spring constant. It would be also necessary to determine the direction of the force vector, since the effective $k$ constant depends on it. Anyway the ratio $k_P/k_D$ for horizontal forces like the one in Fig. 3.6a is independent on these uncertainties, since they would change the values of both $k_P$ and $k_D$ by exactly the same factor. Hence the considerations done about the division of the data in two sets, one for proximal and one for distal adhesions, are not undermined.

## 3.5 Comparison with 2D Elastic Substrates

One of the first quantitative studies on CTFs was carried out on 2D substrates, constituted by continuous elastic gels [2]. The technique became a cornerstone in the domain of CTFM, and various studies make use of 2D continuous substrates. The use of these substrates is even more diffused outside the domain of CTFM, where hydrogels and other polymers with tunable mechanical properties are used to investigate the effects of stiffness on cells. The key parameter charachterizing 2D elastic substrates is the elastic (or Young's) modulus $E$. On the other hand, microstructured substrates with discrete elastic elements (such as, e.g., micro posts arrays [10] and $\mu$-flowers) are charachterized by the spring constant $k$ of their discrete micro-mechanical components (pillars or cantilevers). It is thus fundamental to find a way to convert spring constant values $k$ to equivalent values of the elastic modulus $E_{eff}$ [61], with

the aim to compare the mechanical properties of continuous and discrete substrates, and the results obtained with the two techniques.
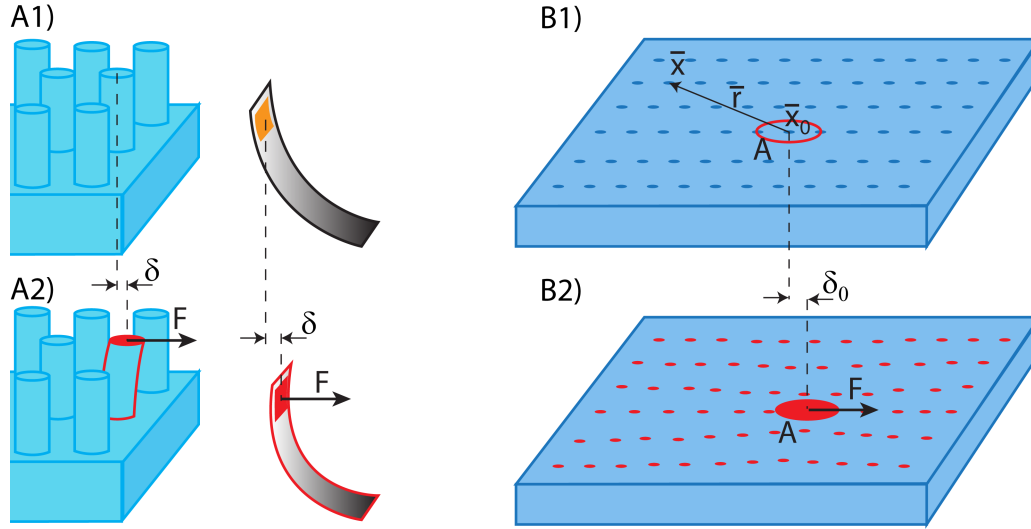


Figure 3.7: Mechanical equivalence between micro-structured substrates with discrete components and a continuous 2D substrate. **A1)**: pillars and cantilevers are the discrete elements of microstructured substrates, such as micro post arrays and μ-flowers, respectively. **A2)**: when a force $F$ is applied to one single element, it is displaced by an amount $\delta$, without the other decoupled components being moved. **B1)**: a continuous elastic substrate with a force $F$ applied over an area $A$ centered around $x_0$. **B2)**: all the points $x$ of the surface of the substrates are displaced, following a continuous strain field proportional to $1/r$.

The first thing to notice is that the two kinds of substrates have fundamentally different mechanical behaviours. When a force is applied on a continuous elastic medium at a point $x_0$, all of its points are displaced, with a strain field going as $1/r$ (Landau and Lifschitz, *Theory of Elasticity*, p. 29 II edition [62]), where $r = |\boldsymbol{r}| = |\boldsymbol{x}_0 - \boldsymbol{x}|$ is the distance between the point $x_0$ and any other point $\boldsymbol{x}$ at the surface of the elastic substrate (see Fig. 3.7). Instead, when a force is applied on a discrete element of a micro-structured surface, the displacement field is localized to that element only, while the surface of the other components stay still, these elements being mechanically decoupled.[5] We will say that a continuos and a micro-structured substates are mechanically equivalent when the same force $F$, applied to both of them, generates identical displacements $\delta$ (see Fig. 3.7). For a discrete element (pillar or cantilever beam) with a stiffness

---

[5]For the sake of precision, individual pillars of poly(dimethylsiloxane) (PDMS) in micro-post arrays are not completely decoupled. They do interact via the elastic substrate, with a small deflection affecting even these pillars on which no force is directy applied. The effect of this cross-talk has been analyzed in depth by Schoen [63], and it is negligible for the typical dimensions of the posts used in literature.

$k$, $F$ and $\delta$ are bound together by Hooke's law

$$\delta = F/k. \tag{3.13}$$

For a continuous substrate, that we model as a semi-infinite elastic and incompressible (Poisson's ratio $\nu = 0.5$) medium, things are less straightforward than Hooke's law. As said, the displacement is distributed to each point $x$ of the surface as follows:

$$\boldsymbol{\delta}(\boldsymbol{x}) = \frac{3}{4\pi E r}\left[\boldsymbol{F} + (\boldsymbol{n}\boldsymbol{F})\boldsymbol{n}\right], \tag{3.14}$$

with $\boldsymbol{n} = \boldsymbol{r}/r$. A first look to equation 3.14 tells us that $\boldsymbol{\delta}(\boldsymbol{x_0}) = \lim_{\boldsymbol{x}\to\boldsymbol{x_0}} \boldsymbol{\delta}(\boldsymbol{x}) = \infty$. This non-physical outcome is a consequence of the non-physical condition of having a force $\boldsymbol{F}$ concentrated in a single point $\boldsymbol{x_0}$. In reality, a force is applied over a certain area $A$ with finite dimensions, and it is more appropriate to talk about the shear stress $\boldsymbol{f} = \boldsymbol{F}/A$, assumed to be homogeneous over $A$. In our model, $A$ is the area of a cellular FA, which we assume to be circular, with radius $a$ and centered in $\boldsymbol{x_0}$ (see Fig. 3.7). Now the strain $\boldsymbol{\delta}(\boldsymbol{x_0})$ at the center of the FA is no more diverging, and can be calculated as:

$$\boldsymbol{\delta}(\boldsymbol{x_0}) = \iint\limits_A \frac{3}{4\pi E r}\left[\boldsymbol{f} + \frac{(\boldsymbol{r}\boldsymbol{f})\boldsymbol{r}}{r^2}\right] \mathrm{d}S = \frac{9\boldsymbol{P}a}{4E}. \tag{3.15}$$

In order to find the value $E_{eff}$ of the effective Young's modulus corresponding to a given $k$, it is sufficient to equate equations 3.13 and 3.15, substituting $P$ with $F/\pi a^2$:

$$\delta = |\boldsymbol{\delta}(\boldsymbol{x_0})| \implies E_{eff} = \frac{9}{4\pi a}k. \tag{3.16}$$

Attention has to be paid to the fact that there is not a univocal correspondence between $k$ and $E_{eff}$. Indeed, they are linked via the value of $a$, i.e. via the typical dimension of FAs on a continuous 2D substrate. This ambiguity can be circumvented with some empirical considerations. Indeed, FAs areas on flat substrates with various compliances have been measured to be in the range of 2 to 3 $\mu m^2$ [64]. This corresponds to a typical FA radius $a$ of 0.8

to $1\,\mu$m. We can thus simplify the second equation 3.16 as

$$E_{eff}\,[\text{kPa}] \approx 0.7 \times k\,\left[\text{nN}\,\mu\text{m}^{-1}\right],\tag{3.17}$$

with $E_{eff}$ and $k$ expressed in terms of the commonly used units of kPa and nN $\mu\text{m}^{-1}$. It has to be kept in mind that this approximate equivalence is held by the hypothesis of circular FAs[6] and by the empirical observation $a \approx 1\,\mu$m.

---

[6]FAs usually have an elliptical shape, with the long axis in the same direction of actin fibers pulling on them, and with a length to breadth ratio $\approx 3$ [64].

# 4 Bent Cantilevers: 1st generation (SiO$_2$ monolayer)

## 4.1 Choice of Material: Thermally Grown SiO$_2$

The presence of stress in thin films is a very common phenomenon, but with a number of different origins, e.g. lattice mismatch (in case of epitaxial films); boundaries between crystalline domains; nano-structure of the film (columnar growth, embedded voids), change in molar volume after oxidation, etc. However, not all of the stressed films are suitable for the micro-fabrication of bent cantilevers. For example, the growth of epitaxial crystalline layers is a well characterized and controllable process, but the intrinsic stress is not isotropic in the plane of the film, taking different magnitudes along different directions, due to the crystalline nature of the film [65]. For many other growth method, the intrinsic stress is difficult to be precisely controlled, since it depends on a number of variables[66]. Let us consider, as an example, the case of physical vapor deposition (PVD). The structure of the film at the nanoscale, and hence its intrinsic stress, is dependent on the collimation of the evaporation beam (which in turns depends on the distance source-substrate), on the temperature of the substrate, on the vacuum level reached inside the deposition chamber, on the deposition rate, and on the thickness of the deposited layer, just to name the main parameters. Not all of these parameters are easily controllable, standardized and reproducible. E.g., the geometry of the PVD setup and the kind of source used (thermal or e-beam) vary from one machine to another, making it very difficult, if not impossible, to draw a consistent picture and extrapolate a solid model from the results found in literature. The lack of a systematic and precise knowledge about

stress control is, in a first instance, a deterrent for the use of this technique. Even more so in the context of the present work, where it would be necessary to control the stress profile all along the film thickness[1] (control of $\sigma(z), \forall z$), and not only the average value of the stress $\langle \sigma(z) \rangle$, which is the quantity normally reported by the vast majority of the studies in literature.

Beside stress control and reproducibility there are other cornerstone criteria that have to be taken into account for the choice of the cantilever material. Namely, a good candidate should fulfill the following requirements:

- presence of a stress gradient $\Delta\sigma(z)$;

- control over the stress magnitude and profile;

- reproducibility of the stress profile;

- biocompatibility;[2]

- possibility to be functionalized or passivated with biomolecules.

SiO$_2$ owns all of these properties and was selected as a building material. Si$_3$Ni$_4$ is another interesting biocompatible material for microelectromechanical system (MEMS) [68], with controllable stress [69]. Despite this, SiO$_2$ has a higher stress to Young's modulus ratio, making smaller bending radii more easily attainable ($R$ is directly proportional to the Young's modulus $E$, as shown in equation 3.4, and $E_{Si_3N_4} \approx 5 \times E_{SiO_2}$ [70], while the stress magnitude in the two materials are similar [69, 70]). The second and most important reason why SiO$_2$ was preferred is the availability of protocols for its passivation against cell adhesion [71, 72], which were also used in a previous work of ours [14].

Let us have a closer look to the stress profile in thermally grown SiO$_2$. The use of SiO$_2$ films as insulating layer in the semiconductor industry made it very important to characterize and

---

[1]It is indeed the stress gradient $\Delta\sigma(z) \neq 0$ that defines the bending radius, as detailed in section 3.2.

[2]Biocompatibility is a somehow ambiguous term, according to the domain and the specific application it is used for. The IUPAC gives two definitions [67] (i) **Biocompatibility (biomedical therapy)***: Ability of a material to perform with an appropriate host response in a specific application*; and a more general definition (ii) **Biocompatibility***: Ability to be in contact with a living system without producing an adverse effect*. It is thus clear that the biocompatibility of a certain material is not an absolute property, but it depends on the living system it is used with and on the application it is used for. A material could be biocompatible with respect to a living system (e.g. cells), but not with respect to another one (e.g. an organism). In the context of this thesis, a material is considered biocompatible if it is suitable as a substrate for cell culture, without inducing toxic reactions.

predict the thermal growth processes of silica on Si wafers. Deal and Grove [73] proposed a famous model to describe the SiO$_2$ growth dynamics in both wet and dry oxidation processes. According to it, the growth time $t$ to obtain an SiO$_2$ thickness $h$ is given by

$$t = \frac{h^2}{B} + \frac{h}{B/A}. \tag{4.1}$$

The quantities $B$ and $B/A$ are often called the quadratic and linear reaction rate constants respectively,[3] even though they are functions of the temperature $T$ (expressed in kelvin in the following equations):

$$B(T) = B_0 e^{-E_B/KT} \tag{4.2}$$

$$B(T)/A(T) = (B/A)_0 e^{-E_{BA}/KT}. \tag{4.3}$$

$E_B$ and $E_{BA}$ are the activation energies and $K$ is the Boltzmann constant. The quadratic and linear coefficients are defined by the following parameters in the case of wet thermal oxidation on (100) Si wafers[74]:

$$B_0 = 386\,\mu\text{m}^2/\text{h} \qquad\qquad E_B = 0.78\,\text{eV}$$

$$(B/A)_0 = 9.7 \times 10^7\,\mu\text{m}\,\text{h}^{-1} \qquad\qquad E_{BA} = 2.05\,\text{eV}. \tag{4.4}$$

The continuous race to miniaturization in metal-oxide-semiconductor (MOS) technology led to the use of SiO$_2$ layers of decreasing thickness. For very thin layers, the growth dynamics deviates from the Deal and Grove model, due to the effect of the intrinsic stress, which reduces the diffusivity of the oxidant molecules into SiO$_2$, thus slowing the oxidation rate. The need to characterize also this regime of growth led to an increased knowledge of the intrinsic stress generated during thermal oxidation. Fargeix and Ghibaudo [75] found an analytical expression

---

[3]The linear coefficient is expressed as the ratio $B/A$ instead of being written as a single coefficient. The reason behind this is that $B$ and $A$ are more fundamental coefficients in the Deal and Grove model, being derived by physical quantities. More specifically: $A = 2D_{eff}(1/k_1 + 1/k_2)$, $B = 2D_{eff}CN_1$, with $D_{eff}$ = effective diffusion coefficient of the oxidant in the oxide; $k_1$ = oxidation reaction coefficient at the Si-SiO$_2$ interface; $k_2$ = gas absorption coefficient at the oxidant-SiO$_2$ interface; $C$ = equilibrium concentration of the oxidant in the atmosphere; $N_1$ = oxidant molecules per unit volume needed to produce a unit volume of the oxide.

describing the stress profile in an SiO$_2$ layer of thickness $h$:

$$\sigma_{int}(h,z) = \sigma_{max} \exp\left[ -\frac{z}{\tau\left(\frac{2h-z}{A} + \frac{1}{B/A}\right)^{-1}} \right].$$ (4.5)

This stress profile is defined by the linear and parabolic coefficients of the Deal and Grove model (equation 4.4), and by $\sigma_{max}$, which represents the maximum stress, at the Si-SiO$_2$ interface.

The physical phenomena giving rise to stress is the **molar volume expansion** in the transition $Si \longrightarrow SiO_2$. Indeed, the volume of one mole of crystalline Si expands by $\approx 2.16$ times upon oxidation, due to oxygen uptake. Since the growing oxide is bound to the underlying Si, it is not free to expand, and hence it remains under compressive stress. The second phenomenon playing a crucial role in shaping the intrinsic stress of thermally oxidized SiO$_2$ is **stress relaxation**. At the high temperatures used in the furnaces (typically around 900 to 1000 °C) silicon dioxide is a viscoelastic solid that can be modeled as a Maxwell material [75]. Under constant strain, as it is the case for the oxide bound to the substrate, the stress of such a material relaxes exponentially with time:

$$\sigma(t) = \sigma_{max} e^{-t/\tau}$$ (4.6)

$$\tau = \frac{\eta}{\mu},$$ (4.7)

where the damping constant of time relaxation (Maxwellian time) $\tau$ is given by the viscosity $\eta$ and the shear modulus $\mu$. An infinitesimal layer d$z$ of SiO$_2$ is under the maximum compressive stress $\sigma_{max}$ right after it is oxidized, due to molar expansion. Thereafter the stress begins to decrease exponentially as a consequence of viscous flow relaxation (Fig. 4.1 a).In the meanwhile, the oxidation keeps on going by reacting the next Si layer. The layer d$z$ gets thus a bit farther from the advancing Si-SiO$_2$ interface while it relaxes its stress. This explains the formation of a stress profile with a maximum value $\sigma_{max}$ at the Si-SiO$_2$ interface, which decreases away from it. Since the growth rate (i.e. the speed of the advancing Si-SiO$_2$ interface) is not constant (equation 4.1), the stress profile $\sigma(z)$ is not simply exponential, but it is characterized by a decay length which varies with $z$: $\tau[(2h-z)/A + 1/(B/A)]^{-1}$ (equation 4.5). Fig. 4.1 b shows five stress profiles according to Fargeix, for five different temperatures in

a)
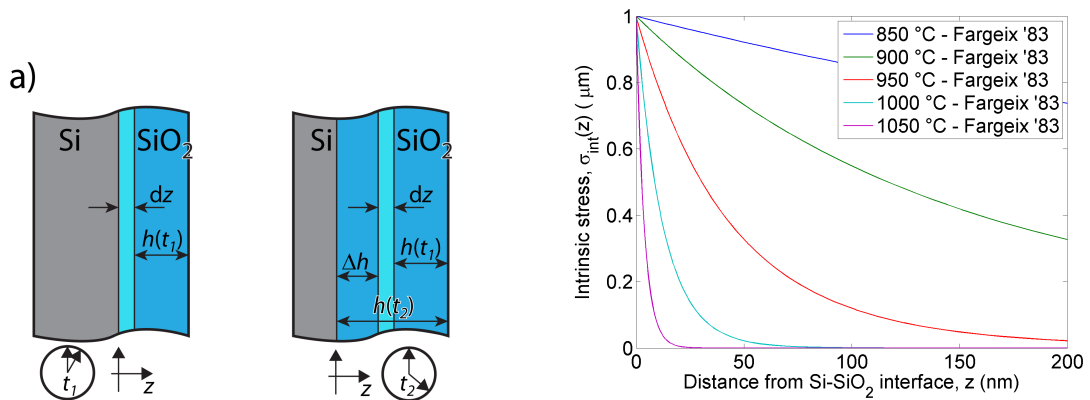


Figure 4.1: **a):** schematics of SiO$_2$ thermal growth. A new layer d$z$ of oxide gets farther away from the Si-SiO$_2$ interface while the oxidation advances. During this time its intrinsic stress decreases due to viscous relaxation. **b):** intrinsic stress profiles after oxidation, according to Fargeix and Ghibaudo [75]. For higher temperatures the viscous relaxation becomes faster than the growth rate, relaxing most of the stress away from the Si-SiO$_2$ interface (set at $z = 0$). At lower temperature the relaxation time $\tau$ become longer, and the stress is only partially relaxed upon growth.

the case of wet oxidation. At higher temperature the relaxation time becomes shorter than the growth time, and the stress away from the Si-SiO$_2$ interface gets quickly relaxed. At lower temperature, conversely, the stress takes a longer time to relax, due to a higher viscosity $\eta$. That is the reason why a significant amount of stress is still present throughout all the oxide thickness.

### 4.1.1 Expected Bending Radius and Spring Constant

Once the material to be used for the fabrication of cantilevers has been identified, it still remains the question of which parameters should be used during fabrication. The values to be optimized during the preparation of μ-flowers are the bending radius of the cantilevers $R$, and their spring constant $k$. [4] The geometrical constraint comes from cells' dimension. Our goal is to make a device which matches in size a single cell, more specifically mouse fibroblasts, which are about 60-70 μm in breadth when spread onto flat substrates. This translates into having a target radius $R \approx 30$μm, as a rule of thumb. The mechanical properties of bent

---

[4]When referring to the spring constant, we mean the one calculated for a bent cantilever of length $L = 2\pi r/4$ (i.e. of a cantilevers with the shape of a quarter of circumference) and for a force applied perpendicularly to the cantilever tip.

cantilevers are another unavoidable constraint when designing and developing μ-flowers, since the mechanical features of the cell culture substrates strongly affect cell behavior, e.g. adhesion, cytoskeleton organization, migration, traction force generation, and differentiation of stem cells [76]. Beside mimicking the stiffness of physiological tissues, we also aimed to fabricate cantilevers that are soft enough to be deflected by a measurable amount[5] under the load of cell traction forces (CTFs), in order to use the μ-flowers as force gauges. Physiological tissues have a wide range of stiffnesses, ranging from $\approx 1$ to $100\,$kPa [77], while cells are able to generate forces up to some tens of nN [10, 78]. It follows from these values that a spring constant[6] $k$ in the order of approximately 1 to $10\,$nN/μm is suitable for both cell traction force measurements and mechanical mimicry of soft tissues (e.g. muscle tissue has been measured to be around $10\,$kPa for mice [79]). In summary, the target values we are aiming for are:

$$R_{\text{target}} = 30\,\mu\text{m}$$

$$k_{\text{target}} = 10\,\text{nN}\,\mu\text{m}^{-1}. \tag{4.8}$$

In a cantilever made out of thermal oxide there are three parameters that can be readily selected in order to tune the bending radius and the spring constant, namely:

- the thickness of the beams, $h$,

- the width, $w$,

- the oxidation temperature, $T$.

It is thus important to select the fabrication parameters $h$, $T$ and $w$ in such a way to attain $R$ and $k$ close to our target values. In order to choose the parameters, we performed a simulation, calculating the expected values of $R$ and $k$ based on the stress model developed by Fargeix [75] and on the bent cantilever model presented in section 3.4. A model stress profile $\sigma_{int}^{h,T}(z)$ is calculated for a given oxide thickness $h$ and for a certain temperature $T$, according to equation 4.5. Then, the bending radius $R(h,T)$ for this couple of parameters $(h,T)$ is computed by

---

[5] In the context of this work the goal was to measure deflections with an optical microscope, e.g. deflections in the order of a μm.

[6] For the mechanical equivalence between the spring constant and the Young's modulus of a continuous elastic substrate, see section 3.5.

integrating $\sigma_{int}^{h,T}(z)$ over $z$, as done in equation 3.4. Knowing $R(h,T)$, the spring constant $k(h,T,w)$ can be calculated right away from equation 3.4.[7] $k(h,T,w)$ depends linearly on the width $w$ (i.e. $k(h,T,w) = k(h,T)w$) and this permits us to simplify our assessment of the expected values. Indeed, we fixed $w = 5\,\mu m$ in all the performed calculations, in such a way to have both $R$ and $k$ depending only on the two parameters $(h,T)$. The expected spring constant for any other value of $w \neq 5\,\mu m$ can be immediately estimated due to the simple linear relation between $k$ and $w$. Four values of the oxide thickness have been considered in the simulations (50, 100, 200 and 300 nm), and for each of them the expected values $R_h(T)$ and $k_h(T)$ have been computed for $850\,°C < T < 1000\,°C$. The results are plotted in Fig. 4.2. An interesting
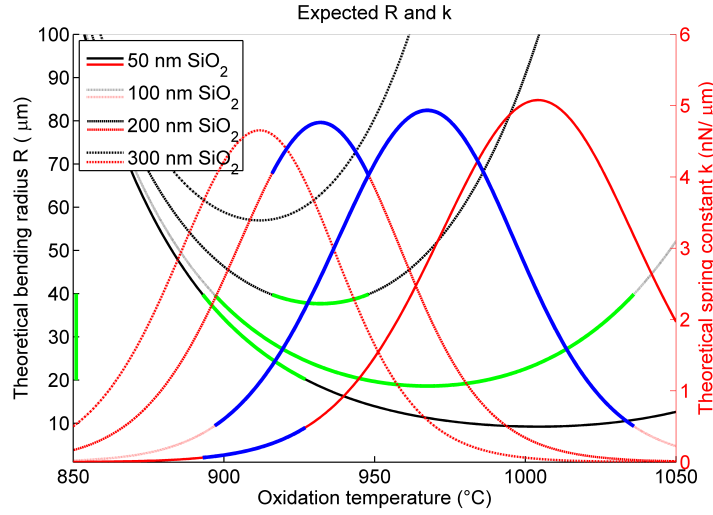


Figure 4.2: Simulated values of $R_h(T)$ (black curves, left vertical axis) and $k_h(T)$ (red curves, right vertical axis), over the temperature range from 850 to 1000 °C. Four simulations have been performed, for four values of $h$, as shown in the legend. The green segments on the $R_h(T)$ curves show the values $20\,\mu m < R_h(T) < 40\,\mu m$, relatively close to the target value of $30\,\mu m$. The blue segments on the $k_h(T)$ curves highlight the spring constants corresponding to the green segments on the $R_h(T)$ curves.

range of values for $R_h(T)$, centered around the target of $30\,\mu m$, has been highlighted in green for each of the curves, and the spring constants corresponding to these selected segments are highlighted in blue. The thinnest oxide layer considered ($h = 50\,nm$) is predicted to have values of $R$ in the good range at a relatively low temperature around 900 °C. However, the spring constants attainable for these radii and for such a thickness are low compared to CTFs [10].

---

[7]In these simulations all the bent cantilevers have been modeled as tracing a quarter of circumference, i.e. the angle $\vartheta_i = \pi/2$ in equation 3.4, and the Young's modulus has been taken as $E = E_{SiO_2} = 60\,GPa$.

Instead, the curves simulated for a thickness of 100 and 200 nm have a range of temperature for which both the radius and the spring constant fall inside an interesting interval. When the thickness is further increased ($h = 300$ nm) the attainable radii are too big, and no longer suitable for single-cell devices. We finally chose to work with 200 nm thick SiO$_2$, because (i) 100 nm SiO$_2$ is an extremely thin layer for wet oxidation (very fast process, less control); (ii) a 200 nm layer could be possibly thinned later via etching, in case it would turn out to be too thick (as it was indeed the case as it will be shown later in section 4.3.3), while a too thin layer would not be easily thickened.

## 4.2 Fabrication of SiO$_2$ Bent Cantilevers

The fabrication of bent cantilevers is done by means of surface microtechnology. All the processes described here and in section 5.2 have been carried out in the clean-room facility of the Center of MicroNanoTechnology of the EPFL (CMi).

The process is performed on test grade Si(100) wafers. First, an RCA cleaning[8] is done in order to remove all the possible organic and metallic contamination from the wafer surface, and prevent that they affect the subsequent high temperature oxidation by diffusing into the wafer. Afterwards, a wet thermal oxidation process is done in a furnace, at a temperature ranging from 850 °C to 1050 °C. Five temperatures in this range have been tested, in five different oxidation runs, spanning the whole temperature interval by steps of 50 °C. Briefly, the wafers are loaded inside the furnace at a temperature of 700 °C, and a linear heating ramp is done at a speed of 10 °C/min until the oxidation temperature $T_{ox}$ is reached (see table 4.1).

Then, highly pure water-steam generated with an oxyhydrogen torch[9]is injected into the chamber, in order to perform the oxidation. As shown in Fig. 4.3, the dry oxidation dynamic is about 20 times slower than the wet one, due to the lower diffusivity of O$_2$ with respect to H$_2$O

---

[8]The RCA cleaning consists of three subsequent cleaning steps. The first step has the purpose to remove organic contaminants and particles from the surface of the wafer, and it is done in a solution composed by 5 parts of deionized water (DI water), 1 part of aqueous NH$_4$OH and 1 part of aqueous H$_2$O$_2$, at 75 or 80 °C typically for 10 minutes. The second step (optional) consists of a quick immersion in a HF:H$_2$O solution (1:100 or 1:50) at 25 °C, for about 15 seconds. The third and last step is performed by immersion in a solution composed by 5 parts of DI water, 1 part of aqueous HCl (hydrochloric acid, 39% by weight) and 1 part of aqueous H$_2$O$_2$ at at 75 or 80 °C typically for 10 minutes.

[9]Highly pure water steam is achieved by ignition of gaseous O$_2$ and H$_2$, keeping O$_2$ slightly in stoichiometric excess, to be sure to completely oxidize all the hydrogen (O$_2$ flow = 8.33 SLM, H$_2$ flow = 16 SLM.

| STEP | T [°C] | H$_2$ flow [SLM$^a$] | O$_2$ flow [SLM$^a$] | N$_2$ flow [SLM$^a$] | rate [°C/min] |
|---|---|---|---|---|---|
| LOADING | 700 | 0 | 0 | 20 | — |
| RAMP UP | 700 → $T_{ox}$ | 0 | 0.5 | 10 | 10 |
| OXIDATION | $T_{ox}$ | 16 | 8.33 | 0 | — |
| RAMP DOWN | $T_{ox}$ → 700 | 0 | 0 | 10 | −4 |
| UNLOADING | 700 | 0 | 0 | 20 | — |

Table 4.1: Parameters used for SiO$_2$ growth. T$_{ox}$ indicates the final temperature at which oxidation is performed. It was varied between 850 °C and 1050 °C, in steps of 50 °C.
$^a$ Standard Liters per Minute, unit to measure gas mass flow. It corresponds to 1 liter of gas at the standard pressure and temperature conditions of $10^5$ Pa and 0 °C.

in SiO$_2$ [80, 73], and hence is much more expensive. For this practical reason the wet process has been preferred, although a more exhaustive literature exists for dry oxidation and for the stress profile obtained with this technique [81, 82, 75, 83, 84]. Viscoelastic stress relaxation of SiO$_2$ is taking place during wet oxidation as well, being caused by high temperatures. A stress gradient $\nabla \sigma(z) \neq 0$ is thus present also in SiO$_2$ grown by wet oxidation, and gives the moment needed for cantilever bending.
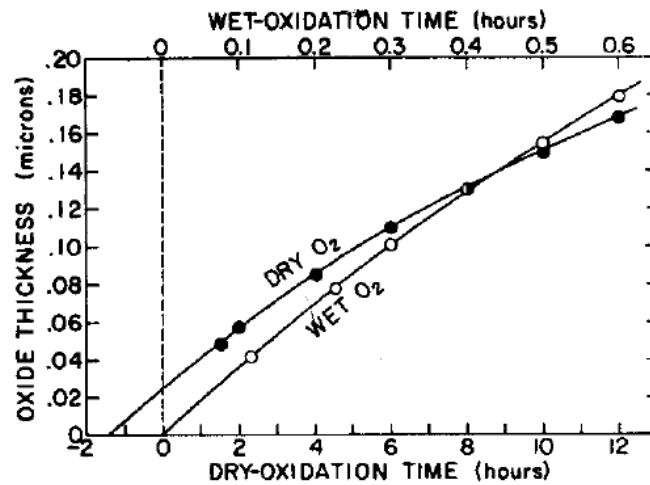


Figure 4.3: Dynamic of the thermal oxidation of silicon, according to the model proposed by Deal and Grove [73]. Different oxidation times have to be used at different temperatures, in order to obtain the same final thickness. The dynamic of dry oxidation is much slower, making the process more expensive.

After growth of SiO$_2$, a photolithographic process is done in order to shape the cantilevers. A Cr mask was designed and fabricated with direct laser writing, always in the clean room facility of CMi, containing the layouts of various cantilevers to be transferred onto the wafer.

In order to do so, a photoresist film is spun onto the oxidized wafer, the Cr mask is placed in contact with it, using a mask aligner, and ultra violet (UV) light is shined through the Cr mask onto the wafer, exposing selectively the photoresist. Later, the photoresist is developed, removing all the exposed areas (Fig. 4.4 - 2).Then, the SiO$_2$ layer is etched by means of reactive
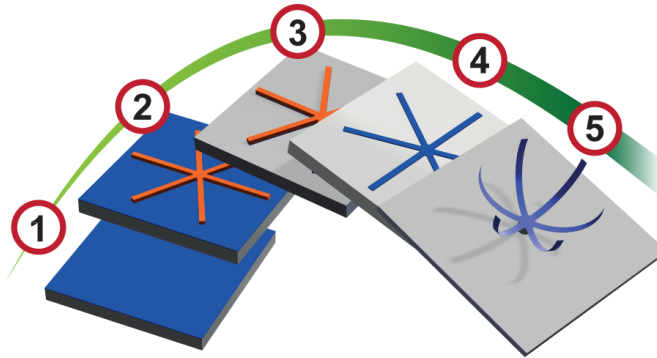


Figure 4.4: Schematics showing the basics steps for the fabrication of bent SiO$_2$ cantilevers. 1) wet thermal oxidation of a Si wafer; 2) photolithography; 3) SiO$_2$ dry etching to transfer the photoresist mask into the oxide layer; 4) photoresist removal; 5) cantilever release by dry etching of the Si substrate.

ion etching (RIE), using a plasma from C$_2$F$_6$ gas, generated in an inductively coupled plasma (ICP) etching system (Alcatel 601E). The photoresist acts as a protective mask, and preserves the underlying oxide, shaping the cantilevers on top of the wafer (Fig. 4.4 - 3). Later the photoresist is removed with wet solvents prior to releasing the SiO$_2$ cantilevers from the Si substrate. This last step is done by isotropic etching of Si, by means of a plasma generated from sulfur hexafluoride gas (SF$_6$), in the same ICP system used for SiO$_2$ etching. While liberating the cantilevers from the cooled Si substrate, their thermal coupling with it is decreased. Thus, in order to avoid excessive heating of cantilevers, a relatively low power and longer process was used for Si etching (ICP coil power: 800 W, power of substrate bias: 0 W).

## 4.3 Characterization of SiO$_2$ Bent Cantilevers

### 4.3.1 Bending Radius vs. Oxidation Temperature

After fabrication, we measured the variation of bending radius as shown on 4.5. Panel a) on the left is a photomontage of the same kind of structures made out of SiO$_2$ grown at different temperatures. Panel b) shows a typical cross-section of the structures, used for the

measurement of the bending radii. $R$ can be derived straightforwardly from $L$ and $h$, applying Pythagoras' theorem on the green triangle of Fig. 4.5 c):

$$
\begin{aligned}
(R-h)^2 + L^2 &= R^2 \\
\Rightarrow R &= \frac{h^2 + L^2}{2h}
\end{aligned}
\tag{4.9}
$$
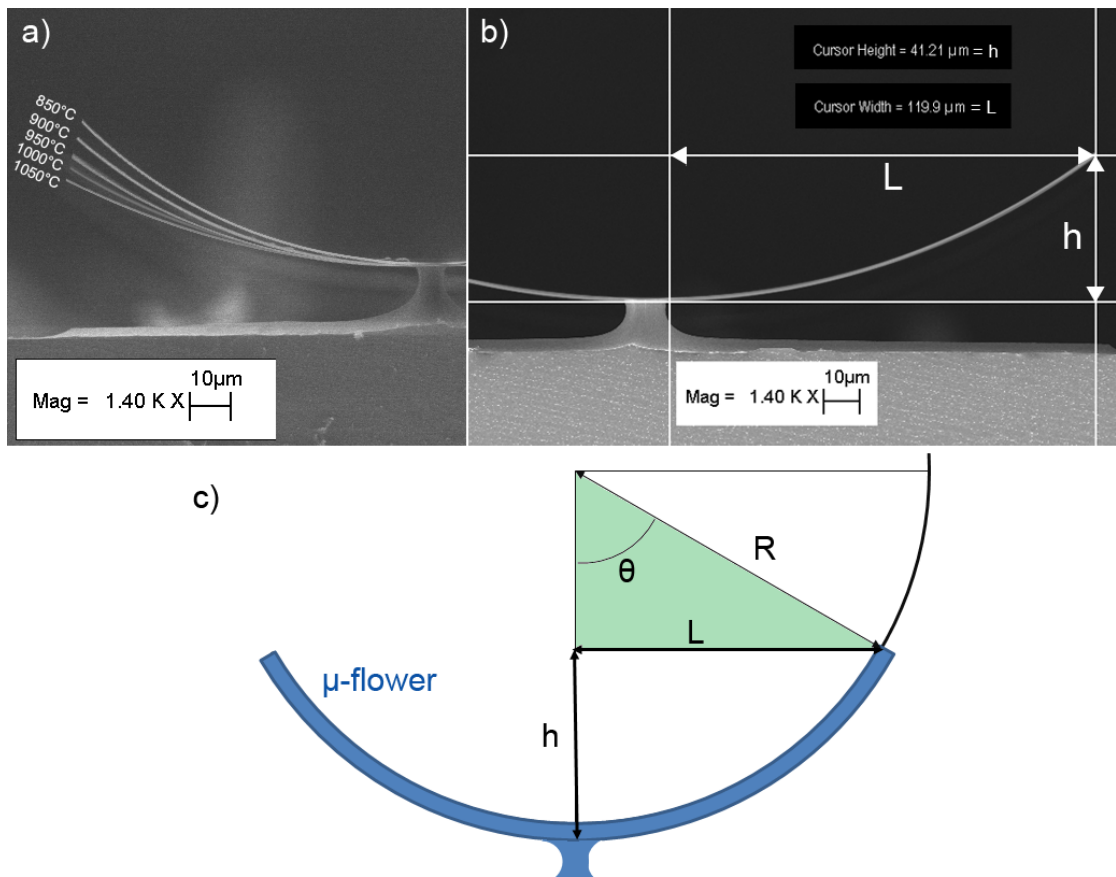


Figure 4.5: a) shows a photomontage of different cantilevers made from SiO$_2$ oxidized at different temperatures. b): a typical picture used for radius measurement. c) shows a schematics with the trigonometric relations used to calculate the bending radius.

L and h have been measured on scanning electron microscope (SEM) micrographs, as shown in Fig. 4.5 b). The bending radius increases with the oxidation temperature, as summarized in table 4.2 and in figure 4.6. It has to be noted that the thickness of the oxide layer grown at 1050 °C is 180 nm and not 200 nm like the others[10]. The bending radius for a 200 nm

---

[10]This lower thickness is due to an error done during the oxidation process, which was stopped too early .

thick layer, oxidized at the same temperature, should be about 20 μm higher (see Fig. 4.11 in section 4.3.3, where the bending radii between a 180 nm and a 200 nm SiO$_2$ film oxidized at 1000 °C differ for about 20 μm).

| oxidation temperature | bending radius [μm] | std. dev. [μm] | oxide thickness [nm] |
|:---:|:---:|:---:|:---:|
| 850 | 106 | 6.2 | 200 |
| 900 | 127 | 6.9 | 200 |
| 950 | 136 | 7.2 | 200 |
| 1000 | 163 | 3.5 | 200 |
| 1050 | 187 | 18.1 | 180[a] |

Table 4.2: Measured bending radii for various oxidation temperatures.
[a] The layer oxidized at 1050 °C was mistakenly grown to a thickness of 180 nm
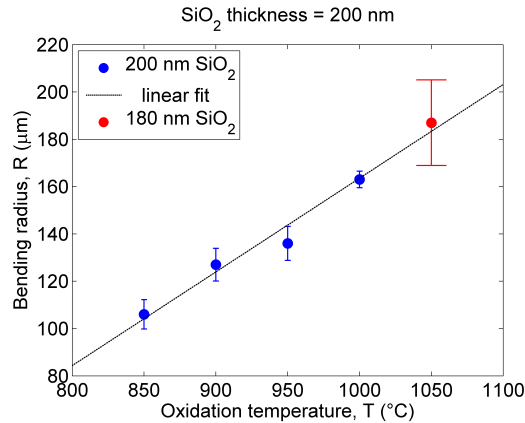


Figure 4.6: Bending radius dependence on the oxidation temperature. The last data point, marked in red, refers to a different SiO$_2$ thickness of 180 nm.

### 4.3.2 Double Clamped Structures for Stress Assessment

Guckel et al. [85] presented an interesting method to measure the average stress in thin films, making use of microfabricated test structures. They used double clamped beams made of the same material as the thin film, and analyzed their deformation as a reaction to the built-in stress. In particular, for films under compressive stress, the method relies on clamped cantilevers buckling. The basic idea is that the built-in stress present in the film will be able to buckle soft beams, but it will not be enough to bend stiffer double-clamped cantilevers. The test structures conceived by Guckel and coworkers consist of an array of double clamped cantilevers with varying length, i.e. with varying stiffness. For a given built-in strain $\varepsilon_{bi}$ the

shortest beams will remain straight, because they are tough enough to withstand buckling, while the longer ones will deform. The built-in strain level is assessed by observing the critical length $l_{cr}$ at which the beams change their state from unbuckled to buckled. Using the Euler buckling criterion for straight beams clamped at both ends, the average built-in strain of the film can be found from the following equation,

$$\langle \varepsilon_{bi}(z) \rangle = -(\pi^2/3)(t/l_{cr})^2 \,, \tag{4.10}$$

where $t$ is the thickness of film. The stress can be finally found via Hooke's law, linking the strain with the stress.

$$\langle \sigma_{bi}(z) \rangle = \langle \varepsilon_{bi}(z) \rangle E_{SiO_2} \tag{4.11}$$
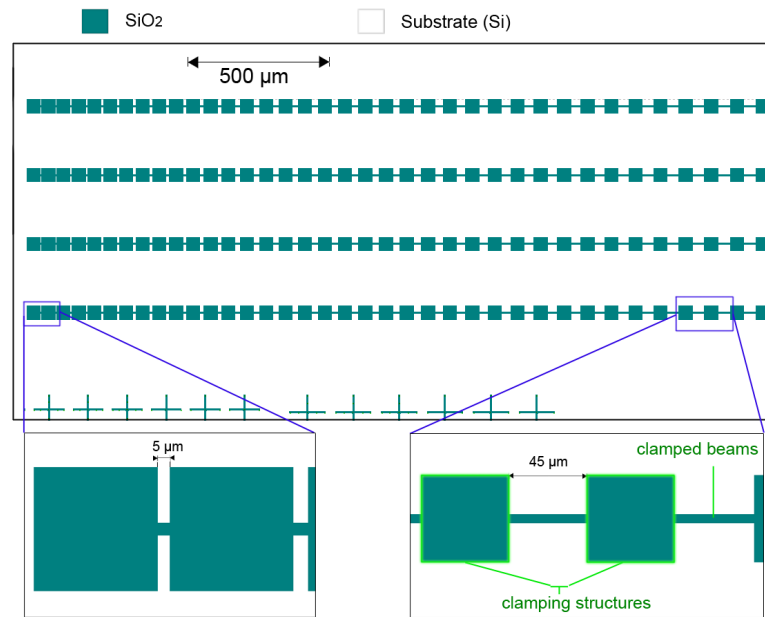


Figure 4.7: Layout of the double clamped beams array. The length of the double clamped beams decreases from right to left. The beams length is in the range from 5 to 45 µm.

We arranged Guckel's test structures on the photolithographic mask, in order to have them on the same wafers used for measuring the bending radii. We disposed double clamped beams
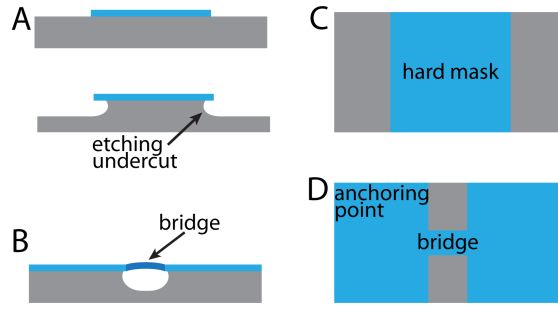
Figure 4.8: Schematics of the undercut due to anisotropic Si etching. A): when a hard mask (e.g. SiO$_2$ as in our case) is used during isotropic Si etching, a rounded undercut is shaped below the edge of the mask itself (side view). This generates a rounded undercut beneath the double clamped structure (bridge), as schetched in B) and as shown in Fig. 4.9.e and 4.9.f. C) and D) are the topviews of A) and B) respectively.

of different length as shown on Fig. 4.7. Their length varies from 5 to 45 µm. The objective is to define the critical length $l_{cr}$, as stated before. As shown in Fig. 4.9, we determined when buckling occurs by observing the different beams with a SEM.

The Young's modulus of SiO$_2$ grown with wet thermal oxidation has been measured to be about 57 GPa [55, 86]. From equation 4.10 and 4.11, the average stress can be assessed:

$$\langle \sigma(z) \rangle = -E_{SiO_2}(\pi^2/3)(h/l_{cr})^2 \tag{4.12}$$

Attention has to be payed to the quadratic dependence of $\langle \sigma(z) \rangle$ with respect to the critical buckling length, which make the stress measurements very sensitive to variations of $l_{CR}$. This is of extreme importance when considering the uncertainty on the average stress measurement. Figure 4.9 shows a panel of double clamped beams observed with SEM. Finding out the precise value of $l_{CR}$ is not trivial. Indeed, the buckling is obvious for images c) and d) but less for a) and b). Moreover, other sources of uncertainty are given by the discretization of the clamped beams length, and by the undercut due to etching (see Fig. 4.9 e and f), which causes the real length of the free-span of the beams to differ from the designed length. However, the technique allows for some constraint on the built-in stress to be found. Fig. 4.9 e) shows buckling for a beam of less than 6 µm in length, after having accounted for the undercut. A
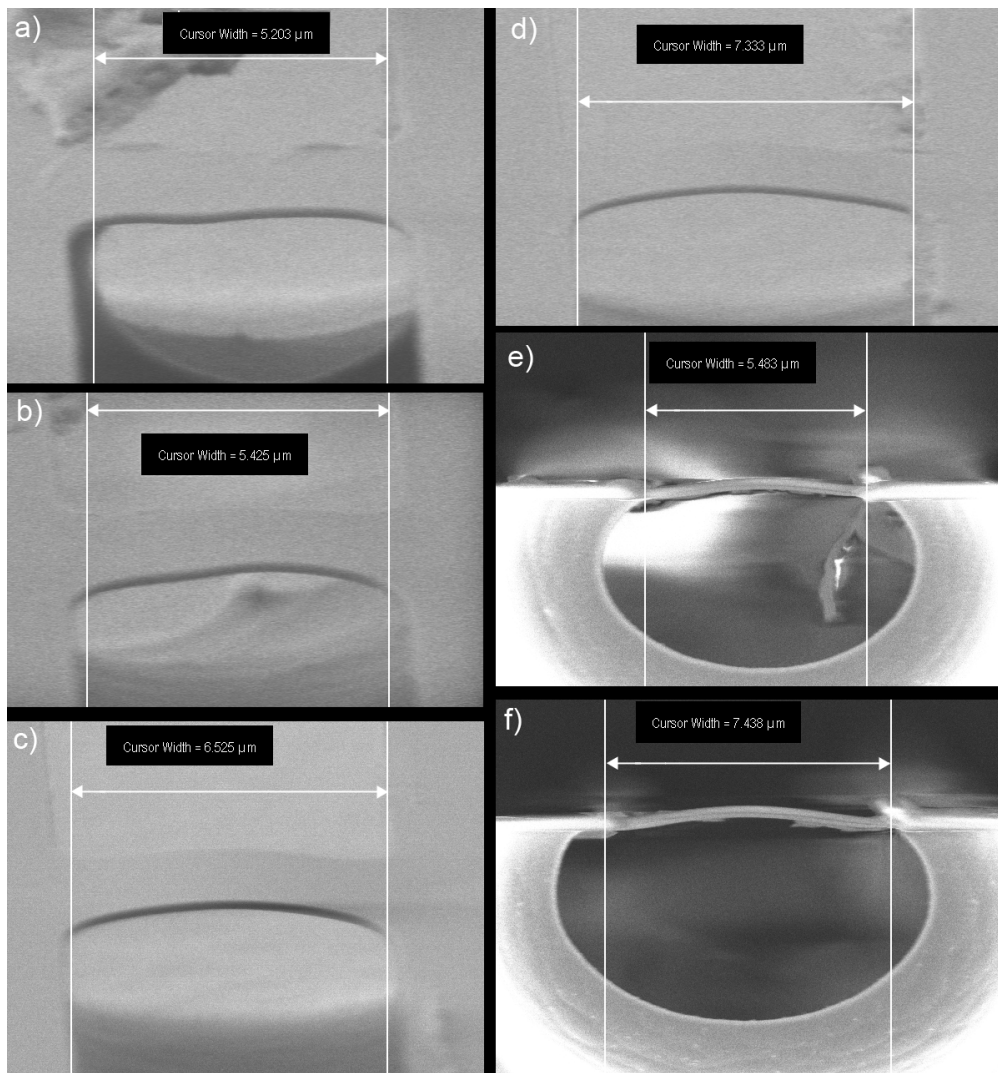
Figure 4.9: SEM micrographs of double clamped beams made out of SiO$_2$. The thickness is 200 nm and the oxidation temperature was 1000 °C. From a) to d) we can see slightly tilted views of the beams. e) and f) show cross sections of similar beams.

minimum average stress value can thus be conservatively calculated:

$$l_{cr} < \quad 6\,\mu m$$
$$\Rightarrow \langle \sigma(z) \rangle < \quad -206\,\text{MPa}\,. \tag{4.13}$$

As already mentioned, the built-in stress is a sum of thermal and intrinsic stress. The

thermal stress can be assumed to be homogeneous throughout all the thickness of the oxide, since the cooling process follows oxidation and concerns the whole SiO$_2$ film. As explained in equation 3.4 and in following comments, a stress which is constant through $z$ can be neglected in calculations related to released beams. However, it is playing an important role for beams that remain clamped to a substrate with a different thermal expansion coefficient, as it is the case here. The thermal stress can be expressed by the following equation:

$$\sigma_{th} = (\frac{E_f}{1 - \nu_f})(\alpha_f - \alpha_s)(T_1 - T_0) \tag{4.14}$$

Where $E_f$ and $\nu_f$ are respectively the Young's modulus and the Poisson ratio of the thin film. $\alpha_f$ and $\alpha_s$ are the thermal expansion coefficients of thin film and substrate respectively. $T_1$ and $T_0$ are, in our case, the oxidation temperature and room temperature. This stress is constant along the oxide layer and its value is around $-100\,\text{MPa}$.[11][87]. It follows, for the intrinsic average stress:

$$\langle \sigma_{int} \rangle = \langle \sigma_{bi} \rangle - \sigma_{th} < -106\,\text{MPa} \tag{4.15}$$

The values are negative in 4.13 and 4.15 because the stress is compressive. It is worth emphasizing that the average value of the intrinsic stress assessed here is only an approximated estimation, with the main uncertainty due to the assessment of the thermal stress $\sigma_{th}$.

### 4.3.3   Bending Radius vs. Oxide Thickness

In the previous section we have investigated the dependence of the bending radius $R$ on the oxidation temperature $T$. The goal was to vary the stress profile while keeping the mechanical properties constant (i.e. constant thickness), and check which bending radii are attainable experimentally. Since the achieved values are too big for the fabrication of a single-cell device, we explored the possibility to make them smaller with another strategy: thinning the SiO$_2$ film. This approach has two advantages. Firstly, it allows to gain insight into the stress profile

---

[11]This is a first order approximation, as $\alpha_f$ and $\alpha_s$ are functions of the temperature, so they are continuously varying during cooling. $\alpha_{SiO_2}$ is between $0.4 \times 10^{-6}$ to $0.7 \times 10^{-6}\,\text{K}^{-1}$, and $\alpha_{Si}$ is between $2.5 \times 10^{-6}$ to $4 \times 10^{-6}\,\text{K}^{-1}$.

$\sigma(z)$, and secondly, it makes possible the achievement of different values of $R$ by using the same wafers already prepared in the previous oxidation (with no need to prepare thinner oxide films from scratch), reducing significantly the costs of the research. The thinning method consisted in taking several chips from the same wafer, which we consider all having the same stress profile. Before releasing the structures from the Si substrate, we etched them from top in a buffered hydrofluoric acid (BHF) solution made by a 7:1 mix of NH$_4$F (concentration 40% in water) and HF (concentration 49% in water). Since the used etching method acts on the surface, we do not expect it to change the oxide stress profile. Each chip was etched for a different amount of time, in such a way to have various slices of the original oxide layer, each characterized by a fraction of the stress profile (see Fig. 4.10). The gradient $\nabla\sigma(z)$ is not
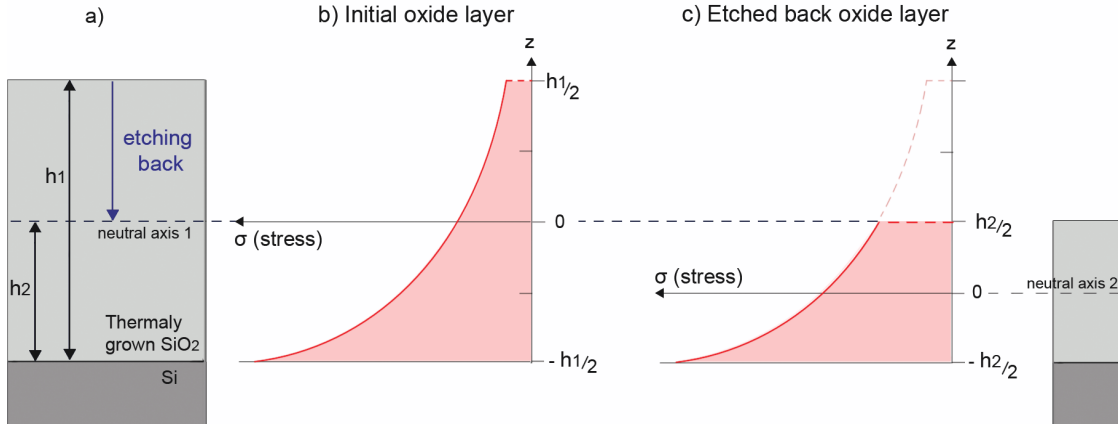


Figure 4.10: Schematics of the etch-back method. In **a)** a scheme of the SiO$_2$ layer on the Si substrate. Initially the thickness is $h_1$. After etching, an oxide layer of thickness $h_2$ remains. In panels **b)** and **c)** we have graphs of initial and post etching stress profiles, respectively. The origin of the z axis always matches the neutral axis in order to calculate properly the bending moment due to the stress.

expected to be constant (i.e. the stress profile is not linear with $z$), thus the bending radius should change by changing the thickness of the SiO$_2$ film. That a linear dependence of the stress on $z$ would give a constant radius when thinning the film, can be readily seen from equation 3.4 which we reproduce here below:

$$R = -\frac{Et^3}{12\int_{-t/2}^{t/2} z\sigma(z)\,\mathrm{d}z} \; . \tag{4.16}$$

Indeed, the integral at the denominator would be $\int_{-t/2}^{t/2} az^2\,\mathrm{d}z \propto t^3$, and would cancel out

| 850 °C wet oxide | | 1000 °C wet oxide | |
|---|---|---|---|
| Ox thick. [nm] | radius [μm] | Ox thick. [nm] | radius [μm] |
| 71 | $19 \pm 1$ | 66 | $20 \pm 1$ |
| 109 | $39 \pm 2$ | 105 | $64 \pm 10$ |
| 126 | $52 \pm 2$ | 125 | $72 \pm 2$ |
| 151 | $67 \pm 2$ | 151 | $110 \pm 6$ |
| 156 | $78 \pm 3$ | 158 | $124 \pm 4$ |
| 184 | $93 \pm 3$ | 200 | $163 \pm 4$ |
| 200 | $106 \pm 6$ | - | - |

Table 4.3: Different values of bending radii depending on the oxide thickness of the etched-back SiO$_2$ film. There are two series of measures, the first done on a wafer oxidized at 850 °C, and the second one on a wafer oxidized at 1000 °C.

with $t^3$ at the denominator, making $R(t) =$ constant. In case $\sigma(z)$ is not a linear function of $z$ – as it is the case for stress models of oxidized SiO$_2$ – then $t$ does not cancel out, and $R = R(t)$ is a function of the thickness $t$. In order to have a better insight into the stress profile of our SiO$_2$ films, we measured a set of bending radii $R_i^{meas} = R(t_i)$ for various thicknesses $t_i$. Then we assumed the stress profile $\sigma(z)$ to follow Fargeix's model (see section 4.1), and we fitted it to the measured $R_i^{meas}$. Let us have a more accurate look at how the fitting is performed. Indeed, the stress profile cannot be fitted directly to the measured data $(R_i^{meas}, t_i)$. We first have to derive the function $R_{\sigma(z)}(t)$ for a given stress profile $\sigma(z)$, then fit it to the data, by varying the stress profile, and eventually find the stress profile $\sigma_{best}(z)$ that produces the derived function $R(t)_{\sigma_{best}(z)}$ that is the best fit of the experimental data $(R_i^{meas}, t_i)$. The Fargeix's stress model of equation 4.5 can be rewritten in a condensed form as

$$\sigma_{int}(h, z) = \sigma_{max}(T)\, e^{-z/\lambda(z,h,T)}\,. \tag{4.17}$$

The exponential dumping length is not constant, but varies in every point $z$ along the SiO$_2$ thickness, and moreover it is a function of the oxidation temperature as well, via the coefficients $A(T)$ and $(B/A)(T)$, as detailed in equation 4.5. When the temperature $T$ is fixed, the expression of $\lambda(z, h, T)$ is known, and the only parameter to be determined is $\sigma_{max}(T)$, whose dependence on $T$ is not known. A least square method has been applied to find the best approximation of $\sigma_{max}(T)$ for a certain temperature, according to the following algorithm:

1. Fix the original oxide thickness $h$ after oxidation, and the temperature $T$ (5 values in the

range 850 to 1050 °C have been tested, once at a time).

2. After having fixed the temperature and the oxide thickness (200 nm in our case, as done experimentally), the function $\lambda_{h,T}(z) = \lambda(z, h_{fix}, T_{fix})$ is known and calculated using the model from Fargeix. The stress profile $\sigma_{h,T}(z) = \sigma_{max,T} \exp(-z/\lambda_{h,T}(z))$ depends thus only on the unknown value $\sigma_{max,T}$.

3. The theoretical bending radii $R_i^{theo}(t_i, \sigma_{h,T}(z), E)$ are calculated for each experimental thickness $t_i$ used in the etch-back experience, using equation 4.16. Assuming a constant Young's modulus $E = 60$ GPa, the bending radii depends only on $\sigma_{max,T}$:
$R_i^{theo} = R_i^{theo}(\sigma_{max,T})$.

4. The value of $\sigma_{max,T}$ is varied between 0 and 1000 MPa, in steps of 1 MPa, and the value $\sigma_{max,T}^{best}$ that best fit the theoretical radii $R_i^{theo}$ to the measured radii $R_i^{meas}$ is chosen. In this way the Fargeix's stress profile $\sigma_{h,T}(z) = \sigma_{max,T}^{best} e^{-z/\lambda_{h,T}(z)}$ that best predicts the experimental data $R_i$ vs. $t_i$ is found, for the chosen temperature $T$.

5. The process is then repeated from 1, by fixing another temperature.

The results of this fitting algorithm, executed with MATLAB®, are shown in Fig. 4.11. For data taken from a wafer oxidized at 850 °C (Fig. 4.11 top-left graph), the stress profile from Fargeix gives a poor fitting. Indeed the model curve for the same temperature simulates an almost constant bending radius for etched-back oxide layers. This is due to the almost linear stress profile (Fig. 4.11 top-right graph). To find a good agreement between data and model, we have to use the Fageix's stress profile expected at 1000 °C. The model, in this case, predicts a stress profile decaying more quickly over the distance $z$ from the Si-SiO$_2$ interface, due to a quicker stress-relaxation dynamics, as explained in section 4.1. Such a variable profile produces the expected trend of $R$ vs. $t$ in etching-back experiments, as can be observed from the good fitting between the data and the 1000 °C model (Fig. 4.11 top-left graph). This means that the wet oxidation performed at low temperature is giving a stress profile different from the one expected, and more similar to the ones presumed at higher temperature. Conversely, the data at high temperature (1000 °C) are in good agreement with the model of similar temperature (Fig. 4.11 low-left graph). A possible reason for the discrepancy observed at low temperature could lay in the approximation with which the relaxation time $\tau$ is known. Fargeix already
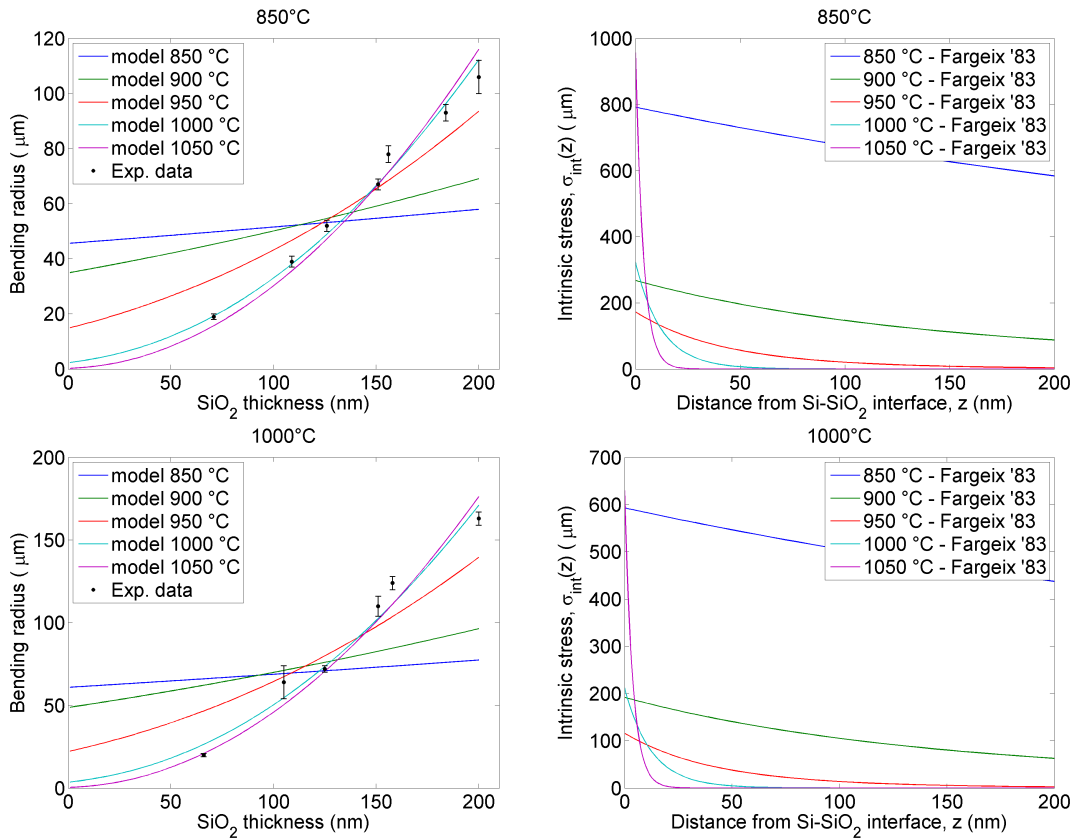
Figure 4.11: **Top left**: Experimental data ($R_i^{meas}, t_i$) from the etching-back experiment performed on a 200 nm thick SiO$_2$ layer oxidized at 850 °C. Five model functions $R_{\sigma(z)}(t)$ are also shown, each derived from a Fargeix's stress profile $\sigma(z)$ for a certain oxidation temperature (see legend). Each curve is, for its specific temperature, the one that better fits the data. It can be seen that Fargeix's model does not reproduce the experimental bending, since the model for 850 °C does not approximate well the data for the same temperature. Stress models for higher temperature fit better the experimental observations. **Top right**: Each of the curves is the Fargeix's stress profile that generates the corresponding model curve $R(t)$ of the graph on the left. For each temperature the shape of the profile is determined by the Fargeix's model, while its amplitude ($\sigma_{max,T}^{best}$) has been found as the one that produces the best fit to the data of the graph on the left. **Bottom**: Same as above, but with experimental data taken from an etching-back experiment done on a wafer oxidized at 1000 °C. Here the modeled behavior fits well the data for the same temperature. In both cases (top and bottom) the intrinsic-stress profile better approximating the real behavior (model 1000 °C) is concentrated approximately in the first 50 nm, and has a maximum value at the interface of 323 MPa (top) and 212 MPa (bottom).

showed that this parameter could vary from one kind of silica to another (e.g. from fused silica to thermally oxidized silica), and gave its value for the case of dry oxide [75]. It could thus be reasonable that $\tau$ is different in the case of wet oxides. A possible explanation could

come from the different molecular reactions happening in wet oxidation, where the oxidizing molecule is water instead of oxygen. The oxidation reaction happening at the Si-SiO$_2$ interface generates H$_2$ molecules:

$$2H_2O + Si = SiO2 + 2H_2, \tag{4.18}$$

which then diffuses back into the SiO$_2$ towards the SiO$_2$-gas interface. There are then two sources of hydrogen during a wet oxidation process, which are not present in dry ones: molecular H$_2$ liberated upon oxidation, and the one present in H$_2$O molecules. Breed [80] pointed out how this can lead to the presence of hydroxyl groups in the oxide:

$$0.5H_2O + 0.5Si - O - Si = SiOH$$
$$H_2 + Si - O - Si = SiOH + HSi. \tag{4.19}$$

These hydroxyl groups come at the expense of Si-O-Si bonds, and reduce the lattice density.[12] This is seen by a drastic increase in diffusivity of the oxidant species for wet oxidation as compared with dry (this increase is responsible for the much faster oxidation rate for wet processes). It could also be that the hydroxylation of Si-O-Si bonds reduces the viscosity of silica, making thus possible a faster stress relaxation at low temperature, resulting in a steeper stress profile, similarly to what was obtained by fitting the etch-back data for the 850 °C oxidation.

## 4.4 Conclusion to this Chapter

At the end of this chapter we can summarize the following points:

- The oxidation temperature affects the bending radius, but not in the way predicted by theory (Fargeix's model). Instead of having a minimum radius for a temperature in between 850 °C and 1050 °C, $R(T)$ increases monotonically with $T$. Quantitatively, the radii for 200 nm thick SiO$_2$ grown by wet oxidation are too big for the fabrication of single-cell μ-flowers, intended for the use with mouse fibroblasts.

---

[12] A similar phenomena is observed in PCVD SiN$_x$, where the Young's modulus of thin films has been observed to decrease strongly for an increasing presence of Si-H bonds [70].

- Test microstructures have been fabricated to assess the stress (double clamped cantilevers). A minimum boundary for the absolute value of the average stress can be conservatively evaluated: $|\langle\sigma_{int}(z)\rangle| > 100\,\text{MPa}$.

- In order to better understand the discrepancy between the expected and the measured trend of $R$ vs. $T$, the stress profile $\sigma(z)$ has been retrieved from data obtained through thinning of the SiO$_2$ film. The shape of the model has been assumed *a priori* to be the one described by Fargeix and Ghibaudo, since to my knowledge it is the most accurate model available for the stress in thermal oxide. The model is fully determined by two parameters, $T$ and $\sigma_{max}$, which have been varied in order to fit the data from the etch-back experiment. The results show that, even at low temperature (850 °C), the stress profile decreases very steeply away from the oxide-silicon interface, as it happens at high temperatures. This discrepancy between model and observed data might be ascribed to a lower viscosity, maybe originating from the hydroxylation and opening of some of the Si-O-Si bonds observed in wet oxides [80] . The stress profile functions, determined heuristically, can be practically used to predict the values of $R(t)$ for thicknesses $70\,\mu\text{m} < t < 200\,\mu\text{m}$ (see Fig. 4.11).

- The etch-back method was proven to be an effective way to reduce the bending radius by a factor of at least five. Radii as small as $20\,\mu\text{m}$ have been achieved, that place the technique in an interesting range of sizes, suitable for single-cell culture. Fig. 4.12 shows how SiO$_2$ films thinned to a thickness of about 70 to 100 nm allow to attain radii in the range from 20 to $40\,\mu\text{m}$. The corresponding theoretical spring constant $k$ for bent cantilevers with such thicknesses and radii spans the approximate range from 0.1 to $1\,\text{nN}\,\mu\text{m}^{-1}$. This is equivalent to an elastic continuous medium with a Young's modulus of about 0.1 to 1 kPa, as explained in section 3.5. Such a stiffness is comparable to the one of very soft tissues, e.g. neural ones [88].
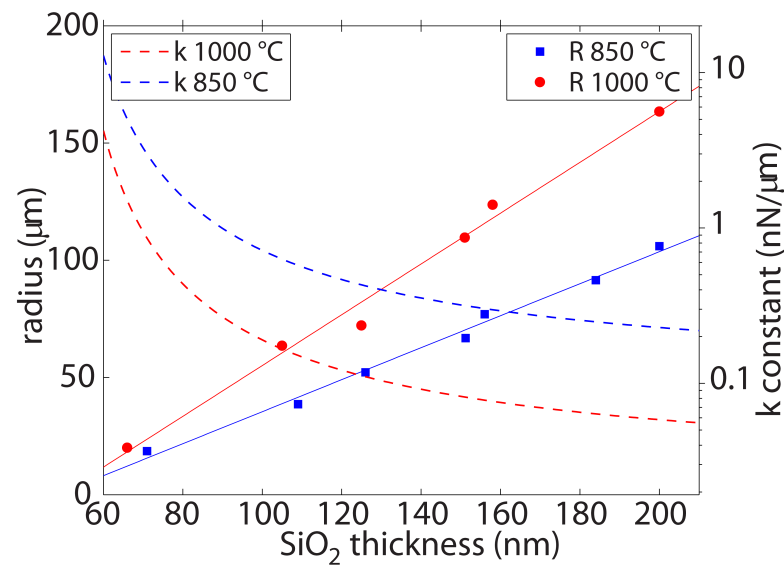
Figure 4.12: The graph shows the bending radius (left axis) and the theoretical spring constant (right axis) of bent cantilevers made out of $SiO_2$, oxidized either at $850\,°C$ or at $1000\,°C$. Thicknesses in the range from $\approx 70$ to $100\,nm$ give radii suitable for single-cell culture ($R \approx 30\,\mu m$ and very soft spring constants $k \approx 0.1\,nN\,\mu m^{-1}$.

# 5 Bent Cantilevers: 2nd generation (Ti-SiO$_2$ bilayer)

In the previous chapter, the first generation cantilevers that are made of single-layer SiO$_2$ and have a very small spring constant are described. These cantilevers having a stiffness resembling that of very soft tissues are applicable for the fabrication of three dimensional (3D) single-cell culture devices. On the other hand, it is our goal to fabricate stiffer spring constant cantilevers ($k \approx 10\,\mathrm{nN\,\mu m^{-1}}$) to mimic harder tissues and for cell traction forces (CTFs) measurements. Therefore, we explored bilayer cantilevers with materials designed to create opposite stress. In our design, the bottom layer is made out of SiO$_2$, featuring a compressive stress, while the Ti top layer acts to create a tensile stress. During the fabrication, upon release from the Si substrate, the SiO$_2$ bottom layer elongates and the Ti upper layer shortens resulting in an upward bending cantilever. More precisely, the bending moments generated by the two materials sums up to give a higher total moment. This higher moment, allows thicker cantilevers to bend with small radii. However, the use of an extra material brings additional costs due to the complexity of the new fabrication process, a more intricate and less predictable system, and the compatibility of another material that has to be taken into account in the functionalization protocol. In this chapter, we will discuss the details about the pros and cons of having a bilayer cantilever, its new fabrication process and the experimental results, which show a two orders of magnitude increase in the spring constant.

## 5.1 Advantages and Limitations of Adding a Second Layer

The advantage of using a bilayer is purely due to its mechanical properties. The use of two thin films bearing opposite intrinsic stresses (tensile vs compressive) produces a higher bending moment in the beam. This is clearly visible in Fig. 5.1). In a monolayer cantilever characterized
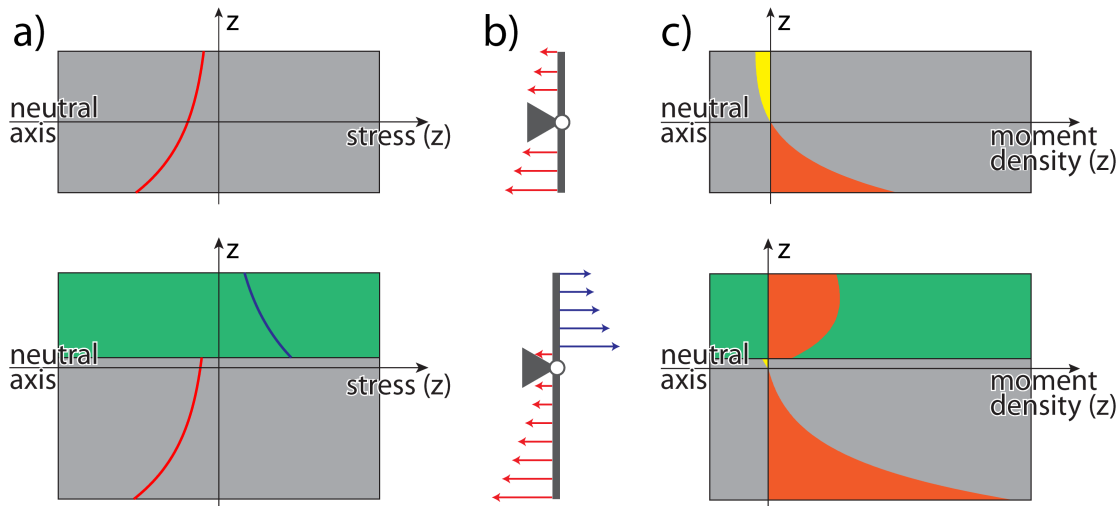


Figure 5.1: Schematics of stress and moments in a bilayer. **a)**: in a monolayer (top) with the stress in one direction only (either compressive or tensile), the stress below and above the neutral axis is pulling in the same direction, similarly to what would happen in a leverage (**b**) with the two arms loaded in the same direction. The total bending moment, given by the area subtended by the curve in **(c)**, is decreased, since there are two counteracting components (orange-positive and yellow-negative contributions). A similar sketch for a bilayer is depicted at the bottom. Here, the contributions of the two opposed stresses to the bending moment sum together, as pulling and pushing loads on the two arms of a leverage. This results in having a bigger bending moment.

by an intrinsic stress of one sign only (e.g. $\sigma(z) > 0$, as in Fig. 5.1.a, top) , the moment density $M(z) = z \times \sigma(z)$ is negative for $z < 0$ and positive for $z > 0$, and these two components partially cancel out each other in the total bending moment $M_{tot} = w \int_{-h/2}^{h/2} z\sigma(z)\,\mathrm{d}z$ (as shown by the orange and yellow areas in Fig. 5.1.c top). On the contrary, **in a bilayer system with opposite stresses**, the stress changes sign in the proximity of the neutral axis, so that **the moments generated by the two layers sum up giving a higher** $M_{tot}$, bending even thicker and stiffer beams to small radii, which would not be achievable with a monolayer of similar stiffness (Fig. 5.1.a-c, bottom). This phenomenon can easily be understood from the analogy between a stressed beam and a leverage. As drawn in Fig. 5.1.b, the neutral axis can be taken as the

fixed hinge of a leverage, and the stress as a load distributed along the arms. Thus, the first question arising when designing a bilayer system is: where is the best location to place the neutral axis (the hinge)? Said in another way, since the neutral axis position depends on $h_1$ and $h_2$ (equation 3.9): what are the optimal thicknesses $h_1$ and $h_2$? Intuitively, one might guess that the bending moment is maximized when the neutral axis is placed at the interface between the two layers (Ti-SiO$_2$ in our case). This would be the case for constant stress (load) distributions, but unfortunately the answer is not that straightforward for more involved stress (load) profiles. Indeed, the precise value of $M_{tot}$ depends on the specific shape and magnitude of the two stress profiles, as it can be predicted from the complex shape of the function $M(z) = z \times \sigma(z)$. It might be that $M_{tot}$ increases by shifting the neutral axis from the interface. Indeed, a shift of the neutral axis from the interface increases the lever arm on which one of the two stresses is acting, and reduces the lever arm for the other. E.g., it might be better to reduce the lever arm of the smaller stress and increase it for the bigger one. To summarize: **the precise knowledge of the intrinsic stress profiles is required for the optimization of the thickness ratio** $h_1/h_2$**, and consequently of the bending moment** $M_{tot}$. Thus, we see the first cons of having a second layer. Due to the material choice, i.e. titanium, **there is no known model**, to the best of our knowledge, **to predict the stress profile precisely**, and it is impossible to define the best parameters $h_1$ and $h_2$ prior to fabrication. This is the reason why we adopted an **empirical approach to study the bilayer system**, as it will be explained in the next section. But before that, let us continue to review the pros and cons.

The second prominent advantage of the proposed bilayer approach comes from the exploitation of the total stress on SiO$_2$ layer. When we analyzed the equilibrium conditions of a stress-bent cantilever, we have seen in equations 3.4 that only the gradient of the stress profile contributes to the bending. The total built-in stress of thermally grown SiO$_2$ is given by:

$$\sigma_{\text{bi}}(z) = \sigma_{\text{thermal}} + \sigma_{\text{intrinsic}}(z) \,, \tag{5.1}$$

where the thermal stress, due to the thermal expansion mismatch between Si and SiO$_2$, is constant through $z$ (Fig. 5.2.b). Thus, it contributes to an overall straight elongation of the

beam after its release from the substrate, but not to the bending. Only $\sigma_{\text{intrinsic}}(z)$ provides a gradient useful for the bending, when a monolayer SiO$_2$ beam is considered. This is no more the case for a bilayer. Indeed, when Ti is deposited on top of SiO$_2$, the latter is still pinned to the Si substrate, with all of its built-in stress still present, including the constant thermal part. After release from the substrate, **the thermal contribution will now participate to the bending**, since it is not a constant stress throughout all the bilayer, but it is present only in SiO$_2$. Using the leverage analogy, the constant $\sigma_{\text{thermal}}$ is no more applied to both arms, and does not cancel out on its own as it was happening in a monolayer. Instead, it loads only one arm, contributing in this way to the bending moment. A second question then arises: what kind of wet oxide is it better to use? One oxidized at low temperature, with higher intrinsic stress and lower thermal, or one fabricated at high temperature, with higher thermal but lower intrinsic stress? The thermal stress of a material can be estimated as:

$$\sigma_{\text{thermal}} = (\alpha_{\text{SiO}_2} - \alpha_{\text{Si}})\Delta T\, E_{\text{SiO}_2}\,. \tag{5.2}$$

Watanabe et al. measured the values of the thermal expansion coefficient of Si in a wide range of temperatures [87], and found it to be between 2.6 and $4.3 \times 10^{-6}\,°\text{C}^{-1}$, while SiO$_2$ has a lower coefficient $\alpha_{\text{SiO}_2} = 0.5 \times 10^{-6}\,°\text{C}^{-1}$. Using these values, the thermal stress of the oxide film after cooling at room temperature has been calculated as 120 MPa and 160 MPa, for oxidations performed at 850 °C and 1000 °C, respectively. Fig. 5.2 shows how the presence of the thermal stress makes the oxidation temperature almost equivalent in terms of momentum generated in a bilayer. Indeed, while the 850 °C oxide has a higher stress at the interface of the Si substrate, the 1000 °C oxide has a higher stress away from the Si interface. Looking at the momentum density $M(z) = z \times \sigma_{\text{bi}}(z)$ (right panel), we can observe that the areas under the two curves, i.e. the total bending moments, are very close to each other. The difference in the total moment is slight: only 6% more has been calculated for the 1000 °C oxide. However, for the fabrication of monolayer cantilevers, the 850 °C oxide proved to be better, since small radii can be attained with thicker films[1] (Fig. 4.12). Thus, **silicon oxide grown with a wet thermal process at 850 °C was used in the remainder of this work**, unless specified otherwise.

---

[1]We observed that for very thin SiO$_2$ layers, below $\approx 60\,to\,70$ nm, the fabrication process is no longer stable, resulting in beams being not only curved upwards, but also twisted randomly, and/or sticking with each other.
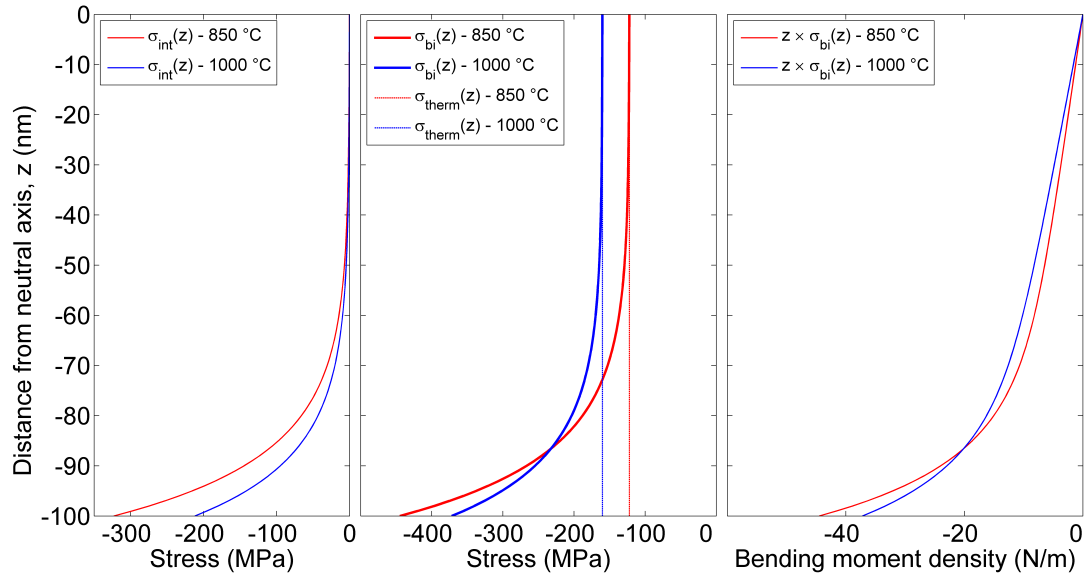
Figure 5.2: $SiO_2$ stress profile models for 850 °C and 1000 °C. **Left**: the curves are the Fargeix's models for the intrinsic stress retrieved by fitting the data from the etch-back experience (see Fig. 4.11). The intrinsic stress is higher for lower temperature oxide. **Middle**: in a bilayer, also the thermal stress contributes to the bending moment. The total built-in stress for low temperature is higher for $z$ values far from the neutral axis, but gets smaller close to it. **Right**: bending moment density of the total built-in stress ($z \times \sigma_{bi}(z)$). As an example, the case with the neutral axis at a distance of 100 nm from the Si-$SiO_2$ interface is considered. The total bending moments (areas subtended by each curve) differ by only 6% from each other, and are basically equivalent for practical purposes.

Similarly to what was done for $SiO_2$, also for the top layer we had to take into account the constraints of biocompatibility and the ones posed by the functionalization/passivation protocol. **Titanium was finally selected as a material for the top layer, due to the following reasons**:

- Ti thin films deposited by physical vapor deposition (PVD) at room temperature are characterized by a tensile internal stress [89];

- Ti is biocompatible [68];

- Ti oxidizes in air, showing an external shell of native $TiO_2$ few nanometers thick [90], which is fundamental during μ-flowers functionalization/passivation, since it can be coated with the anti-fouling molecule poly(L-lysine)-*grafted*-poly(ethylene glycol) (PLL-*g*-PEG) [91], creating a chemical contrast with functionalized Au, (see section 6.2).

Even if it enables the bending of stiffer cantilevers to small radii, the use of Ti has a couple of drawbacks. First, the complexity of the fabrication process is increased. New steps of deposition and etching are added and the release and cleaning of bent cantilevers become more delicate and critical, as will be explained in the next section. Second, the stress of evaporated metallic films is not described by any quantitative model, and it is often difficult to control and predict, as pointed out by Ohring in his book *Materials science of thin films* [92]:

> Despite the apparent simplicity of the experimental techniques and corresponding defining stress equations, the measured values of the intrinsic contribution to $\sigma_{\text{film}}$ display bewildering variations as a function of deposition variables, nature of film-substrate combination, and film thickness. [...] measured stress values for [...] evaporated films should be considered as representative rather than precise. [...] data published by different investigators employing similar and different measurement techniques are frequently inconsistent [...].

Keeping this in mind, a **combinatorial empirical approach** has been used to find the best match between Ti and SiO$_2$ thicknesses. **Four layers of SiO$_2$ with** thicknesses of about 100, 125, 150 and 180 nm were used as the base layers of the cantilever, **combined with four layer of Ti** with thicknesses of 30, 60, 110 and 150 nm. In order to have consistent results, the Ti layer of a given thickness was deposited on top of all the four SiO$_2$ substrates during the same deposition. Fabrication details are given in the following section, after which the characterization of the µ-flowers obtained with the bilayer beams will be presented, in terms of their bending radii $R$ and spring constants $k$.

## 5.2  Fabrication of Ti-SiO$_2$ Bilayer Bent Cantilevers

In the present section the details of the fabrication process are fully given, including the materials, machines and methods used.

*SiO$_2$ growth and thinning (Fig.5.3A and 5.3B)* — The fabrication of Ti-SiO$_2$ bilayer cantilevers started with a wet oxidation of Si (100) wafers. The growth was carried out at a relatively low temperature (850 °C) and no post-oxidation annealing was done,[2] to avoid stress relax-
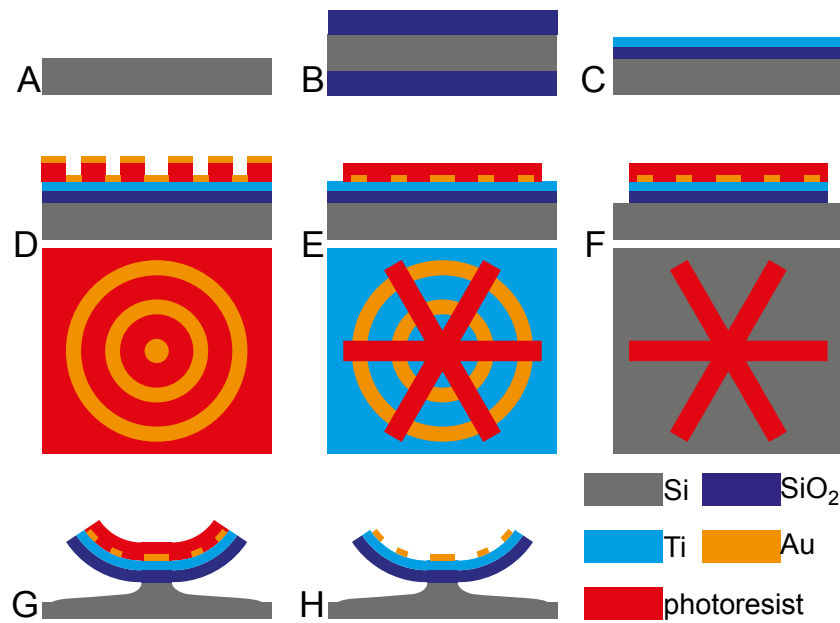
Figure 5.3: Schematic process flow for the fabrication of bilayer Ti-SiO$_2$ μ-flowers. (A) Test grade Si wafers (100) are used as substrate on which (B) 200 nm thick SiO$_2$ is thermally grown. (C) Silicon oxide is removed from the backside with BHF etching; the SiO$_2$ on the front side is first thinned down to a lower thickness (with a second BHF etching) and later is coated with a Ti film by PVD. (D) shows the cross section and the top view of a lift-off process in which photoresist is used as a mask to deposit ring-shaped patterns of Au. (E) After removal, another photoresist layer is applied, with the shape of μ-flowers. In (F) Au, Ti and SiO$_2$ are etched away from all of the area not protected by photoresist. An isotropic Si dry etching (G) is performed to release the cantilevers from the substrate, and the intrinsic stress of the Ti/SiO$_2$ bilayer make cantilevers bending out of plane. (H) Eventually the protective photoresist is removed.

ation in SiO$_2$. The final thickness of SiO$_2$ was 200 nm. After oxidation, the topside of the wafers was protected by 2 μm of spin coated photoresist AZ$^{®}$ 1512 HS (MicroChemicals GmbH, Ulm, DE) and the oxide on the back side of the wafer was completely removed in a BHF solution made of a 7:1 mix of NH$_4$F (concentration 40% in water) and HF (concentration 49% in water). Later, the photoresist was removed using SVC 14 remover (Micro Resist Technology GmbH, Berlin, DE), followed by rinsing with deionized water (DI water). The SiO$_2$ films remaining on the front side were thinned to various thicknesses by etching in BHF, and their thicknesses were measured by a spectroscopic reflectometer (Nanospec 6100, Nanometric Inc., Milpitas, CA) in 49 points distributed across the surface of each wafer. The standard deviations of the

---

[2]Particularly, on purpose the wafers were not kept at high temperature. The temperature was brought down to the unloading temperature of 700 °C by a ramp down rate of 4 °C/min. The wafer cooling was executed in N$_2$ to avoid further oxidation.

oxide thickness across a single wafer were between 1.1 and 1.8 nm.

*Ti deposition (Fig. 5.3C)* — A layer of Ti was subsequently evaporated on top of SiO$_2$ in a LAB 600 H e-beam evaporator (Leybold Optics GmbH, Alzenau, DE). A small area of the wafer was masked during the evaporation, to keep it free from Ti and use it as a baseline for the measurement of Ti thickness. The measurement was performed with an Alpha-Step 500 mechanical profilometer (Tencor, Milpitas, CA), and bear an uncertainty of $\pm 2$ nm.

*Au patterning via lift-off (Fig. 5.3D)* — Au patterns were fabricated and functionalized with a lift-off process. First the wafer was dehydrated on a hot plate at 150 °C for 3 min 30 s. Then the wafers were lifted to a distance of 5 mm over the hotplate for 30 s, to gently decrease the wafer temperature. This information is given in details because the thermal story of a metallic thin film could affect its stress [89], and might be relevant for reproducibility. A sacrificial layer of LOR resist (MicroChem Corp., Newton, MA) was spun onto the wafer for 30 s at a speed of 6500 rpm, followed by baking on a hotplate at 190 °C for 4 min 10 s, with a proximity gap of 375 μm. The nominal LOR thickness was 400 nm. Photoresist AZ$^®$ 1512 HS was spun onto LOR at a speed of 2800 rpm for 1 min 30 s, to reach a nominal thickness of 1.6 μm. All the steps just detailed (dehydration, spin coating, baking) were performed with an EVG$^®$ 150 automated resist processing system (EVG, Sankt Florian am Inn, AT). The resists were exposed with ultra violet (UV) light on an MJB4 mask aligner (Süss MicroTec AG, Garching, DE), using an I-line filter and a dose of 42 mJ/cm$^2$. A chrome mask that was previously written on a DWL 200 laser lithography system (Heidelberg Instruments Mikrotechnik GmbH, Heidelberg, DE) was used during wafer exposure, to transfer circular rings into the resist (Fig. 5.3D). After exposure the wafer was manually developed in a beaker containing 100 ml of MF-CD 26 developer (Micro Resist Technology GmbH, Berlin, DE). The beaker was gently rotated and shaken to refresh the exhausted developer at the photoresist surface. Development was stopped after 1 min 30 s by dipping the wafer in DI water, and followed by a thorough rinse with DI water and drying with a nitrogen gun. The wafer was thus protected by a photoresist layer, except for concentric ring patterns that were exposed and removed during developing stage. The diameter of the central circle was about 8 μm, while the thickness of the external rings was about 5 μm. A Ti/Au (5/40 nm) layer was deposited onto the wafer with a LAB 600 H e-beam evaporator, with Ti acting as an adhesion layer for Au. The sacrificial photoresist was removed

by overnight immersion in Microposit 1165 remover (Shipley Co., Inc., Malborough, MA), followed by rinsing in isopropyl alcohol, rinsing in DI water and spin drying. In this way Au rings were fabricated on top of the Ti-SiO$_2$ bilayer. Their thickness was measured as 44(2)nm with an Alpha-Step 500 mechanical profilometer.

*Second photolithographic mask (Fig. 5.3 E)* — A new photoresist layer was patterned to shape the cantilevers of μ-flowers. Again, a film of AZ$^®$ 1512 HS was spin coated at a speed of 3000 rpm for 1 min 30 s, to achieve a thickness of 1.5 μm. A chrome mask containing the patterns to define the cantilevers was aligned on the wafer, to center the μ-flowers with respect to the Au rings (Fig. 5.3 E). The alignment was done manually with optical microscopes on an MJB4 mask aligner, with a typical alignment error of about 1 μm. The photoresist was then exposed to UV light, using an I-line filter and a dose of 42 mJ/cm$^2$. After exposure the wafer was manually developed and rinsed as described before. The wafer was selectively protected by photoresist with the shape of μ-flowers. Four different geometries of μ-flowers were fabricated, by changing the number of cantilevers (3, 4, 6, and 8 cantilevers per μ-flower, as shown in Fig. 5.4). Each of these geometries was then reproduced by varying the length of
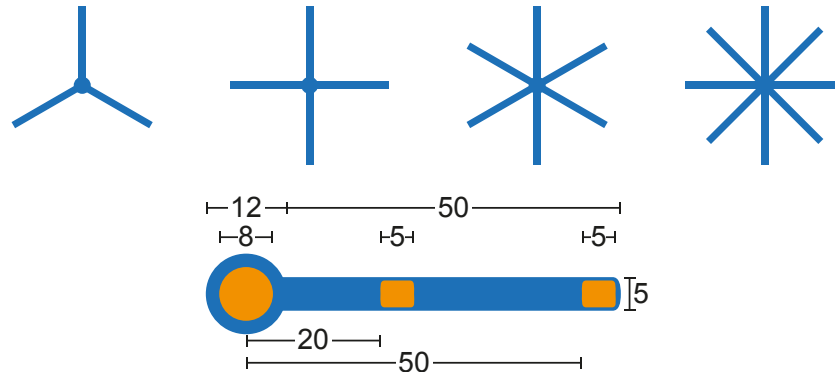


Figure 5.4: Schematics of μ-flowers geometry. Four kinds of μ-flowers were fabricated, with a varying number of cantilevers (3, 4, 6 and 8 respectively). Each of these four kinds was further reproduced in four different dimensions, with various cantilever lengths (20, 30, 40 and 50 μm). The dimensions of the 50 μm long cantilever are shown, together with the dimensions of Au spots. For shorter cantilevers the length of the cantilever itself and the spacing between Au spots are scaled proportionally, while all of the other dimensions are kept constant.

the cantilevers to 4 different values (20, 30, 40, and 50 μm). In this way every chip (dimension 1 cm × 1.2 cm) contained 16 versions of μ-flowers, and each of these versions was replicated 600 times, for a total of about 10 000 μ-flowers per chip. μ-flowers dimensions are shown

in Fig. 5.4.  The pitch between subsequent μ-flowers was 60, 80, 100, and 120 μm, scaling according to the length of cantilevers.

*Cantilever shaping by etching (Fig. 5.3 F)* — The part of Au rings exceeding the photoresist was etched in a water solution containing KI (25 g/l) and I$_2$ (12 g/l) for 30 s, followed by rinsing in DI water.  In this way Au spots were left only on the cantilevers.  This process enables the perfect alignment of the Au spots with respect to the long axis of the cantilevers, independent of the alignment error between the 2$^{nd}$ mask and the Au rings, as sketched in Fig 5.5.  This
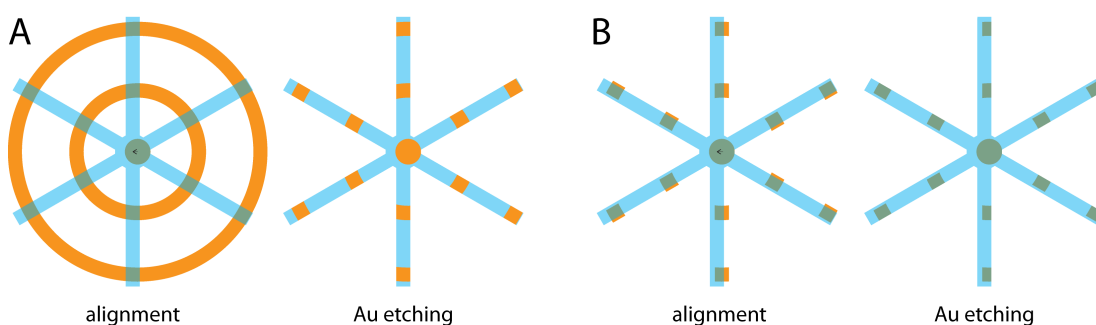


Figure 5.5: Alignment of Au spots.  When aligning the second mask (μ-flowers) over the first (Au rings), a misalignment of about 1 μm at best is normally present.  **A**: using Au rings results in having Au spots always aligned over the width of cantilevers, after the excessive Au is etched. **B**: if Au spots were deposited, instead of rings, the alignment error would result in having a significantly different area of Au on the cantilevers.

error affected only the position of Au spots along the cantilever length, but since this error (≈ 1 μm) is much shorter than the length of cantilevers, it is absolutely tolerable.  This explains why Au rings were deposited, instead of depositing directly Au spots.  In the latter case, a misalignment between Au spots and cantilevers would have resulted in discrepancy in the Au spots size distribution (see Fig. 5.5).  The non-protected area of Ti was etched as well, this time by means of an inductively coupled plasma (ICP) generated in a mix of Cl$_2$ and BCl$_3$ gases.  For this etching an STS ICP etching system was used (Surface Technology Systems, Newport, UK). The wafer was then diced into 1 cm × 1.2 cm chips.

*Cantilever release and cleaning (Fig. 5.3G and 5.3H)* – Chips were rinsed in DI water, and glued with QuickStick$^{TM}$ 135 (Electron Microscopy Sciences, Hatfield, PA) on a blank dummy Si (100) wafer, in order to continue the process with machines compatible with 10 cm wafers. Dummy and real chips were loaded in an Alcatel 601E deep reactive ion etcher (Alcatel, Paris,

FR) and SiO$_2$ was etched from the unprotected areas of the chips using a plasma from C$_2$F$_6$ gas (ICP coil power: 1800 W, power of substrate bias: 400 W). In this way the bilayered Ti-SiO$_2$ cantilevers were patterned on the Si substrate (Fig. 5.3F).
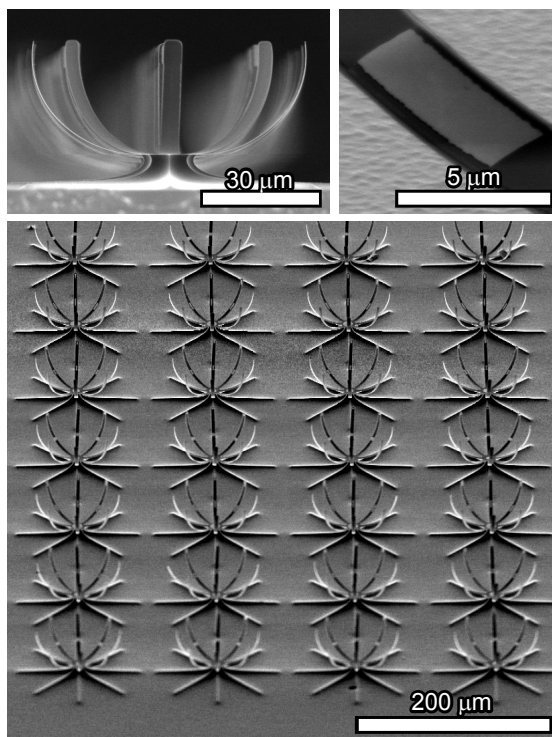


Figure 5.6: SEM micrographs of µ-flowers. **Top-left**: side view of an 8 arm µ-flower. **Top-right**: close up view of an Au rectangular spot onto a bent cantilever. **Bottom**: an array of µ-flowers.

## 5.3   Characterization of Ti-SiO$_2$ Bilayer Bent Cantilevers

Cantilevers were then released from the substrate by an isotropic Si etching performed by plasma generated from SF$_6$ gas. To avoid excessive heating of cantilevers, a low power was used during Si etching (ICP coil power: 800 W, power of substrate bias: 0 W). Chips were detached from the dummy wafer by melting QuickStick$^{TM}$ 135 on a hotplate at 135 °C. This process was done as quickly as possible, to avoid thermal stress relaxation of the Ti film, and lasted less than 1 min. Residues of glue were carefully removed from the back of the chips with acetone, using a swab to prevent any wetting of the topside (which would be harmful for released cantilevers, due to capillary forces). Finally, the photoresist was stripped from cantilevers by means of oxygen plasma, in a TePla 300 reactor (PVA TePla AG, Kirchheim, DE).

The stripping process was segmented in three short steps of 10 s each, to minimize cantilever heating. For the same reason the power of the machine was kept low (100 W, 200 ml/min oxygen flux).

### 5.3.1 Bending Radii (R) and Theoretical Spring Constants (k)

In this section the characterization of the geometrical and mechanical properties of the Ti-SiO$_2$ bent cantilever is presented. Concerning geometry, we measured the bending radii for all 16 thickness combinations. Each of the four Ti layers has been deposited in one single PVD process on all of the wafers with different SiO$_2$ films, in order to minimize the variability of Ti deposition from sample to sample. The oxide layers have been grown in one single wet oxidation process at 850 °C, to a thickness of 200 nm, and have been subsequently thinned in BHF. The maximum uncertainty on the thickness was 4 nm for the thinnest layers of 100 nm (which underwent the longest BHF etching), decreasing to 1 nm for the thickest 182 nm films (which underwent the shortest BHF etching). The radius $R$ for each combination was measured by taking scanning electron microscope (SEM) micrographs of the side view of µ-flowers. In order to decrease any possible variability in the comparison of various samples, only µ-flowers with 8 cantilevers each have been imaged for the characterization of $R$. Fig. 5.7 shows a typical
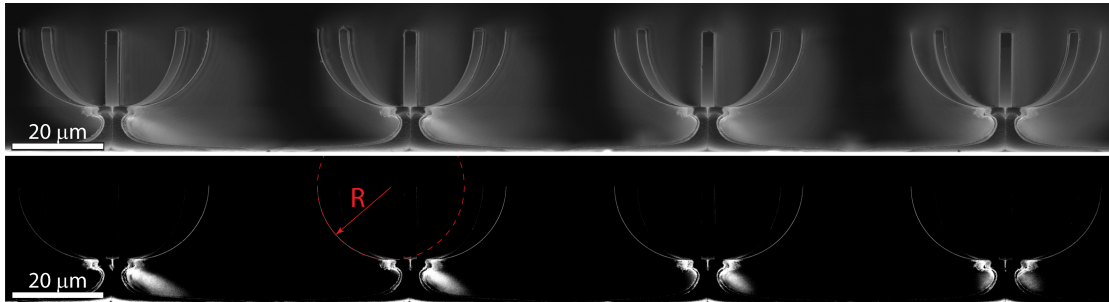


Figure 5.7: **Top**: SEM cross views of µ-flowers, used to measure the bending radius. **Bottom**: contrast enhancement and image binarization are used in order to extract the coordinate of the cantilever profile. The radius is found by fitting these data with a circumference .

SEM side view with four µ-flowers. By increasing the contrast of the picture and applying a proper threshold the external cantilevers are highlighted (Fig. 5.7, bottom). To select the pixels truly belonging to the cantilevers, a region of interest was manually defined, which cut out all the other pixels above the threshold but not corresponding with the beam. The $(x, y)$

coordinates of the selected pixels were recorded and fitted with a circle using a least square method. At least eight cantilevers were fitted for each sample, and their average radius was assigned to the corresponding Ti-SiO$_2$ combination. The fit with a circular shape is very good and the standard deviation of the average radii is often less than 0.5 μm. However, it has to be considered that for each sample the measured cantilevers were all close to each other. A bigger deviation could be reasonably expected across the wafer, where film thicknesses and etch rates vary more. For this reason, scale bars in Fig. 5.8b and 5.8c are set to a more conservative value of 1 μm. As expected, the addition of the Ti layer allowed for small radii, even if the stiffness of
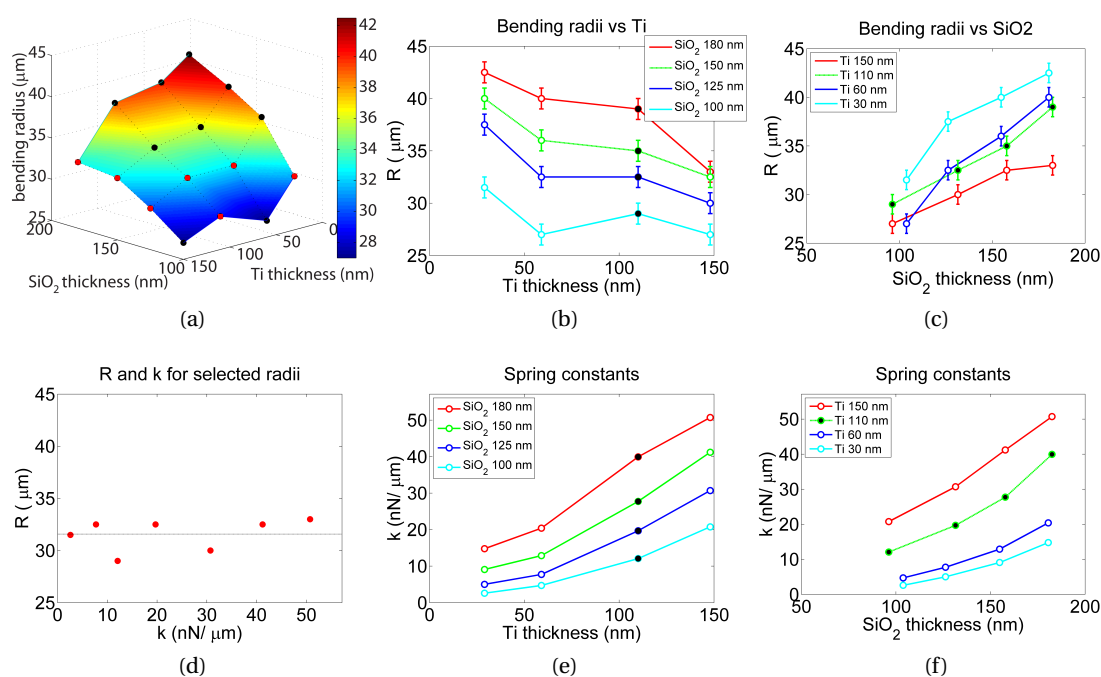


Figure 5.8: **Top**: left to right: bending radius as a function of Ti and SiO$_2$ thickness for the sixteen combination analyzed; radius as a function of Ti thickness only, and radius as a function of SiO$_2$ thickness only. The points marked in black are from a faulty deposition, and should be discarded when considering the trend of the curves. **Bottom**: left: measured radii and theoretical spring constants for seven selected samples suitable for single-cell culture. The values of $k$ are calculated for the real case of a constant lenght $l = 50$ μm for all the samples. Center and right: spring constant vs. Ti and SiO$_2$ thickness, respectively. For these two graphs the spring constants are calculated assuming a variable lenght $l$ for each sample, and a constant angle $\vartheta = \pi/2$ (same shape but different size for each kind of μ-flower, for a better comparison).

the beams was greatly increased. Seven combinations out of sixteen have a suitable radius for the fabrication of single-cell devices, as shown in Fig. 5.8a by the red markers. Fig. 5.8b

and 5.8c shows the same $R$ data plotted in two dimensions, versus the thickness of Ti and SiO$_2$, respectively. The data highlighted by a black marker have to be regarded with caution when making any consideration on this graph, since they correspond to a faulty Ti deposition of the 110 nm thick layer. Indeed, a bug in the program controlling the e-beam evaporator stopped the deposition midway. It was possible to resume it and achieve the final thickness, but Schneeweiss et al. showed that the stress behavior is affected by having the film deposited in two tranches [89].

The trend expected by increasing the thickness of the Ti layer in Fig. 5.8b would be (i) an initial shrinking of $R$, due to the additional bending moment provided by the bilayer configuration, and (ii) a final increase of $R$ when the increasing stiffness is no more compensated by an increasing moment.[3]Somewhere in between, a minimum is expected. For the lower curve of Fig. 5.8b, we can see that the radius does not get smaller when the thickness of Ti is increased from 60 to 150 nm (the value at 110 nm is not considered for the aforementioned reasons). The minimum attainable $R$ probably lays in between these two thicknesses, and further increasing Ti would probably give larger radii. Oppositely, for the thickest oxide layers the trend still looks decreasing. The bilayer is probably not yet exploited at its maximum and a thicker Ti layer could result in even smaller radii, and stiffer cantilevers.

Fig. 5.8d shows $R$ and $k$ for the selected combinations with $R \approx R_{\text{target}} \approx 30\,\mu$m. Their radii are spanning the relatively small range from 29 to 32.5 $\mu$m, with an average value of 31.6 $\mu$m. On the other hand, the spring constants $k$ of these selected Ti-SiO$_2$ combinations span a much wider range from 1.8 to 35 nN $\mu$m$^{-1}$. Compared with the stiffness of 1 nN $\mu$m$^{-1}$ achieved with oxide monolayers, this is a significant 35 fold increase. Moreover, this increased range of stiffness contains seven points (intermediate values are accessible), revealing the power of the combinatorial approach as a means to decouple $k$ from $R$. In other terms, the combination of variable thicknesses of Ti and SiO$_2$proved to be an effective way to decouple the geometrical and the mechanical properties of $\mu$-flowers, since the radius can be kept almost constant while the spring constant varies significantly. Interestingly, the stiffness values achieved with this method cover a variety of physiological values [77], including the one of soft nervous tissue,

---

[3]Indeed, making Ti thicker and thicker will increase the stiffness (proportional to $t^3$), but will not increase the bending moment that much, for two reasons: (i) the stress is usually confined close to the substrate, and vanishes away from it, (ii) the neutral axis will shift far from the Ti-SiO$_2$interface, close to where it should stay to have the tensile and compressive stresses on the two sides of the leverage fulcrum.
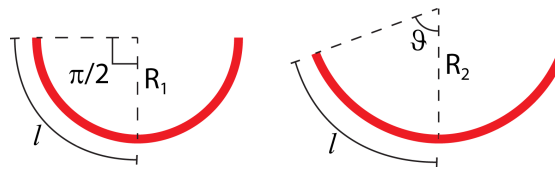
Figure 5.9: Comparison of different μ-flowers. Since the length $l$ is the same for each sample, but the bending radii are different, the shape of μ-flowers is not the same for all the samples. For a better comparison of the spring constants of different cantilevers, we calculated their values assuming a constant angle $\vartheta = \pi/2$ for all of them, and a variable length $l$, tailored to the radius in order to have cantilevers covering a quarter of circumference ($l_i = (\pi/2)R_i$).

fat, muscles, cartilage and precalcified bone.

The spring constants for the complete set of Ti-SiO$_2$ are plotted in Fig. 5.8e and 5.8f, versus Ti and SiO$_2$ thickness, respectively. For the selected beams with radius $R \approx 30\,\mu$m (Fig. 5.8d), the spring constant was calculated for the fabricated cantilevers, i.e. for cantilevers with a length $l = 50\,\mu$m. In this case, the angle subtended by the bent beams is close to a right angle, $\vartheta = (l/R)(180°/\pi) \approx 95°$, and the beams are approximately a quarter of circumference. For the other combinations, characterized by larger $R$, the beams of length $l$ do not cover a quarter of circumference any longer, as shown in Fig. 5.9.The comparison of the spring constants would thus be biased by the fact that each beam subtends a different angle $\vartheta$, which is a parameter that greatly affects the spring constant (equation 3.8). It is more significant to compare μ-flowers with the same shape, achievable by adjusting the length $l$ to the given radius. Following this idea, the spring constants plotted in Fig. 5.8e and 5.8f are the ones calculated considering $\vartheta = \pi/2$ for each cantilever (i.e. cantilevers with a length $l = (\pi/2)R$ adjusted to the length). These cantilevers were not fabricated, since the maximum length used in the fabrication was $50\,\mu$m, but they can be produced by modifying their lengths on the photolithographic masks.

**Measurement of the Stiffest Spring Constant**

A direct measurement of the spring constant of the stiffest cantilevers has been done (Ti = 148 nm, SiO$_2$ = 182 nm, $R = 33\,\mu$m). This test was performed during a demonstration day of the company FemtoTools[4]. Unfortunately, the sensor was available only for a demonstration,

---

[4]http://www.femtotools.com

so no systematic measurements were taken, but only a couple of force-displacement curves. Despite this, the results are worth being reported, since they are the only direct measurement of the spring constant taken so far. We used a force sensor FT-S100 Microforce Sensor Probe, based on a capacitive force sensor, with 5 nN force sensitivity. The tool is very convenient for mechanical tests on microstructures, due to its versatility of displacement along three axis. The standard probe used is made out of a Si beam, with the section pulling on the sample being 50 µm × 50 µm. A sketch of the probing experiment is shown in Fig. 5.10a. The stiffer cantilevers have been used, in order to better match the sensitivity of the sensor.
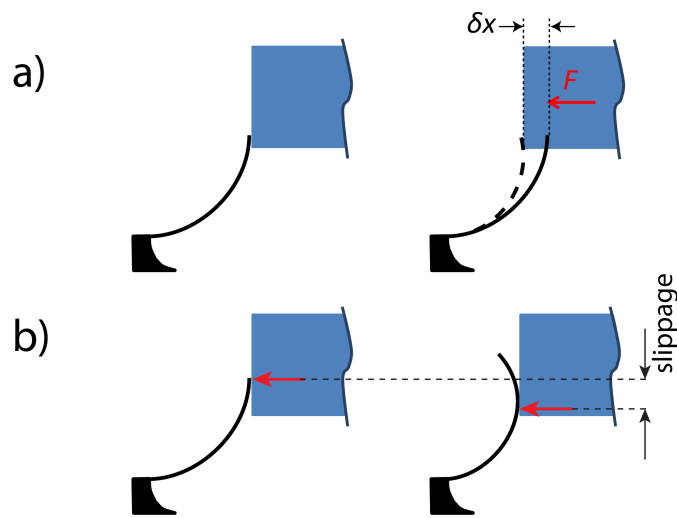


Figure 5.10: Schematics showing the measurement of the spring constant with a force sensing probe. **a)**: the sensor measures both the displacements and the force. **b)**: during compression it might happen that the bent cantilever slips over the force sensor probe, causing a displacement of the contact point (red arrows) and of the perceived spring constant.

Discontinuities in the force curves have been observed, and we hypothesize that they are due to slippage of the cantilevers over the probe face, during loading. As schematized in Fig. 5.10b, the beam might have slipped upwards during compression, resulting in a shift of the contact point with the probe (red arrows). This behavior might explain the sudden jumps observed in the force curves, followed by an increase in the steepness of the curve itself, as if the cantilever was loaded in a lower point along its length, showing an higher spring constant (Fig. 5.11). For this reason, only the first linear segments of the load curves are taken into account (red points in Fig. 5.11). The first measurement gave a value of the spring constant of 126 nN µm$^{-1}$, more than twice the theoretical expectation of 50 nN µm$^{-1}$. However, the data are quite scattered,
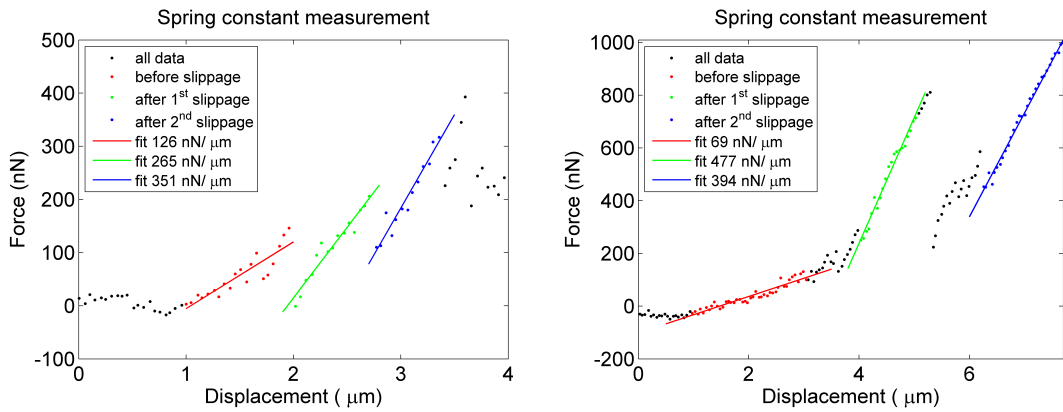
Figure 5.11: Direct measurement of the spring constant of the stiffest cantilevers (Ti-SiO$_2$: 148-182 nm). Discontinuities in and steepening of the force curves might be due to slippage of the cantilevers with respect to the force probe.

and a discontinuity in the force curve happened after a compression of only 1 μm. The data of the second curve look less scattered, and a more stable linear segment of about 3 μm gave a value of $k = 69$ nN μm$^{-1}$, in better agreement with the calculation. More data are without any doubt necessary for a statistically meaningful calibration, and the data quality can be improved by using the sensor on an isolated bench, not available during the test, but normally necessary for fine measures. For these reasons, we preferred to use the theoretical values for the force quantification done in the next chapter 6. This test, despite its preliminary nature, gives however an indication that the theoretically calculated spring constant should be in reasonable agreement with the real value.

## 5.4 Conclusion to this Chapter

The following points can be concluded from this chapter:

- The use of Ti-SiO$_2$ bilayer beams increased significantly the bending moment originating from the built-in stresses, with respect to SiO$_2$ monolayers. However, the increased complexity of the system and the lack of a reliable model for the stress in deposited metallic films, made it necessary to adopt a combinatorial empirical approach, in which sixteen different combinations of Ti-SiO$_2$ bilayers have been tested.

- Seven combinations gave values of $R$ in the range 29 to 32.5 μm, suitable for single-cell

culture. At the same time, the span of the spring constants for these seven combinations extends from $\sim 2$ to $50 \, \text{nN} \, \mu\text{m}^{-1}$, resulting in a 50 times increase of the maximum stiffness previously reached with SiO$_2$ monolayers. Moreover, since seven values of $k$ are available for an almost constant $R$, the geometrical and mechanical properties of the µ-flower devices are decoupled. Single-cell substrates with the same 3D geometry, but with highly variable rigidity, are fabricated.

• The attained stiffnesses match the values of a wide range of physiological rigidity, from soft nervous tissue to cartilage and precalcified bone [77], making the device suitable for the *in vitro* mimicking of the natural microenvironment.

# 6 Cell Traction Forces Measurement of Fibroblasts

## 6.1 Introduction

For the experiments reported in this section, we used μ-flowers with 50 μm-long cantilevers having a bending radius of 28 μm. μ-flowers with a different number of cantilevers have been used (3, 4, 6 and 8 cantilevers). Two parameters are necessary in order to quantify cell traction forces (CTFs) by means of cantilevers: the position where the force is applied to, and the spring constant experienced by the force in that point. For this reason, we developed a strategy aiming to localize the focal adhesions (FAs) of cells, i.e. the protein complexes anchoring cells to the substrate, and through which cells exert forces. The strategy relies on the creation of cell-adhesive patterns surrounded by an area passivated against cell adhesion. This objective is practically achieved by creating a chemical contrast on the surface of the cantilevers, by depositing Au spots that are selectively functionalized prior to cell culture. Ideally, the cell-adhesive Au spots are placed at the end of the cantilever, in order to have the cells well suspended in three dimensions. However, if the adhesive points are too far from each other, the fibroblasts are not able to reach them out . For this reason a second Au spot was fabricated on every cantilever, as already described. To avoid any confusion, we remind here the nomenclature used to distinguish the two Au spots deposited onto each cantilever: we will call *distal* Au spot the one placed at the free-end of the cantilever, while we will refer to the one located in the middle of the cantilever as *proximal* Au spot.

## 6.2    Localization of Cell Adhesions via Surface Functionalization

The topside of bilayer cantilevers is made out of Ti, which oxidizes in air giving rise to a native $TiO_2$ layer of a few nanometers; in a similar way the Si surface of the chip spontaneously oxidizes in air, giving rise to a native $SiO_2$ layer, while the underside of cantilevers was directly fabricated from an $SiO_2$ film. It follows that all of the surfaces present on the chip – except for the Au spots – are either $TiO_2$ or $SiO_2$, which are both negatively charged at physiological pH, allowing poly(L-lysine)-*grafted*-poly(ethylene glycol) (PLL-*g*-PEG) to be adsorbed on them [91]. In this way both Ti and $SiO_2$ could be passivated at the same time against cell adhesion. Conversely, Au spots were functionalized with a peptide in order to enhance the formation of focal adhesions. The functionalization protocol started by cleaning the chips with an ultra violet (UV)-ozone PR-100 photoreactor (UVP, Upland, CA) for 30 min. Right afterwards the chips were placed inside tailor made poly(dimethylsiloxane) (PDMS) wells, specifically fabricated for surface functionalization and cell culture purposes (PDMS: Sylgard 184 at 1:10 w/w; Dow Corning, Midland, MI).These wells are rectangular and fit chip dimensions. They were used to keep a constant layer of liquid of about 1 mm above released cantilevers, to prevent them from collapsing under capillary forces that could occur due to handling errors, such as air to liquid and vice-versa phase changes. Special care was also taken while pipetting, in order not to damage the three dimensional (3D) structures with excessive liquid flow. As previously done [14], Au spots on cantilevers were functionalized by flooding the entire chip overnight with 200 µl of a 3 mg ml$^{-1}$ solution of the peptide Ac-Gly-Cys-Gly-Arg-Gly-Asp-Ser-Pro-Gly-NH2 (PolyPeptide Laboratories, Strasbourg, France) in phosphate buffered saline (PBS) (Gibco, Life Technologies, Carlsbad, CA). The peptide is adsorbed on Au surface via the thiol side chain of the cysteine amino acid. Samples were then rinsed in PBS and passivated by flooding the
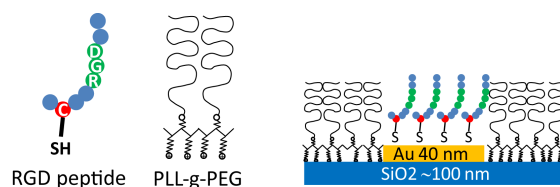


Figure 6.1: Schematics of the functionalization strategy. A peptide is used to functionalize the Au spots, by exploiting the SH group of a cysteine for selective self-assembly on Au surface, and the RGD sequence as a ligand for integrin. The comb polymer PLL-*g*-PEG is instead used to passivate $SiO_2$.

chips for 2 h with 200 µl of a PBS solution with 0.2 mg ml$^{-1}$ PLL-*g*-PEG (20)-[3.5]-(2) (SuSoS AG, Dübendorf, CH). PLL-*g*-PEG labeled either with Rhodamine or with Atto-633 was used on some samples in order to better visualize the cantilevers. Finally the chips were thoroughly washed with PBS and serum free Dulbecco's Modified Eagle's Medium (DMEM) (Gibco, Life technologies, Carlsbad, CA) prior to cell plating.

In order to check for the effectiveness of the functionalization protocol, µ-flowers not yet released from the Si substrate have been used (i.e. flat, two dimensional (2D) µ-flowers). Indeed, they are much more easily and better visualized with a widefield microscope with respect to 3D microflowers, which require the use of a confocal microscope. As shown in Fig. 6.2, Au spots not occupied by cell processes appear darker than the rest of the cantilevers, suggesting that they are functionalized with the RGD-peptide, while the remainder of the cantilevers is passivated with fluorescent Rhodamine-PLL-*g*-PEG. Focal adhesions of fibroblasts adhering to individual µ-flowers were stained as well, using Rhodamine-labelled anti-vinculin. They are easily recognizable since their signal is definitely brighter than the one of PLL-*g*-PEG adsorbed onto the cantilevers. Fig. 6.2C highlights how force-sustaining focal adhesions of adherent cells are well confined to the functionalized Au spots.
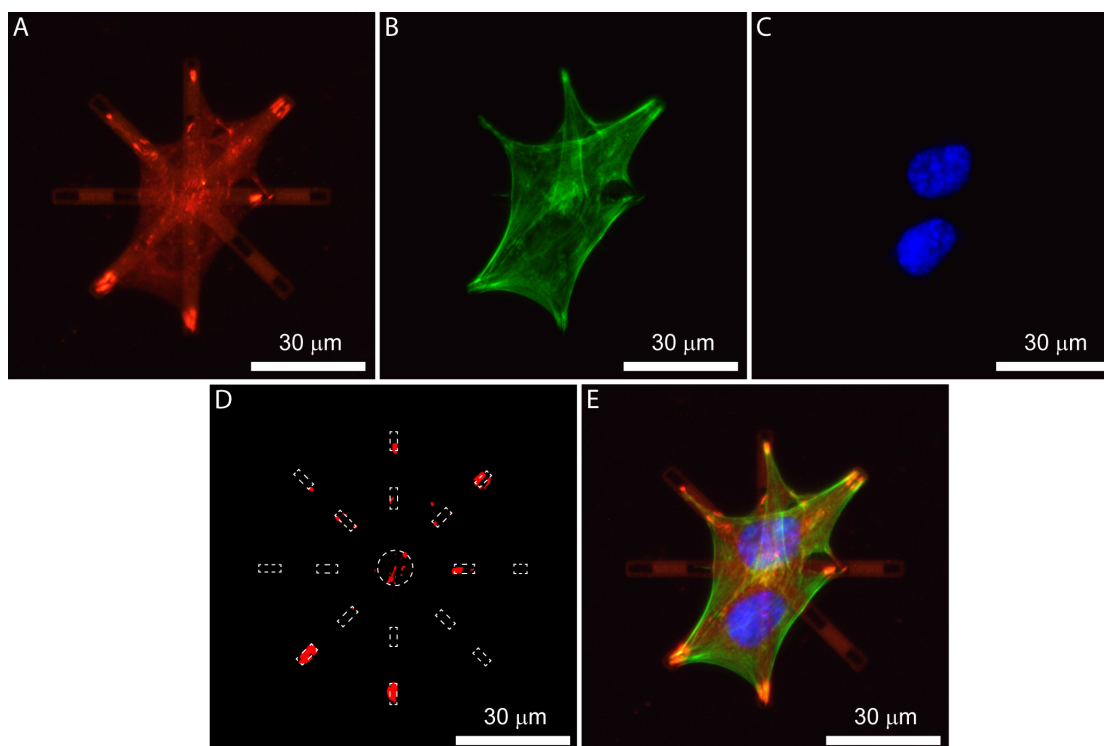
Figure 6.2: Epifluorescence micrographs of two MEFs adhering on a μ-flower. Cantilevers were not released from the substrate, in order to facilitate imaging. **A**: Red channel showing both the Rhodamine-labelled PLL-*g*-PEG and immunostained vinculin. Au spots at the end and in the middle of cantilevers were functionalized with the RGD peptide, reason why they don't adsorb PLL-*g*-PEG and look dark. **B**: Green channel showing F-actin stained with phalloidin. **C**: Blue channel showing the nuclei (DAPI). **D**: shows in red these pixels that have an intensity higher than the 80% of the maximum intensity: they are due to vinculin present in focal adhesions. Notice the localization of vinculin on Au spots (manually outlined with white dashed lines). **E**: merged image of the three channels.

## 6.3   Cell Culture and Time Lapse Imaging

A clonal MEFs cell line [14] was used for all the experiments. Cells were maintained at 37 °C in a humidified environment with 6% $CO_2$ in DMEM supplemented with 10% fetal calf serum (FCS) and 1% antibiotic-antimycotic solution (all from Life Technologies, Carlsbad, CA). At 80% confluency cells were harvested with 0.05% trypsin-EDTA (Gibco, Life technologies, Carlsbad, CA) and re-suspended in DMEM containing 10% fibronectin-depleted FCS to prevent unwanted cell adhesion. About 32000 cells in 4 ml medium were seeded onto a chip and cultured overnight. About 40–50% of the μ-flowers were filled with cells, as shown in Fig. 6.3. For live imaging purpose, cells in culture were treated with CellMask™ Orange plasma membrane
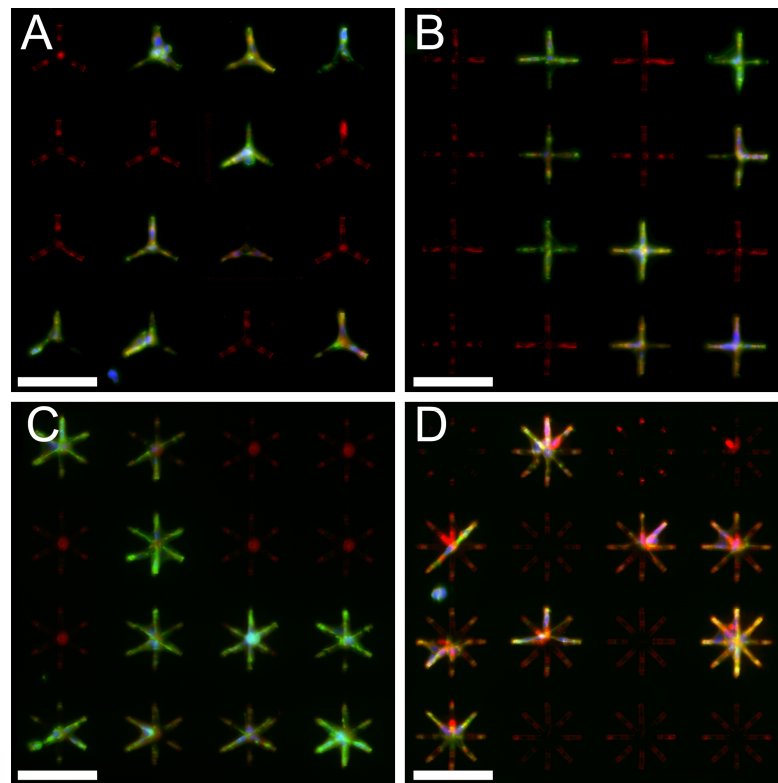
Figure 6.3: Epifluorescence micrographs showing arrays of µ-flowers. **A**, **B**, **C** and **D** show µ-flowers with 3, 4, 6 and 8 cantilevers respectively. About 40-50% of the µ-flowers contain MEFs, after seeding and leaving them spread overnight. Passivation of the chip background prevented MEFs from adhering on it, and confined them inside µ-flowers. Red: PLL-*g*-PEG labeled with Rhodamine; green: Alexa Fluor® 488 phalloidin; blue: DAPI. Scale bars are all 100 µm long.

dye (Invitrogen, Life technologies, Carlsbad, CA) for 30 min. Before transferring the chip onto the microscope stage, the medium containing the dye was replaced with phenol red-free and bicarbonate-free L-15 medium (Gibco, Life technologies, Carlsbad, CA) containing 10% FCS. During cell culture and imaging the chip was fixed onto a Petri dish by means of a tailor-made PDMS case (the same used for functionalization). Time lapse imaging was performed to quantify the cantilevers displacements generated by cells inside µ-flowers. An upright fluorescence LSM710 microscope with a 20× water immersion objective and equipped with an incubation chamber was used (Carl Zeiss Microscopy GmbH, Jena, Germany). The temperature inside the chamber was kept at 37 °C. Four fields of view with cells attached to µ-flowers were chosen and imaged with a CCD camera to mark the initial positions of cantilevers as a reference. Each field of view contained 12 µ-flowers of one particular geometry (with 3, 4, 6, or 8 cantilevers, re-

spectively; all the imaged cantilevers were 50 µm long). A total of 20 µ-flowers contained cells, either single ones or few of them (typically two or three). Lysophosphatidic acid (LPA) (Sigma-Aldrich, St. Louis, MI) was added on stage to a concentration of 5 M to induce cell contraction [48], and cells were imaged every 2 min. For each time point and for each field of view a volume of 447 µm × 335 µm × 62 µm was acquired with a voxel dimension of 0.32 µm × 0.32 µm × 2 µm (x, y and z respectively). The use of a widefield microscope allowed the imaging time to be kept below 8 s for each acquired volume, in order to reduce phototoxicity. Cells were fixed after 1 h of imaging with 4% paraformaldehyde for 5 min and stored in PBS at 4 °C. In some cases cells were fixed after overnight culture in DMEM containing 10% fibronectin-depleted FCS [14], without LPA stimulation, and processed for immunofluorescence using labeled phalloidin to stain F-actin, anti-vinculin (mouse monoclonal antibody hVIN-1) to detect FAs, and DAPI to label nuclei (all reagents from Sigma-Aldrich, Buchs, Switzerland).

## 6.4 Image Processing and Cantilever Tracking

The 3D stacks were deconvolved with Huygens® software (Scientific Volume Imaging, Hilversum, NL), in order to reduce the noise coming from light sources localized out of the focal plane. Pictures were then processed with a Sobel operator in order to enhance the edges of cells and cantilevers, using ImageJ software [93]. The free-ends of cantilevers were manually tracked using the Manual Track plugin for ImageJ.
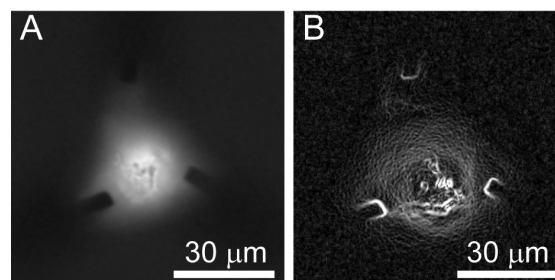


Figure 6.4: Image processing. **A**: original widefield epifluorescence micrograph with the extremities of the cantilevers in focus. **B**: same of **A** after applying the Sobel operator to enhance the edges.
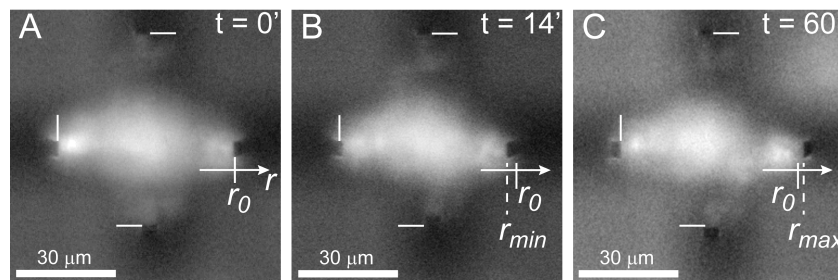
Figure 6.5: Live imaging top views of a fibroblast inside a µ-flower with 4 cantilevers, illustrating how the displacements of the cantilevers are measured (fluorescence micrograph with the free-ends of cantilevers in focus). For live imaging, fibroblasts membranes were stained with CellMask™ Orange plasma membrane dye. At time $t = 0$ min (LPA injection) the initial position $r_0$ of each cantilever is marked (solid lines in panel A-C) and set equal to 0. The tips of cantilevers are tracked at subsequent times $t$ (dashed lines in B and C) and their radial displacement $r(t)$ is measured with respect to $r_0$. The position $r(t)$ is defined to be positive when the tip distance from the center of the µ-flower is larger than at $t = 0$ min. **B**: at $t = 14$ min the cantilever on the right reaches its minimum value for $r(t)$, named $r_{\min}$ ($< 0$). **C**: at $t = 60$ min min the tip of the cantilever has moved outwards and reached the maximum value $r_{\max}$ beyond $r_0$ ($> 0$).

## 6.5 Cell Traction Forces Calculation

MEFs were cultured overnight onto the chips, allowing them to adhere and spread inside µ-flowers. For live imaging, cell membranes were stained with CellMask™ Orange plasma membrane dye, and LPA was added to the culture medium in such a way to induce fibroblasts contraction during image acquisition. The free-ends of cantilevers were manually tracked in order to measure their displacement and calculate CTFs acting on them. For each cantilever the position $r_0$ of the tip at time $t = 0$ (time of LPA injection) was taken as a reference and set equal to 0 (solid lines in Fig. 6.5A-C). For subsequent times t we measured the radial displacement of the tip $r(t)$ with respect to the initial position $r_0$ (Fig. 6.5B and C). The tangential part of the displacement was omitted, since it was small compared to the radial one (typically less than 5%). $r(t)$ is defined to be negative when the tip is closer to the center of the µ-flower with respect to its initial position $r_0$ (cell contraction) and is positive when the tip lays farther away from the center with respect to $r_0$ (cell relaxation and cantilever opening beyond the initial position $r_0$ at the time of LPA injection).

The cantilevers were split into two sets for statistical analysis. One set with cells adhering to the distal Au spot, and another one with cells adhering to the proximal Au spot – or with
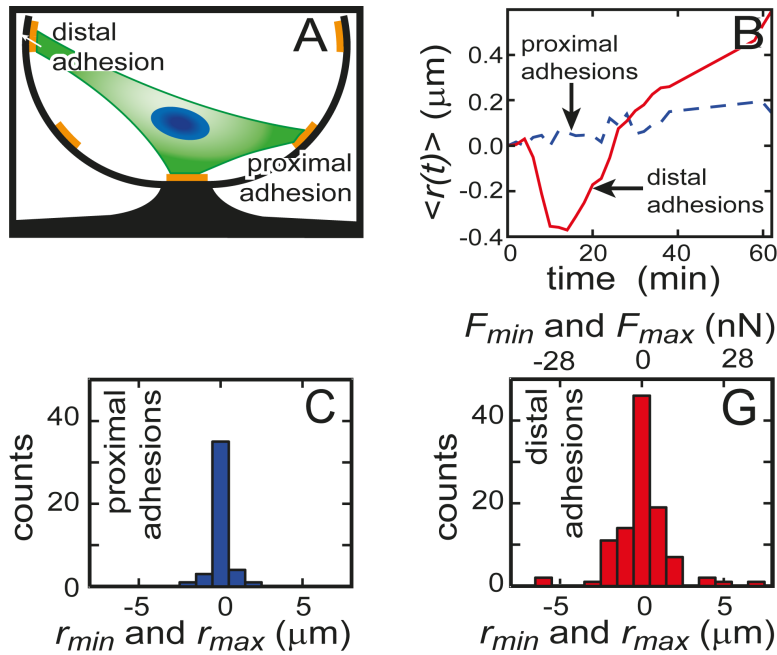
Figure 6.6: **A**: scheme of a cell growing inside a μ-flower, showing distal and proximal adhesions on Au spots. For data analysis, the cantilevers were sorted in two families, according to the position of cell adhesions along their length (see text for more details). Panel **B** shows the average displacement $< r(t) >$ of cantilever tips for the two families of cantilevers. **C** and **D**: distributions of $r_{min}$ and $r_{max}$ for the two families. Cells pulling at proximal adhesion spots (**C**) perceive a stiffer spring constant ($k_D = 313\,\mathrm{nN\,\mu m^{-1}}$), and do not move significantly the cantilevers (the width of the distribution is comparable to the experimental error, see text). Cells pulling at distal adhesion spots (**D**) face a much softer spring constant ($k_P = 5.5\,\mathrm{nN\,\mu m^{-1}}$), and are able to move the cantilevers significantly, allowing cell traction forces to be measured.

no cell adhesions at all (Fig. 6.6A). Cell processes pulling on the distal spot of cantilevers experience a spring constant $k_D$ of about $5.5\,\mathrm{nN\,\mu m^{-1}}$, and are expected to displace the cantilevers free-end from its initial position $r_0$ by few micrometers, since typical CTFs have been measured to be in the order of few tens of nanonewtons [10]. On the contrary, when forces are applied to the proximal Au spot, the experienced spring constant $k_P$ is much higher and equals about $313\,\mathrm{nN\,\mu m^{-1}}$. Hence, cantilevers with cells adhering at the proximal spot are expected to bend the cantilevers only by a fraction of a micrometer. The typical cantilever dynamics observed upon stimulation with LPA is characterized by an initial movement of the cantilever edge towards the center ($r(t) < 0$) for about 15 min, after which $r(t)$ reaches a minimum value $r_{min}$ (Fig. 6.5B). Then, while contraction of cell bodies continues, the tension exerted on the cantilevers begins to relax, due to cell processes becoming thinner

and weaker, and sometimes due to adhesion detachment. Cantilevers begin to move back from the center of μ-flowers, and eventually they cross the initial position $r_0$, with $r(t)$ taking positive values (see Fig. 6.5C). In order to quantify the amplitude of cantilever displacements, we recorded the minimum ($r_{\min}$) and maximum ($r_{\max}$) values of $r(t)$ for each cantilever over an interval of 60 min, and plotted their distributions for the two families of cantilevers, i.e. cantilevers with distal and proximal adhesions respectively (Fig. 6.6C and D). When cellular forces act on the proximal part of cantilevers, $r_{\min}$ and $r_{\max}$ are sharply distributed around zero (Fig. 6.6C), with an average value of 0.08 μm and a standard deviation of 0.4 μm. The standard deviation is similar to the pixel dimension (0.32 μm) of the acquired images, hence it can be mainly ascribed to the error introduced by manual tracking. It follows that there are no significant forces measurable when a cell is pulling on a proximal Au-spot, as anticipated by considering the spring constant experienced by cells with a proximal focal adhesion ($k_P = 313\,\text{nN}\,\mu\text{m}^{-1}$). Thus the histogram in Fig. 6.6C can be considered as a good estimation of the overall noise, mainly due to manual tracking. Conversely, when cellular processes adhere on the distal part of the cantilever, the effect of traction forces results in a clear spreading of the distribution, with a threefold increase of the standard deviation to a value of 1.5 μm, and a range of displacements spanning from −6.5 to 7.3 μm. This proves that this technique allows for the measurement of displacements generated by cells pulling on distal Au spots. Hence, CTFs applied at distal adhesions can be calculated by multiplying $r(t)$ by the distal spring constant $k_D = 5.5\,\text{nN}\,\mu\text{m}^{-1}$. Consequently, maximum forces of about 40 nN were observed in our experiment (6.6D). The time course of LPA-induced CTFs has been analysed as well. The average displacement $\langle r(t) \rangle$ was calculated for each time point for the two families of cantilevers and is plotted in Fig. 6.6B. The characteristic dynamics induced by LPA is found for cantilevers loaded at the distal Au spot, with an initial contraction period of about 15 min followed by force relaxation. After about half an hour $\langle r(t) \rangle$ goes back to 0 μm, meaning that CTFs built up by LPA are loosened. However, the relaxation of forces keeps on going for at least another 30 min, with cantilevers opening in average about 0.6 μm beyond their initial position. This is due to the relaxation of cellular stress established before LPA addition, which kept the cantilevers under tension already before $t = 0$. The relaxation of CTFs – begun at about $t = 15\,\text{min}$ – caused also the loosening of this pre-bending and resulted in the measurement of positive displacements ($r > 0$, opening beyond $r_0$) and in a roughly

symmetrical distribution of $r_{min}$ and $r_{max}$ (Fig. 6.6G). This symmetry between $r_{min}$ ($\leq 0$) and $r_{max}$ ($\geq 0$) means that the CTFs naturally developed in FCS serum before $t = 0$ were of the same order of magnitude of LPA-induced forces, proving the suitability of μ-flowers as a tool to measure CTFs generated by non-stimulated MEFs as well.

## 6.6  Conclusion to this Chapter

Since the pioneering work of Harris [28], which observed wrinkles generated by cell forces on silicone substrates, the techniques used to investigate CTFs have been developed in the direction of a better measurability of the forces [33, 10, 35, 38]. However, all of these advancements were making use of 2D substrata for cell culture. Recently the measurement of CTFs by means of fluorescent beads embedded in soft gels has been extended to 3D matrices [52, 39] opening new possibilities of investigation. Here we proposed a new device for the quantification of CTFs exerted by cells cultured in a 3D configuration, and we proved its potential via a live measurement of CTFs generated by few or single mouse fibroblasts. The positioning of adhesion sites on μ-flowers not only affects the shape and dimensionality of cells, but also localizes the points where CTF are applied. This is crucial for the measurement of cell forces – since the spring constant of a cantilever depends on the point where the load is applied – and represents an improvement with respect to previous approaches in which the load distribution along microstructures was assumed a priori [53]. Attention has to be paid to the fact that each cantilever has two adhesion sites on which cells can pull at the same time. Due to this configuration, the system is in principle statically indeterminate, and there is not a unique solution for two forces acting at the same time on the proximal and on the distal adhesion points, respectively. However, this indeterminacy is negligible in practice, because of the high value of the spring constant at the proximal adhesion point ($k_P = 313\,\text{nN}\,\text{µm}^{-1}$) which does not allow for significant deflections of the cantilever under the typical CTFs strength. This implies that all the observable deflections can be attributed to CTFs applied at the distal Au spot, making the system statically determinate for the calculation of these forces. Nevertheless, another consequence of having steady proximal adhesion points not displaced by CTFs, is that the device is not measuring all the forces generated by cells, but only the ones applied at the distal adhesion sites. Serum has been shown to stimulate the stretching and suspension of

cells in concave microstructures [19]. Since in our experiments we needed cells to be spread and suspended inside the concave shape of μ-flowers, we plated them in serum-containing medium. Cells adhering to μ-flowers under these conditions reached a state of contraction induced by the serum after overnight incubation. In our cellular traction measurements, the level of contraction $r(t)$ without addition of LPA was the value measured at $t(0)$, and this value was set to zero. Even in the presence of serum, LPA induced a burst of RhoA-dependent cell contraction, evidenced by strong negative deflection of $r(t)$ after 10-15 min. Later, $r(t)$ switched to positive values, indicating that the cells relaxed even beyond their original level of traction induced by serum. In this way, positive values of $r(t)$ quantify the FCS-induced contraction (present already before addition of LPA), while negative values of $r(t)$ are a measure of additional LPA-induced tension. The symmetry of the distribution of $r_{min}$ and $r_{max}$ (Fig. 6.6) indicates that the magnitude of FCS-induced tractions is similar to the additional contractile forces due to LPA. The observed CTFs relaxation, after about 15 min from LPA stimulation, might be due to LPA-induced partial detachment of the cells, or to photodamage originating from the tracker dye [94]. The use of cells transfected with GFP-labeled cytoskeletal markers [95] will be needed to clarify this point.

Along with the possibility to measure CTF, μ-flowers are a cell culture substrate well characterized and controllable both mechanically and geometrically. This would help in obtaining more consistent data, differently from more complex systems (e.g. reconstituted matrices) that have less controllable physical properties, especially at sub-cellular scale or upon matrix remodeling. In these latter systems, cells can assume an arbitrary shape, they can adhere randomly, and they experience a non-homogeneous environment, e.g. variable matrix fiber density and fiber orientation (e.g. due to remodeling of the extracellular matrix (ECM) [96]) would result in variable local stiffness, and in a non-homogeneous density of adhesion sites. Moreover, unlike for 3D gels with embedded fluorescent beads, the quantification of CTFs with μ-flowers does not require the use of confocal microscopy [39], reducing phototoxicity and allowing live measurements to be performed with shorter time lapse.

Compared to hydrogels, in which cells can engage freely with the ECM and remain motile [39], our cage-like μ-flowers provide a very distinct biomimetic model, namely one for adult connective tissues (e.g. tendons) in which position, shape, attachment points, and movements of cells are restrained by the very dense ECM. Thus in contrast to hydrogels, μ-flowers allow to

explore physiological conditions where cells cannot respond to the action of matrix-derived strains by evasion (reorientation) and escape (migration), but have to deal with restraints specified by the extracellular 3D substrate.  Since the ability to be suspended in concave structures is dependent on the cell-type [19], hydrogels should be preferred for the assessment of traction forces of non-suspending cells and of small cells (less than 60-70 μm span) that could not reach out the distal adhesion spots of μ-flowers. Another peculiarity of μ-flowers is the spatial organization of focal adhesions, which differ substantially from those on flat 2D substrates. In the latter case contractile actin stress fibers end parallel to the cell surface [97, 98] and generate large shear stresses on focal adhesions, whereas in μ-flowers they are attached roughly perpendicular to the adhesion surface resulting in more normal stresses, as it is the case e.g. for myotendinous junctions in vivo [99]. This makes the proposed system interesting to study the relations between focal adhesion organization and force generation. Other possible applications of the proposed device could be thought in the domains of physi-ological and pharmacological studies on-chip — where the mechanical properties of the cell culture substrates can be engineered in order to mimic the physical conditions found *in vivo*, e.g. as done for beating cardiac cells [7] — or in the domain of micropatterned surfaces, where the response of cells is studied systematically and reproducibly by culturing them on identical substrates [16]. The Au adhesive patterns of μ-flowers could be optimized to control the shape of cells in 3D, similarly to what has been already done in 2D. Indeed, culturing cells into well-defined geometries allows the systematic study of fundamental processes, like division [15] and internal organization of the cell [16]. Altogether, these features make μ-flowers an interesting tool to investigate the effects exerted on cells by the combination of dimensionality and mechanical properties of the microenvironment, while avoiding the technical difficulties encountered with complex 3D matrices.

# 7 Conclusions and Outlook

## 7.1 Conclusions

This work focuses on the fabrication of artificial microenvironments for cell culture, making use of surface microtechnology. The goal was to engineer the mechanical and geometrical properties of cell culture substrates, in order to mimic some relevant physical aspects found *in vivo*. More specifically, we did so at the single cell scale, concentrating our efforts on the realization of three dimensional (3D) microenvironments and on the tuning of their stiffness. The properties of the fabricated devices have been matched to the typical parameters of single cells, both for what concerns geometry and mechanics. In order to adapt the 3D geometry of the microenvironment to the size of a single cell,[1] an approximate target of $R_{\text{targ}} \approx 40\,\mu\text{m}$ was set for the radius of the round microdevices. Similarly, the benchmark used to engineer the mechanical features of the devices is set by the magnitude of cell traction forces (CTFs) and by the rigidity of physiological tissues. CTFs have been measured to be in the order of few tens of nanonewton [10]. In order for them to exert a measurable displacement, the approximate target stiffness of the mechanical elements is set as $k_{\text{targ}} \approx 10\,\text{nN}\,\mu\text{m}^{-1}$, which also corresponds to the elastic modulus of soft tissues such as muscles [77].

Two kinds of devices have been completely developed: hard Si micro-wells and flexible cell-cages based on bent cantilevers (named as µ-flowers).

---

[1] The size of a single cell is not a well defined dimension, since it varies significantly according to the kind of cell considered. Here we refer to the cell model used in this dissertation, i.e. mouse embryonic kidney fibroblasts (MEFs).

**Microwells**

One of the two 3D cell culture substrates is constituted by round microwells etched in silicon. Their most innovative characteristic lays in the possibility to decorate their curved inner surface with micropatterns of arbitrary shape. Stencil lithography is the crucial technique that allowed the deposition of Au patterns onto non-flat surfaces. In order to improve the quality of this deposition, a two-step etching process has been developed, enabling the well shape control. Namely, the maximum steepness of the sidewalls is controlled by the second etching step, allowing for the surface of the well to be at an angle with the deposition beam, instead of parallel (as it is after the first etching step). This improves the uniformity of continuous films, particularly close to the edge of the micro-wells. At this stage, the main limitation of the technique is the impossibility to tune the stiffness of the substrate – made of Si and too hard to mimic the rigidity of physiological tissues. However, the advantage of stencil lithography is that the patterns deposited inside the micro-wells can also be deposited on a two dimensional (2D) flat substrate, making the technique suitable to fabricate equivalent 2D and 3D microenvironments, which are identical except for the dimensionality. Therefore, these systems are a potential tool to study the effects of the microenvironment dimensionality on cells.

**Micro-flowers**

The second device (μ-flowers) enabled the mechanical properties of the microenvironment to be engineered, while retaining the 3D shape. The use of flexible cantilevers with different thicknesses provided stiffness control, while the 3D shape was attained by exploiting the intrinsic stress of the beams, which bends them out-of-plane.

Firstly, a monolayer of silicon oxide served as the building material of the cantilevers. Different oxidation temperatures have been systematically tested in order to have different stress profiles, and hence different bending radii. The behavior of wet oxide, though, deviated from the modeled one, showing a monotonic dependence of $R$ vs. the oxidation temperature $T$. We hypothesize that this discrepancy between experiments ad simulations is due to a

different viscosity of $SiO_2$ prepared by wet oxidation (opening of Si-O-Si bonds by means of hydrogen). Radii small enough for single cell culture have been reached by back etching the oxide layer to lower thicknesses of about 80 to 100 nm. At the same time, *via* thinning of the $SiO_2$ beams, the stress profile of the oxide was heuristically retrieved, assuming some properties of its shape *a priori* (according to the Fargeix's model of viscous flow relaxation [75]). Since the target radius of $\approx 30 \mu m$ is attainable only for very thin cantilevers, the spring constant is limited to valued of $k \approx 0.1 - 1 \, \mathrm{nN} \, \mu m^{-1}$, corresponding to extremely soft tissues (neuronal [77]).

A second generation of cantilevers expanded significantly the range of attainable stiffnesses. The combination of Ti and $SiO_2$ layers, with opposite tensile-compressive stresses, increased the bending moment and allowed stiffer cantilevers to bend at the right scale of the single cell ($R \sim 30 \mu m$). An empirical, combinatorial approach has been used to find out the proper thicknesses of Ti and $SiO_2$. Seven Ti-$SiO_2$ combinations, out of the sixteen investigated, were found to have the right radius, while being characterized by different stiffnesses. The bilayer technique greatly enlarged the range of achievable spring constants: $k \approx 1 - 80 \, \mathrm{nN} \, \mu m^{-1}$. In this way it is possible to mimic the physiological rigidity of a variety of tissues (e.g. neural, fat, muscles, cartilage, non-calcified bone [77]). Similar to the case of micro-wells, Au deposition has been used to create micropatterns, in the shape of rectangular spots deposited on the cantilevers. In this case, however, Au spots are fabricated before releasing the cantilevers from the substrate, when they are still flat, using standard lithographic techniques instead of stencil masks.

**Validation with Cells**

Concerning cell culture, a functionalization protocol has been used with the goal of localizing cell adhesions. First, a peptide that acts as a ligand for integrin was selectively adsorbed on the surface of Au spots. Afterwards, the microenvironments were passivated against cell adhesion, by adsorption of poly(L-lysine)-*grafted*-poly(ethylene glycol) (PLL-*g*-PEG) on all the non-Au surfaces. In this way, cellular focal adhesions (FAs) – the anchors through which cells exert traction forces on their surroundings – have been localized onto the adhesive Au spots. The localization of cell adhesions at the end of the cantilevers allowed cell forces to be quantified

from the deflections $\delta$ of the beams ($F = k \cdot \delta$). This proved that µ-flowers, beside mimicking physiological stiffnesses, can also be used as force gauge at the single cell scale. More than 10 000 µ-flowers per chip were fabricated in various configurations (number and length of bent cantilevers), making the proposed device suitable for the parallelization of experiments, and the acquisition of statistically relevant data.

## 7.2   Outlook

Some improvements and applications for the patterned microwells and for µ-flowers are envisaged below.

A technical advancement for the **treatment of acquired images** has to be foreseen in order to process higher amounts of data more effectively and unfurl the parallelization potential of the microfabricated devices. Namely, a program for the automatic tracking of cantilever deflection will boost the applicability of the tool and the efficiency of the biological experiments that can be performed. In the same perspective, the analysis of 3D images could be automatized also for other parameters, e.g. to quantify and compare cell morphology (surface to volume ratio, presence of cell processes, etc.). A better knowledge of cell shapes would be beneficial for more precise force measurements as well, since not only the location of CTFs, but also their orientation, could be better assessed. In the same direction of improving the quantification of cell force, further and more detailed measurement of the spring constants could be performed.

**The effects of dimensionality** on cell behavior could be studied using the fabricated 3D microenvironments and the corresponding flat 2D patterns. The easiest way to make such a comparison, in terms of fabrication, would be considering the patterned microwells and the Si flat substrates patterned using the same stencil mask. The morphology of cells in the two cases could be compared, as well as the spatial distribution of selected proteins, which can enlighten the mechanical structure of cells (e.g. F-actin, tubulin) and the organization of FA (vinculin).

**The effects of the stiffness** could be investigated in a similar way, this time using µ-flowers with the same geometry ($R$), but with different rigidity. Finally, a comparison based on both geometry and mechanics could be conceived by comparing microenvronments of various stiffnesses, both in 2D and 3D. This could be achieved by fabricating a 2D equivalent of
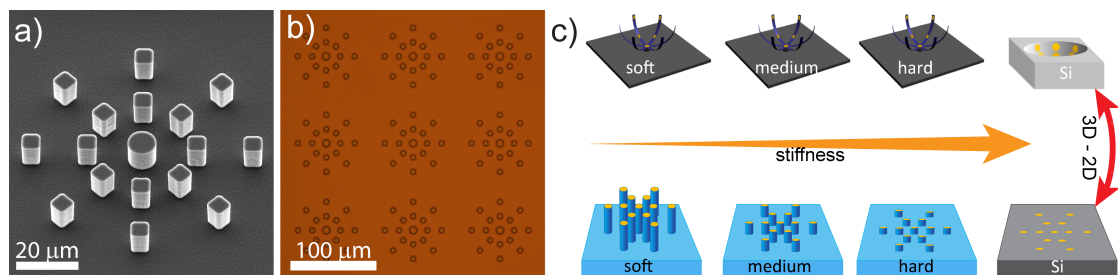
Figure 7.1: 2D equivalent of μ-flowers. **a)**: SEM micrograph showing the Si master mold for the fabrication of PDMS 2D μ-flowers. **b)**: optical micrograph of 2D μ-flowers replicated in PDMS. **c)**: schematic of a potential palette of tools to study the effects of the dimensionality and stiffness of the cell culture substrate. The stiffness of 2D μ-flowers can be changed by varying the base/cross-linker ratio of PDMS and/or the height of the pillars. A suitable functionalization protocol should be envisaged, in order to have the same biomolecules on all the devices.

μ-flowers, using vertical poly(dimethylsiloxane) (PDMS) pillars arranged in the same way as Au spots in μ-flowers, and with length and Young's modulus designed in order to give the same stiffness of bent cantilevers (Fig. 7.1).

The realization of Au patterns deposited *via* stencil lithography could be tested as well using microwells made out of softer materials, e.g. PDMS.

# Bibliography

[1] D.-H. Kim, A. B. Chambliss, and D. Wirtz, "The multi-faceted role of the actin cap in cellular mechanosensation and mechanotransduction," *Soft Matter*, vol. 9, pp. 5516–5523, 2013.

[2] R. J. Pelham and Y.-l. Wang, "Cell locomotion and focal adhesions are regulated by substrate flexibility," *Proceedings of the National Academy of Sciences of the United States of America*, vol. 94, no. 25, pp. 13661–13665, 1997.

[3] C. Garrido, S. Gurbuxani, L. Ravagnan, and G. Kroemer, "Heat shock proteins: endogenous modulators of apoptotic cell death," *Biochemical and biophysical research communications*, vol. 286, no. 3, pp. 433–442, 2001.

[4] J. T. Francis, B. J. Gluckman, and S. J. Schiff, "Sensitivity of neurons to weak electric fields," *The Journal of neuroscience*, vol. 23, no. 19, pp. 7255–7261, 2003.

[5] D. J. Beebe, D. E. Ingber, and J. den Toonder, "Organs on chips 2013," *Lab on a Chip*, 2013.

[6] E. Ghafar-Zadeh, J. R. Waldeisen, and L. P. Lee, "Engineered approaches to the stem cell microenvironment for cardiac tissue regeneration," *Lab on a Chip*, vol. 11, no. 18, pp. 3031–3048, 2011.

[7] A. Grosberg, P. W. Alford, M. L. McCain, and K. K. Parker, "Ensembles of engineered cardiac tissues for physiological and pharmacological study: Heart on a chip," *Lab on a Chip*, vol. 11, no. 24, pp. 4165–4173, 2011.

**Bibliography**

[8] M. Nikkhah, F. Edalat, S. Manoucheri, and A. Khademhosseini, "Engineering microscale topographies to control the cell-substrate interface," *Biomaterials*, vol. 33, no. 21, pp. 5230 – 5246, 2012.

[9] T. Yeung, P. C. Georges, L. A. Flanagan, B. Marg, M. Ortiz, M. Funaki, N. Zahir, W. Ming, V. Weaver, and P. A. Janmey, "Effects of substrate stiffness on cell morphology, cytoskeletal structure, and adhesion," *Cell motility and the cytoskeleton*, vol. 60, no. 1, pp. 24–34, 2005.

[10] J. L. Tan, J. Tien, D. M. Pirone, D. S. Gray, K. Bhadriraju, and C. S. Chen, "Cell lying on a bed of microneedles: an approach to isolate machanical force," *Proceedings of the National Academy of Sciences of the United States of America*, vol. 100, no. 4, pp. 1484–89, 2003.

[11] J. Fu, Y.-K. Wang, M. T. Yang, R. A. Desai, X. Yu, Z. Liu, and C. S. Chen, "Mechanical regulation of cell function with geometrically modulated elastomeric substrates," *Nat Meth*, vol. 7, no. 9, pp. 733–736, 2010. 10.1038/nmeth.1487.

[12] W. R. Legant, A. Pathak, M. T. Yang, V. S. Deshpande, R. M. McMeeking, and C. S. Chen, "Microfabricated tissue gauges to measure and manipulate forces from 3d microtissues," *Proceedings of the National Academy of Sciences*, vol. 106, no. 25, pp. 10097–10102, 2009.

[13] C. S. Chen, M. Mrksich, S. Huang, G. M. Whitesides, and D. E. Ingber, "Geometric control of cell life and death," *Science*, vol. 276, no. 5317, pp. 1425–1428, 1997.

[14] R. Lutz, K. Pataky, N. Gadhari, M. Marelli, J. Brugger, and M. Chiquet, "Nano-stenciled rgd-gold patterns that inhibit focal contact maturation induce lamellipodia formation in fibroblasts," *PLoS ONE*, vol. 6, no. 9, p. e25459, 2011.

[15] M. Théry, A. Jimenez-Dalmaroni, V. Racine, M. Bornens, and F. Julicher, "Experimental and theoretical study of mitotic spindle orientation," *Nature*, vol. 447, no. 7143, pp. 493–496, 2007.

[16] M. Théry, V. Racine, M. Piel, A. Pépin, A. Dimitrov, Y. Chen, J.-B. Sibarita, and M. Bornens, "Anisotropy of cell adhesive microenvironment governs cell internal organization and orientation of polarity," *Proceedings of the National Academy of Sciences*, vol. 103, no. 52, pp. 19771–19776, 2006.

[17] S. Giselbrecht, T. Gietzelt, E. Gottwald, C. Trautmann, R. Truckenmuller, K. F. Weibezahn, and A. Welle, "3d tissue culture substrates produced by microthermoforming of pre-processed polymer films," *Biomedical Microdevices*, vol. 8, no. 3, pp. 191–199, 2006.

[18] E. Gottwald, S. Giselbrecht, C. Augspurger, B. Lahni, N. Dambrowsky, R. Truckenmuller, V. Piotter, T. Gietzelt, O. Wendt, W. Pfleging, A. Welle, A. Rolletschek, A. M. Wobus, and K. F. Weibezahn, "A chip-based platform for the in vitro generation of tissues in three-dimensional organization," *Lab on a Chip*, vol. 7, no. 6, pp. 777–785, 2007.

[19] M. Nikkhah, J. S. Strobl, B. Peddi, and M. Agah, "Cytoskeletal role in differential adhesion patterns of normal fibroblasts and breast cancer cells inside silicon microenvironments," *Biomedical Microdevices*, vol. 11, no. 3, pp. 585–595, 2009.

[20] M. Nikkhah, J. S. Strobl, R. De Vita, and M. Agah, "The cytoskeletal organization of breast carcinoma and fibroblast cells inside three dimensional (3-d) isotropic silicon microstructures," *Biomaterials*, vol. 31, no. 16, pp. 4552–4561, 2010.

[21] M. Ochsner, M. Textor, V. Vogel, and M. L. Smith, "Dimensionality controls cytoskeleton assembly and metabolism of fibroblast cells in response to rigidity and shape," *PLoS ONE*, vol. 5, no. 3, p. e9445, 2010.

[22] K. Hayakawa, H. Tatsumi, and M. Sokabe, "Actin stress fibers transmit and focus force to activate mechanosensitive channels," *Journal of Cell Science*, vol. 121, no. 4, pp. 496–503, 2008.

[23] A. R. Gingras, K.-P. Vogel, H.-J. Steinhoff, W. H. Ziegler, B. Patel, J. Emsley, D. R. Critchley, G. C. Roberts, and I. L. Barsukov, "Structural and dynamic characterization of a vinculin binding site in the talin rod," *Biochemistry*, vol. 45, no. 6, pp. 1805–1817, 2006.

[24] E. Papagrigoriou, A. R. Gingras, I. L. Barsukov, N. Bate, I. J. Fillingham, B. Patel, R. Frank, W. H. Ziegler, G. C. Roberts, and D. R. Critchley, "Activation of a vinculin-binding site in the talin rod involves rearrangement of a five-helix bundle," *The EMBO journal*, vol. 23, no. 15, pp. 2942–2951, 2004.

[25] B. Geiger, J. P. Spatz, and A. D. Bershadsky, "Environmental sensing through focal adhesions," *Nat Rev Mol Cell Biol*, vol. 10, no. 1, pp. 21–33, 2009. 10.1038/nrm2593.

[26] U. S. Schwarz, T. Erdmann, and I. B. Bischofs, "Focal adhesions as mechanosensors: the two-spring model," *Biosystems*, vol. 83, no. 2, pp. 225–232, 2006.

[27] C.-M. Lo, H.-B. Wang, M. Dembo, and Y.-l. Wang, "Cell movement is guided by the rigidity of the substrate," *Biophysical Journal*, vol. 79, no. 1, pp. 144–152, 2000. 0006-3495 doi: DOI: 10.1016/S0006-3495(00)76279-5.

[28] A. K. Harris, P. Wild, and D. Stopak, "Silicone rubber substrata: a new wrinkle in the study of cell locomotion," *Science*, vol. 208, no. 4440, pp. 177–9, 1980.

[29] A. K. Harris, D. Stopak, and P. Wild, "Fibroblast traction as a mechanism for collagen morphogenesis," *Nature*, vol. 290, no. 5803, pp. 249–251, 1981. 10.1038/290249a0.

[30] J. Lee, M. Leonard, T. Oliver, A. Ishihara, and K. Jacobson, "Traction forces generated by locomoting keratocytes," *The Journal of Cell Biology*, vol. 127, no. 6, pp. 1957–1964, 1994.

[31] T. Oliver, K. Jacobson, and M. Dembo, "Traction forces in locomoting cells," *Cell Motility and the Cytoskeleton*, vol. 31, no. 3, pp. 225–240, 1995.

[32] M. Dembo, T. Oliver, A. Ishihara, and K. Jacobson, "Imaging the traction stresses exerted by locomoting cells with the elastic substratum method," *Biophysical Journal*, vol. 70, no. 4, pp. 2008–2022, 1996.

[33] M. Dembo and Y.-L. Wang, "Stresses at the cell-to-substrate interface during locomotion of fibroblasts," *Biophysical Journal*, vol. 76, no. 4, pp. 2307–2316, 1999.

[34] Y.-L. Wang and R. J. Pelham Jr, "Preparation of a flexible, porous polyacrylamide substrate for mechanical studies of cultured cells," *Methods in enzymology*, vol. 298, pp. 489–496, 1998.

[35] C. G. Galbraith and M. P. Sheetz, "A micromachined device provides a new bend on fibroblast traction forces," *Proceedings of the National Academy of Sciences of the United States of America*, vol. 94, no. 17, pp. 9114–9118, 1997.

[36] N. J. Sniadecki, A. Anguelouch, M. T. Yang, C. M. Lamb, Z. Liu, S. B. Kirschner, Y. Liu, D. H. Reich, and C. S. Chen, "Magnetic microposts as an approach to apply forces to living

cells," *Proceedings of the National Academy of Sciences of the United States of America*, vol. 104, no. 37, pp. 14553–14558, 2007.

[37] S. A. Maskarinec, C. Franck, D. A. Tirrell, and G. Ravichandran, "Quantifying cellular traction forces in three dimensions," *Proceedings of the National Academy of Sciences*, vol. 106, no. 52, pp. 22108–22113, 2009.

[38] H. Delanoë-Ayari, J. P. Rieu, and M. Sano, "4d traction force microscopy reveals asymmetric cortical forces in migrating dictyostelium cells," *Physical Review Letters*, vol. 105, no. 24, p. 248103, 2010.

[39] W. R. Legant, J. S. Miller, B. L. Blakely, D. M. Cohen, G. M. Genin, and C. S. Chen, "Measurement of mechanical tractions exerted by cells in three-dimensional matrices," *Nat Meth*, vol. 7, no. 12, pp. 969–971, 2010.

[40] A. Béduer, C. Vieu, F. Arnauduc, J.-C. Sol, I. Loubinoux, and L. Vaysse, "Engineering of adult human neural stem cells differentiation through surface micropatterning," *Biomaterials*, vol. 33, no. 2, pp. 504–514, 2012.

[41] R. Truckenmuller, S. Giselbrecht, M. Escalante-Marun, M. Groenendijk, B. Papenburg, N. Rivron, H. Unadkat, V. Saile, V. Subramaniam, A. van den Berg, C. van Blitterswijk, M. Wessling, J. de Boer, and D. Stamatialis, "Fabrication of cell container arrays with overlaid surface topographies," *Biomedical Microdevices*, vol. 14, no. 1, pp. 95–107, 2012.

[42] O. Vazquez-Mena, L. Villanueva, V. Savu, K. Sidler, P. Langlet, and J. Brugger, "Analysis of the blurring in stencil lithography," *Nanotechnology*, vol. 20, p. 415303, 2009.

[43] V. Svetovoy, J. Berenschot, and M. Elwenspoek, "Experimental investigation of anisotropy in isotropic silicon etching," *Journal of Micromechanics and Microengineering*, vol. 17, no. 11, p. 2344, 2007.

[44] H. Robbins and B. Schwartz, "Chemical etching of silicon I. the system HF $HNO_3$ $H_2O$ and $HC_2H_3O_2$," *Journal of the electrochemical society*, vol. 106, no. 6, pp. 505–508, 1959.

[45] H. Robbins and B. Schwartz, "Chemical etching of silicon II. the system HF $HNO_3$ $H_2O$ and $HC_2H_3O_2$," *Journal of the electrochemical society*, vol. 107, no. 2, pp. 108–111, 1960.

[46] B. Schwartz and H. Robbins, "Chemical etching of silicon: IV . etching technology," *Journal of the electrochemical society*, vol. 123, no. 12, pp. 1903–1909, 1976.

[47] M. Chiquet, L. Gelman, R. Lutz, and S. Maier, "From mechanotransduction to extracellular matrix gene expression in fibroblasts," *Biochimica Et Biophysica Acta-Molecular Cell Research*, vol. 1793, no. 5, pp. 911–920, 2009.

[48] A. Sarasa-Renedo, V. Tunc-Civelek, and M. Chiquet, "Role of rhoa/rock-dependent actin contractility in the induction of tenascin-c by cyclic tensile strain," *Experimental Cell Research*, vol. 312, no. 8, pp. 1361–1370, 2006.

[49] J. Wang and J.-S. Lin, "Cell traction force and measurement methods," *Biomechanics and Modeling in Mechanobiology*, vol. 6, no. 6, pp. 361–371, 2007.

[50] E. Cukierman, R. Pankov, D. R. Stevens, and K. M. Yamada, "Taking cell-matrix adhesions to the third dimension," *Science*, vol. 294, no. 5547, pp. 1708–1712, 2001.

[51] M. A. Wozniak and C. S. Chen, "Mechanotransduction in development: a growing role for contractility," *Nat Rev Mol Cell Biol*, vol. 10, no. 1, pp. 34–43, 2009.

[52] T. M. Koch, S. Munster, N. Bonakdar, J. P. Butler, and B. Fabry, "3d traction forces in cancer cell invasion," *PLoS ONE*, vol. 7, no. 3, p. e33476, 2012.

[53] M. Ghibaudo, J.-M. Di Meglio, P. Hersen, and B. Ladoux, "Mechanics of cell spreading within 3d-micropatterned environments," *Lab on a Chip*, vol. 11, no. 5, pp. 805–812, 2011.

[54] J. Sharpe, W. N., J. Pulskamp, D. S. Gianola, C. Eberl, R. G. Polcawich, and R. J. Thompson, "Strain measurements of silicon dioxide microspecimens by digital imaging processing," *Experimental Mechanics*, vol. 47, no. 5, pp. 649–658, 2007.

[55] K. E. Petersen and C. R. Guarnieri, "Young's modulus measurements of thin films using micromechanics," *Journal of Applied Physics*, vol. 50, no. 11, pp. 6761–6766, 1979.

[56] T. P. Weihs, S. Hong, J. C. Bravman, and W. D. Nix, "Mechanical deflection of cantilever microbeams: A new technique for testing the mechanical properties of thin films," *Journal of Materials Research*, vol. 3, no. 05, pp. 931–942, 1988.

[57] T. Tsuchiya, M. Hirata, and N. Chiba, "Young's modulus, fracture strain, and tensile strength of sputtered titanium thin films," *Thin Solid Films*, vol. 484, no. 1-2, pp. 245–250, 2005.

[58] Z. Shan and S. K. Sitaraman, "Elastic-plastic characterization of thin films using nanoindentation technique," *Thin Solid Films*, vol. 437, no. 1-2, pp. 176–181, 2003.

[59] W. Young and R. Budynas, *Roark's formulas for stress and strain*, vol. 494. McGraw-Hill New York, 2002.

[60] M. M. Gauthier, *Engineered materials handbook*. Materials Park, OH: ASM International, 1995.

[61] M. Ghibaudo, A. Saez, L. Trichet, A. Xayaphoummine, J. Browaeys, P. Silberzan, A. Buguin, and B. Ladoux, "Traction forces and rigidity sensing regulate cell functions," *Soft Matter*, vol. 4, no. 9, pp. 1836–1843, 2008.

[62] L. D. Landau and L. E. Mikhailovich, *Course of Theoretical Physics*, vol. 7. Pergamon press, 2nd ed., 1970.

[63] I. Schoen, "Substrate-mediated crosstalk between elastic pillars," *Applied Physics Letters*, vol. 97, no. 2, pp. 023703–3, 2010.

[64] D.-H. Kim and D. Wirtz, "Focal adhesion size uniquely predicts cell migration," *The FASEB Journal*, vol. 27, pp. 1351–1361, 2013.

[65] L. Zhang, L. Dong, D. J. Bell, B. J. Nelson, C. Schönenberger, and D. Grützmacher, "Fabrication and characterization of freestanding si/cr micro- and nanospirals," *Microelectronic Engineering*, vol. 83, no. 4, pp. 1237 – 1240, 2006.

[66] J. A. Thornton and D. W. Hoffman, "Stress-related effects in thin films," *Thin Solid Films*, vol. 171, no. 1, pp. 5–31, 1989.

[67] M. Vert, K.-H. Hellwich, M. Hess, P. Hodge, P. Kubisa, M. Rinaudo, and F. Schué, "Terminology for biorelated polymers and applications (iupac recommendations 2012)," *Pure and Applied Chemistry*, vol. 84, no. 2, pp. 377–410, 2012.

[68] G. Kotzar, M. Freas, P. Abel, A. Fleischman, S. Roy, C. Zorman, J. M. Moran, and J. Melzak, "Evaluation of mems materials of construction for implantable medical devices," *Biomaterials*, vol. 23, no. 13, pp. 2737–2750, 2002.

[69] M. Maeda and K. Ikeda, "Stress evaluation of radio-frequency-biased plasma-enhanced chemical vapor deposited silicon nitride films," *Journal of Applied Physics*, vol. 83, no. 7, pp. 3865–3870, 1998.

[70] S. King, R. Chu, G. Xu, and J. Huening, "Intrinsic stress effect on fracture toughness of plasma enhanced chemical vapor deposited $sin_x$: H films," *Thin Solid Films*, vol. 518, no. 17, pp. 4898–4907, 2010.

[71] D. L. Elbert and J. A. Hubbell, "Self-assembly and steric stabilization at heterogeneous, biological surfaces using adsorbing block copolymers," *Chemistry and Biology*, vol. 5, no. 3, pp. 177–183, 1998.

[72] R. Michel, J. W. Lussi, G. Csucs, I. Reviakine, G. Danuser, B. Ketterer, J. A. Hubbell, M. Textor, and N. D. Spencer, "Selective molecular assembly patterning: A new approach to micro- and nanochemical patterning of surfaces for biological applications," *Langmuir*, vol. 18, no. 8, pp. 3281–3287, 2002.

[73] B. E. Deal and A. S. Grove, "General relationship for the thermal oxidation of silicon," *Journal of Applied Physics*, vol. 36, no. 12, pp. 3770–3778, 1965.

[74] R. C. Jaeger, *Introduction to Microelectronic Fabrication*. Upper Saddle River: Prentice Hall, 2nd ed., 2002.

[75] A. Fargeix and G. Ghibaudo, "Dry oxidation of silicon: A new model of growth including relaxation of stress by viscous flow," *Journal of Applied Physics*, vol. 54, no. 12, pp. 7153–7158, 1983.

[76] D. E. Discher, P. Janmey, and Y.-l. Wang, "Tissue cells feel and respond to the stiffness of their substrate," *Science*, vol. 310, no. 5751, pp. 1139–1143, 2005.

[77] D. E. Discher, D. J. Mooney, and P. W. Zandstra, "Growth factors, matrices, and forces combine and control stem cells," *Science*, vol. 324, no. 5935, pp. 1673–1677, 2009.

[78] O. du Roure, A. Saez, A. Buguin, R. H. Austin, P. Chavrier, and P. Silberzan, "Force mapping in epithelial cell migration," *Proceedings of the National Academy of Sciences of the United States of America*, vol. 102, no. 7, pp. 2390–95, 2005.

[79] A. J. Engler, M. A. Griffin, S. Sen, C. G. Bonnemann, H. L. Sweeney, and D. E. Discher, "Myotubes differentiate optimally on substrates with tissue-like stiffness: pathological implications for soft or stiff microenvironments," *The Journal of Cell Biology*, vol. 166, no. 6, pp. 877–887, 2004.

[80] D. J. Breed and R. H. Doremus, "Hydrogen profiles in water-oxidized silicon," *The Journal of Physical Chemistry*, vol. 80, no. 22, pp. 2471–2473, 1976.

[81] E. P. Eernisse, "Viscous-flow of thermal sio2," *Applied Physics Letters*, vol. 30, no. 6, pp. 290–293, 1977.

[82] F. P. Eernisse, "Stress in thermal sio2 during growth," *Applied Physics Letters*, vol. 35, no. 1, pp. 8–10, 1979.

[83] J. T. Fitch, G. Lucovsky, E. Kobeda, and E. A. Irene, "Effects of thermal history on stress-related properties of very thin films of thermally grown silicon dioxide," *Journal of Vacuum Science and Technology*, vol. 7, no. 2, pp. 153–166, 1988.

[84] J. Fitch, C. Bjorkman, G. Lucovsky, F. Pollak, and X. Yin, "Intrinsic stress and stress gradients at the sio2-si interface in structures prepared by thermal oxidation of si and subjected to rapid thermal annealing," *Journal of Vacuum Science and Technology B: Microelectronics and Nanometer Structures*, vol. 7, no. 4, pp. 775–781, 1989.

[85] H. Guckel, D. Burns, C. Rutigliano, E. Lovell, and B. Choi, "Diagnostic microstructures for the measurement of intrinsic strain in thin films," *Journal of Micromechanics and Microengineering*, vol. 2, no. 2, pp. 86–95, 1992.

[86] H. Tsai and W. Fang, "Diagnostic microstructures for the measurement of intrinsic strain in thin films," *Sensors and Actuators*, no. 103, pp. 377–383, 2002.

[87] H. Watanabe, N. Yamada, and M. Okaji, "Linear thermal expansion coefficient of silicon from 293 to 1000 k," *International Journal of Thermophysics*, vol. 25, no. 1, pp. 221–236, 2004.

# Bibliography

[88] L. A. Flanagan, Y.-E. Ju, B. Marg, M. Osterfield, and P. A. Janmey, "Neurite branching on deformable substrates," *Neuroreport*, vol. 13, no. 18, p. 2411, 2002.

[89] H. J. Schneeweiss and R. Abermann, "Ultra-high vacuum measurements of the internal stress of pvd titanium films as a function of thickness and its dependence on substrate temperature," *Vacuum*, vol. 43, no. 5-7, pp. 463–465, 1992.

[90] J. Lausmaa, B. Kasemo, and H. Mattsson, "Surface spectroscopic characterization of titanium implant materials," *Applied Surface Science*, vol. 44, no. 2, pp. 133–146, 1990.

[91] N.-P. Huang, R. Michel, J. Voros, M. Textor, R. Hofer, A. Rossi, D. L. Elbert, J. A. Hubbell, and N. D. Spencer, "Poly(l-lysine)-g-poly(ethylene glycol) layers on metal oxide surfaces: Surface-analytical characterization and resistance to serum and fibrinogen adsorption," *Langmuir*, vol. 17, no. 2, pp. 489–498, 2000.

[92] M. Ohring, *Materials science of thin films*. Academic press, 1993.

[93] W. S. Rasband, "Imagej," 1997-2013.

[94] J. M. Zdolsek, "Acridine orange-mediated photodamage to cultured cells," *APMIS*, vol. 101, no. 1-6, pp. 127–132, 1993.

[95] J. Riedl, A. H. Crevenna, K. Kessenbrock, J. H. Yu, D. Neukirchen, M. Bista, F. Bradke, D. Jenne, T. A. Holak, Z. Werb, M. Sixt, and R. Wedlich-Soldner, "Lifeact: a versatile marker to visualize f-actin," *Nat Meth*, vol. 5, no. 7, pp. 605–607, 2008.

[96] M. K.-R. Casey, P. C. Shawn, P. C. Joseph, N. S. Brooke, and A. R.-K. Cynthia, "The role of the cytoskeleton in cellular force generation in 2d and 3d environments," *Physical Biology*, vol. 8, no. 1, p. 015009, 2011.

[97] K. Burridge, "Substrate adhesions in normal and transformed fibroblasts: organization and regulation of cytoskeletal, membrane and extracellular matrix components at focal contacts," *Cancer Rev*, vol. 4, pp. 18–78, 1986.

[98] J. V. Small, K. Rottner, I. Kaverina, and K. Anderson, "Assembling an actin cytoskeleton for cell attachment and movement," *Biochimica et Biophysica Acta (BBA)-Molecular Cell Research*, vol. 1404, no. 3, pp. 271–281, 1998.

[99] B. Sharafi, E. G. Ames, J. W. Holmes, and S. S. Blemker, "Strains at the myotendinous junction predicted by a micromechanical model," *Journal of Biomechanics*, vol. 44, no. 16, pp. 2795–2801, 2011.

# Appendices

# A Curriculum Vitae and Publications

## Personal Data

|  |  |
|---|---|
| **Name** | Mattia Marelli |
| **Date of bith** | 05 March 1983 |
| **Place of birth** | Cantù (Como), Italy |
| **Nationality** | Italian |

## Education

| | |
|---|---|
| **2009–present** | Ph.D. candidate in in Microsystems and Microelectronics, École Polytechnique Fédérale de Lausanne (EPFL), Lausanne, Switzerland |
| **2006–2009** | Master in Physics, Università Statale degli Studi, Milan, Italy |
| **2002–2006** | Bachelor in Physics,Università Statale degli Studi,Milan, Italy |

## Professional Experience

**2009–2013**  Research and teaching assistant in Microsystems Laboratory (LMIS1), EPFL, Switzerland

**Apr–Sept 2009**  Research assistant, C.I.Ma.I.Na (Interdisciplinary Center for Nanostructured Materials and Interfaces), Milan, Italy

## Languages

**Italian**  Mother tongue

**English**  Fluent

**French**  Fluent

**German**  Basic

## Publication List

### Papers done at Microsystems Laboratory

1. **M. Marelli**, N. Gadhari, G. Boero, M. Chiquet and J. Brugger, "Cell force measurements in 3D microfabricated environments based on compliant cantilevers", *Lab on a Chip*, 14 (2014) 286-93.

2. N. Gadhari, M. Charnley, **M. Marelli**, J. Brugger, M. Chiquet, "Cell shape-dependent early responses of fibroblasts to cyclic strain", *Biochimica et Biophysica Acta - Molecular Cell Research*, 1833 (2013) 3415-25.

3. R. Lutz, K. Pataky, N. Gadhari, **M. Marelli**, J. Brugger and M. Chiquet, "Nano-Stenciled RGD-Gold Patterns That Inhibit Focal Contact Maturation Induce Lamellipodia Formation in Fibroblasts", *PLoS ONE*, 6 (2011) e25459.

## Conferences done at Microsystems Laboratory

1. **M. Marelli**, N. Gadhari, G. Boero, M. Chiquet and J. Brugger, "Single-cell 3D bio-MEMS environment with engineered geometry and physiologically relevant stiffnesses", *The 27*[th] *IEEE International Conference on Micro Electro Mechanical Systems (MEMS 2014)*, San Francisco, CA, January 2014 (accepted, oral presentation).

2. **M. Marelli**, N. Gadhari, P. Biro, M. Chiquet and J. Brugger, "Micro-beams with tunable stiffness and curvature for mechano-sensitive cell culture substrates", *37*[th] *International Conference on Micro and Nano Engineering (MNE 2011)*, Berlin, Germany, Sept. 2011, oral presentation.

3. **M. Marelli**, O. Vazquez-Mena, K. Pataky, P. Mato Sabat, J. Brugger, "Micro and nano tools for life science applications", *TransAlp'Nano Conference*, Como, Italy, June 2011, poster.

## Previous Papers

1. G. Corbelli, C. Ghisleri, **M. Marelli**, P. Milani and L. Ravagnan, "Highly Deformable Nanostructured Elastomeric Electrodes With Improving Conductivity Upon Cyclical Stretching", *Advanced Materials*, 23 (2011) 4504.

2. **M. Marelli**, G. Divitini, C. Collini, L. Ravagnan, G. Corbelli, C. Ghisleri, A. Gianfelice, C. Lenardi, P. Milani and L. Lorenzelli, "Flexible and biocompatible microelectrode arrays fabricated by supersonic cluster beam deposition on SU-8", *Journal of Micromechanics and Microengineering*, 21 (2011) 045013.

3. L. Ravagnan, G. Divitini, S. Rebasti, **M. Marelli**, P. Piseri and P. Milani, "Poly(methyl methacrylate)-palladium clusters nanocomposite formation by supersonic cluster beam deposition: a method for microstructured metallization of polymer surfaces", *Journal of Applied Physics D*, 42 (2009) 082002.

# Acknowledgements

This thesis would not be complete without acknowledging the many persons who made it possible, by giving their fundamental contribution.

I first wish to thank my advisor Prof. Jürgen Brugger, for creating a friendly group and environment in which it was nice working. Thanks also for heaving left me much freedom about the research done over the last four years. The financial support was provided by the Swiss National Science Foundation (SNSF) under the grants nos. 125290 and 140623. A special thanks to Prof. Roman Truckenmüller, Prof. Matthias Chiquet and Prof. Giovanni Dietler for having accepted to be jury members for my thesis defense, and for having read and corrected it. Thanks to Prof. Herb Shea for having been the president of the jury.

I owe a great acknowledgement to the researchers that have shared with me these years: Dr. Neha Gadhari and Sylke Höhnel for their help and support with cell culture, and for the common investigations discussed and performed together; Mirren Charnely for helping with the functionalization; Prof. Matthias Chiquet, for his passion for science and deep insight in cell biology; Prof. Matthias Lutolf and Prof. Marcus Textor for being valuable partners. All the micro-fabrication was done in the EPFL Center of Microtechnology (CMi): thanks to all the staff members working there, because you make it a very open and educational facility, keeping it at a very high professional level. Particularly, I would like to thank Cyrille Hibert, Anthony Guillet, Joffrey Pernollet, Jean-Marie Voirol, Zdenek Benes, Georges-André Racine, Claudia D'Agostino, Jean-Baptiste Bureau and Boris Lunardi.

Thanks also to the Interdisciplinary Centre for Electron Microscopy (CIME) and to the Bioimaging and Optics Platform (PtBiOp) and its extremely friendly collaborators, in particular

supported me in my choices, accepting all of them with great freedom; my brother Alessandro for his love towards his little brother, and for being an example to me; my brother Paolo for being always with us all; Beatrice for being a tireless partner along our path and for being crucial to my growth... though a bit crazy.

*Lausanne, 16 January 2014*                                                                                    Mattia Marelli